Diplomarbeit

The Density of Ultra-High Energy Protons within the Local Supercluster of Galaxies

- Die Dichteverteilung ultra-hochenergetischer Protonen im Lokalen Supercluster -

vorgelegt von Wiebke Schubotz

Institut für Experimentalphysik, Universität Hamburg

Januar 2011

Erklärung

Hiermit versichere ich, dass ich die vorliegende Arbeit selbstständig verfasst und nur die angegebenen Hilfsmittel und Quellen verwendet habe. Mit einer universitätsinternen Veröffentlichung bin ich einverstanden.

Hamburg, den 10. Januar 2011 Wiebke Schubotz

Erstgutachter: Prof. Dr. D. Horns
Zweitgutachter: Prof. Dr. G. Sigl

Abstract
This thesis is focused on the determination of the density of ultra-high energy protons within the Local Supercluster of galaxies. The calculations are based on a single-source model proposed by Berezinsky et al. [4]. The spatial density of such protons can be examined as a function of different physical effects and parameters, such as diffusion, the type of source, the propagation distance and others. The impact of diffusion and interactions with ambient photon fields that influence high-energy particle propagation are discussed in detail. Relevant interactions are the pion production on interstellar gas protons and photons, as well as electron-positron production. The results in [4] are reproduced and the work extended in terms of possible photon backgrounds. Beside the cosmic microwave background, photons from the extragalactic background light and the supercluster radiation field are taken into consideration. Moreover, the thesis examines the influence of different diffusion coefficients on the propagation and distribution of the protons and the influence of different magnetic field strengths.

Zusammenfassung
Der Schwerpunkt dieser Diplomarbeit liegt auf der Berechnung der Protondichte im lokalen Supercluster. Die Berechungen gehen zurück auf eine Veröffentlichung von Berezinsky et al. [4]. Dort wird ein Modell vorgestellt, mit dem sich die räumliche Dichteverteilung der ultra-hochenergetischen Protonen einer einzelnen Quelle berechnen lässt. Physikalische Effekte und Parameter, welche die Dichte beeinflussen, sind dabei z.B. Diffusion, die Propagationsstrecke eines Protons, sowie die Art der Quelle. Die Diffusion der Protonen und die Wechselwirkung der Protonen mit Hintergrundphotonen werden genau betrachtet, da sie die Dichteverteilung erheblich beeinflussen. Mögliche Wechselwirkungen mit den Photonfeldern sind dabei die Pionproduktion mit Protonen des interstellaren Gases oder Photonen und die Elektron-Paarerzeugung. Die Ergebnisse, die in [4] präsentiert sind, werden nachvollzogen und die Berechnungen hinsichtlich der Photonenfelder erweitert. Neben Photonen der kosmischen Hintergrundstrahlung werden auch Photonen des extragalaktischen Hintergrundlichtes, sowie das Strahlungsfeld des lokalen Superclusters betrachtet. Desweiteren werden die Einfüsse verschiedener Diffusionskoeffizienten und Magnetfelder auf die Propagation und Dichteverteilung der Protonen untersucht.

Contents

List of Figures

Chapter 1

Cosmic ray particles — An introduction

Cosmic ray particles, CR for short, have been a subject of study for more than one hundred years by now. Pioneer work was done by Victor Hess, an Austrian scientist who ventured a balloon flight in 1912, to find out more about ionizing radiation, which was a big puzzle to the scientific community at that time. The radiation that was measured on the surface of the Earth was thought to come from radioactive nuclei in the Earth's crust. Accordingly, Hess expected to measure less and less radiation as altitude would increase. The flight, which went up to 5000 m, became famous, but not because Hess verified the assumptions, but because his results indicated something totally different. Surprisingly, he discovered that the intensity of the flux *increased* with altitude. At that time the term "cosmic radiation" was first coined, because the radiation seemed to emanate from the universe, the cosmos. The discovery Hess made was so groundbreaking that he received a Noble prize for this experiment in 1936.
Nowadays, the term cosmic radiation is specified to "cosmic ray particles", because studies some time after the discovery indicated that the ionization comes indeed from individual charged or neutral particles. Starting in 1927, the detection of particles in cloud chamber experiments began. From this the idea arose that cosmic ray particles can collide with nuclei and gas molecules in the upper atmosphere and produce, via Einsteins $E = mc^2$, a huge amount of new particles that come down to the surface of the Earth as a particle "shower". Thus the name "secondary particles" came into being. It took some time, until those particles, e.g. muon, pions and positrons, could be verified and studied in collider experiments. This could only be done from the mid 50's on. A simplified image of a possible shower is depicted in figure 1.1. It shows a proton that serves as a starting point for a shower of secondary particles, including both leptons and baryons. In reality, the number of secondary particles that appear at the end of the shower is a lot larger, reaching up to several hundred.

Since the time of the cosmic ray discovery, a lot of effort was made to disclose their secrets. During the years, detection methods and experiments constantly improved and a better understanding and a more detailed view on the CR themselves, their

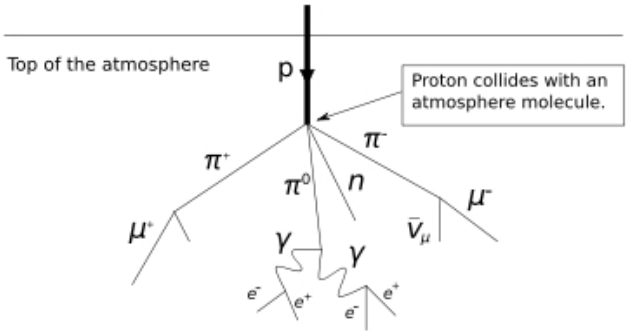

Figure 1.1: A simplified image of a particle shower. The image is taken from the web page *http* : *//en.wikipedia.org/wiki/Cosmic_ray*.

origin, propagation and interaction was gained. It started with Victor Hess, but as time passed many people joined the search for cosmic ray particles. Experiments grew in size and number of involved people. Today the experiments cover huge distances and are able to detect events that occur with an extremely small rate.
The information one has about CR today is presented in figure 1.2. It shows the overall spectrum, the amount of particles that is received here on Earth, according to the various energies the particles have. This figure contains the information of 20 experiments, which are all different in their experimental setup and research aims, but do agree in their measurements. At first sight one can see in this figure that the number of particles decreases with increasing kinetic energy E_{kin} of the particles. While CR with energies around 1 GeV have a flux of approximately one particle per second and square meter, particles with higher energies occur, and are thereupon detected, less often. Cosmic rays with energies around $E = 10^6$ GeV are only detected once per year and square meter. This behavior continues and ends in an extremely small flux of only one particle per hundred years and square kilometer for very energetic particles at the high energy end of the spectrum. These particles have energies of more than $E = 10^9$ GeV and are often named ultra-high energy cosmic rays (referred to as UHECR from here on).
The different fluxes result in an change of the slope of the spectrum. Whereas the low energy part is described by a function E^α with a spectral index of $\alpha = 2.7$, the spectrum becomes steeper at $E = 10^6$ GeV. This change is called the "knee" of the spectrum.
After that the spectral index is $\alpha \sim 3.0$. Another change in the spectrum occurs in the region of the "ankle", that are energies around $E = 10^9$ GeV. The spectral index changes back to $\alpha = 2.7$ there. The feature of the change of slope at the knee gave for a long time rise to many speculations, but nowadays some feasible explanations have been found. The most prominent explanation for the change of the spectrum is the crossover from the galactic component to the extragalactic component of the cosmic rays: It is believed that up to the energies of 10^6 GeV they originate from sources

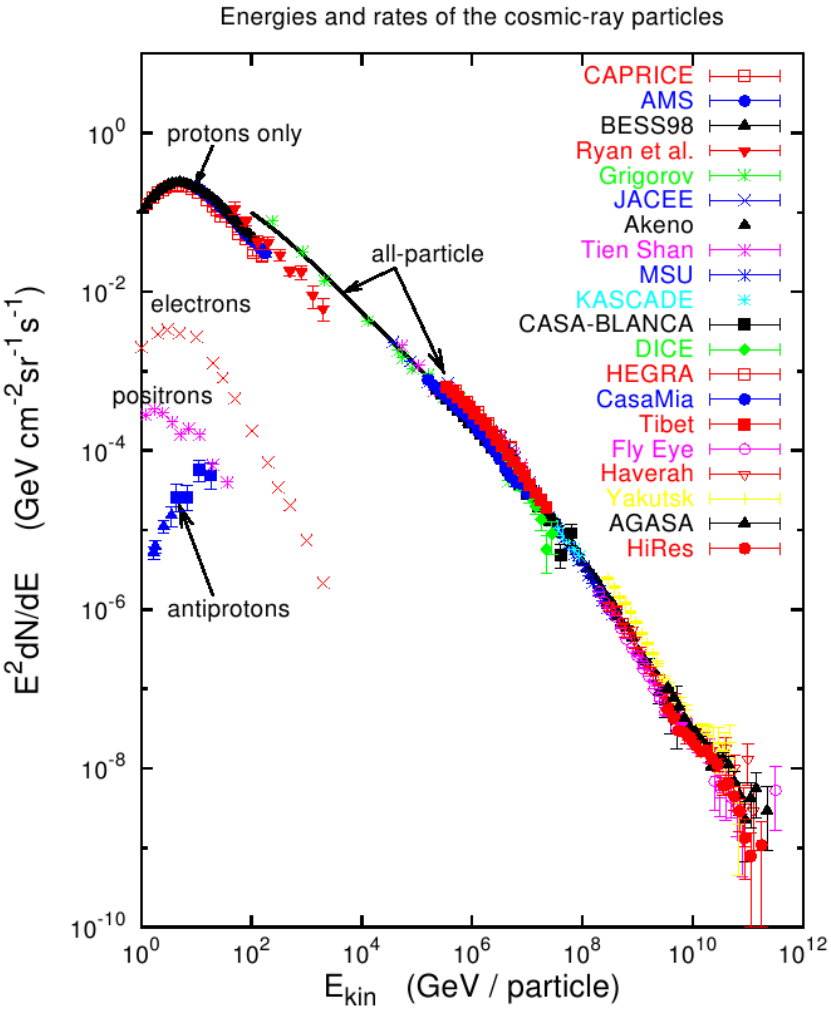

Figure 1.2: The cosmic ray spectrum today, as it can be found in the Hillas paper from 2006, in [17]. The image shows the all particle flux on Earth in dependence of the kinetic energy of the individual particles.

within our galaxy, see [16] for further discussion. Afterwards they are thought to come from sources outside of our galaxy. The reason is that galactic objects in general do not have the right combination of magnetic field and size to contain high energy particles inside the galactic environment. The gyroradius r_g is a distinct measure of charged particles. It is the radius of the orbit a particle travels when it is subject to magnetic fields. When a cosmic ray particle travels in space, both Lorentz force and centrifugal force act on it. If both forces are in equilibrium the expression

$$\frac{mv^2}{r_g} = ZevB \tag{1.1}$$

holds. Here v is the velocity of the particle, Z its atomic number, e its charge and B the magnetic field strength. Moreover, it is assumed that the magnetic field is perpendicular to the velocity. This equation can be solved for the gyroradius and yields for the case of a relativistic particle:

$$r_g[\mathrm{m}] = \frac{mv}{eZB} \simeq \quad 3.3 \times \frac{p[\mathrm{GeV}/c]}{ZB[T]}. \tag{1.2}$$

Of course, it is also possible to compute the maximal momentum a particle can have for a specific gyroradius from this expression. For a proton ($Z = 1$) inside our galaxy, the distance from which the particles start to leak from the galaxy is 5 pc. In astrophysics, parsec is a commonly used distance unit, one parsec equals 3.26 light years or 3.08×10^{16} meters. If now a weak galactic field of 10^{-10} Tesla is considered, equation 1.2 yields a maximal momentum of $\mathrm{p_{max}} = 4.6 \times 10^{15}\mathrm{eV/c}$. Up to this energy are CR particles confined inside the galaxy. Particles with higher momentum start to leak from the galaxy. On the other hand, this also means that particles that are detected with higher energies cannot originate from our galaxy, they must come from extragalactic sources "outside". They naturally appear less often, which shows up in the change of slope in the spectrum, it becomes steeper.
For the "toes" of the spectrum, CR with energies around $E = 10^{11}$ GeV, the information is very scarce, since the detection of those is very rare and their origin not entirely clear. Existing experiments give contradictory results on this issue. While e.g. data from the HiRes experiment shows a sharp decrease in flux of such UHECR, the results from AGASA show an increase of particle flux, see figure 1.2.
The detection of cosmic ray particles in general is not easy, because direct detection is only possible with balloon or satellite experiments. Most experiments however, are stationed at Earth and there the detection can only be done via the secondary particles. A calculation from this information "back" to the original CR that hit the atmosphere is therefore necessary.
The secondary particles are only a "footprint" of the original cosmic ray spectrum. Their flux on Earth is mostly isotropic, meaning that secondaries arrive from all possible directions with the same amount. So far there are only a few measurements, where an excess from a certain direction could be detected. This issue of anisotropy will be in detail discussed in section 2.2. In general, the measured spectrum here on

Earth will be different from the original cosmic ray production spectrum. It changes during the propagation of the cosmic rays to Earth.
For UHECR there is the problem of extremely low detection rates. For particles of more than 10^{20} eV one needs huge areas equipped with detector material to be able to detect these CR with a significant rate. The newest experiment for detection of the highest energy CR is the Auger experiment in Argentina.

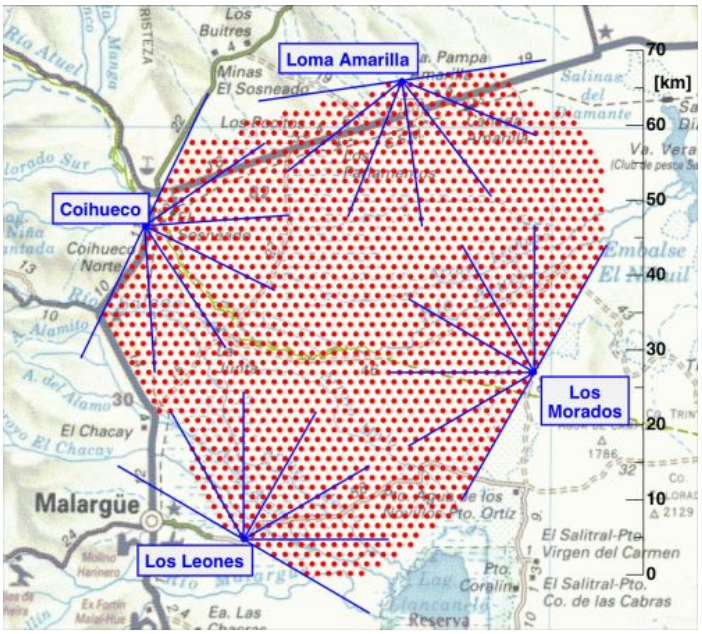

Figure 1.3: The Auger experiment in the Argentinean pampas. The red dots represent the water tanks, the blues lines the fluorescence telescopes. The figure is taken from the Auger collaboration web page *http://www.auger.de/public/sd.html*.

It is named after Pierre Auger, who initially proposed the idea of the showering of CR. This was in 1938, some time after secondary particles were detected in the first place. The Auger experiment covers a detection area of three thousand square kilometers and is equipped with 1600 water Cerenkov detectors and 24 fluorescence telescopes. The build-up started in 2004 and since 2008 data is being taken. In every water tank, seen as the red dots in figure 1.3, there is one photomultiplier that collects the Cerenkov light emitted from the particles that enter the tank. With this, the extension and exact position of the shower and its maximum can be measured. This is important, because the showers can extend up to square kilometer size. At the same time, the fluorescence telescopes, the blue lines in figure 1.3, act as calorimeters and measure the energy of the passing shower. They detect the faint fluorescence glow that occurs when the cosmic ray particles collide with gas molecules in the atmosphere. The more energy the individual particles have, the more fluorescence light is emitted as the shower proceeds to Earth. With the information from both arrays one hopes to receive detailed information about the primary cosmic rays with initial energies of

more than 10^{20} eV.
The contradiction of the AGASA and HiRES experiments is not the only reason why the region around the "toe" energies is of special interest to the astroparticle community. The composition of primary particles in this energy regime is to a great extent not well understood yet and one hopes that Auger will provide information on this issue.
HiRes results and also recent results from the Auger experiment back up the idea of the Greisen-Zatsepin-Kuzmin- (GZK-) cutoff, which describes the decrease in particle flux above the ankle. In 1966 two separate papers, [28] and [15], one written by Georgiy Zatsepin and Vadim Kuzmin, the other written by Kenneth Greisen, proposed a change in the CR spectrum due to the interaction of high-energy protons with the blackbody photon field of the cosmic microwave background (CMB). This interaction results in the production of neutral and charged pions, π^0 and π^+, see expression 1.4. Both papers were published shortly after the discovery of a large isotropic flux of microwave radiation with a temperature of roughly 3 K (this was later pinned down to 2.725 K). They studied the effect of this radiation in terms of cosmic ray propagation. Independently both papers found out that the spectrum above energies of $E = 10^{19}$ eV must be heavily influenced by the the production of π-mesons, so less high energy protons will arrive on Earth. According to the papers, this influence is caused by energy losses – the protons lose a big part of their initial energy (roughly 20%) in the collision with the blackbody radiation field and therefore "slide" to lower energies. This would lead to a sharp cutoff of the spectrum above $E = 10^{20}$ eV and to a steeper spectrum for energies slightly below this value. Since the CMB is uniform in the entire universe, it influences all high-energy protons and does not depend on the propagation direction of the protons or the special type of the source they are emitted from. The GZK-cutoff influences all cosmic ray protons with energies above several 10^{19} eV. As long as the threshold energy of the collision is sufficient to produce pions, the reaction takes place, so multiple proton interactions are also possible. Especially protons with energies above the "toe" can undergo several pion-production processes and it takes some time for them to drop below the threshold energy.
As mentioned already, one can deduce information only from measurements of secondary particles. But their properties give only information about how the primary CR arrived at the Earth's atmosphere. How its characteristics changed along its way from the source to the Earth is an entirely different question. One aim of this thesis is to take a look at the mechanisms that influence a high-energy proton. Energetic changes arise by various processes, e.g photopion production or photopair production due to interactions with photons, as well as collisions between protons and interstellar gas. These protons are also subject to diffusion if magnetic fields are present in the surrounding medium. This process deflects particles from their original propagation direction. This means that astronomical objects can seldom be seen in "first cosmic ray light", one cannot be sure that particles detected from a certain direction were actually also emitted in that region. It is therefore often difficult to identify an astrophysical counterpart to the detected secondary particles. The only regime where

diffusion does not act strongly on particles, where a connection between their source and detection is still possible, is the range of the UHECR above $E = 10^{18}$ eV. These cosmic rays are so energetic that they are only minor affected by the magnetic fields, so they could possibly serve as a "high energy telescope" for CR sources. Of course, this only happens when the magnetic fields are small enough. It is difficult to term the strength of those magnetic fields, literature holds several orders of magnitude, ranging from pico- to hundreds of microgauss, in store. The kind of cosmic rays that is most suitable for serving as such "high energy telescope" are protons. They have a positive charge of one and are, off all charged CR, the ones that are deflected least in a certain magnetic field, so protons are an ideal subject to study the behaviour of UHECR in galactic and extragalactic surroundings.

1.1 Where do they come from?

The origin of UHE protons is for the most part still unclear, most ideas are still very vague. The first uncertainty arises with the term cosmic ray production. Usually not the production mechanism is questioned, but the *acceleration* mechanism. The classical acceleration models support the idea that CR are accelerated by moving clouds of magnetized plasma or in shock waves from supernova explosions. This idea goes back to Enrico Fermi, who described the possible acceleration of CR in supernovae for the first time in 1949 and coined the expression "Fermi acceleration". But a thorough understanding of the acceleration is not gained yet.
The protons themselves arose in one of the earliest epochs in the history of our universe. They were created in the era of hadronization, about one micro-second after the Big Bang. Before that, the energy density of the evolving universe was so high that quarks and antiquarks existed as quasi-free particles in the quark-gluon plasma. After that the quarks formed stable nuclei, protons and neutrons, which were in thermal equilibrium with all the other Standard Model particles, such as electrons, positrons and neutrinos, see [27]. At this time the universe had a temperature of $\sim 10^{11}$ K. This provided enough energy that protons could constantly convert into neutrons ($p + \bar{\nu_e} \rightarrow e^+ + n$) and neutrons into protons ($n + \nu_e \rightarrow e^- + p$). The energy density of this radiation-matter-soup was too high to form any stable nuclei. That happened later, when the universe cooled down. As the universe was 0.11 seconds old, the temperature had sunk to 3×10^{10} K and the back and forth change between neutrons and protons slowly declined. Because of the lower energy density, it became harder for the protons to change into the heavier neutrons, an inequality started to evolve. This continued until 14 seconds after the Big Bang the first nuclei started to form, the primordial nucleosynthesis began. The temperature then was below 10^9 K and the first stable helium (^{4}He) atoms and also small fractions of deuterium, helium three (^{3}He), lithium and beryllium started to form. The helium to proton ratio was 25%:75%. Today protons are "stuck" inside astronomical objects, but they can escape and propagate through space if they are ejected by supernova explosions or high energy jets of active galaxy nuclei (AGN).

As mentioned before, UHECR can only be generated in an object that has the right combination of magnetic field and size. Figure 1.4, taken from [2], shows possible sources. The solid black line indicates protons of energies of $E = 10^{20}$ eV. Every astronomical object that coincides with this line can accelerate protons to ultra-high energies. From the figure one can tell that basically only AGN or galaxy clusters come into question.

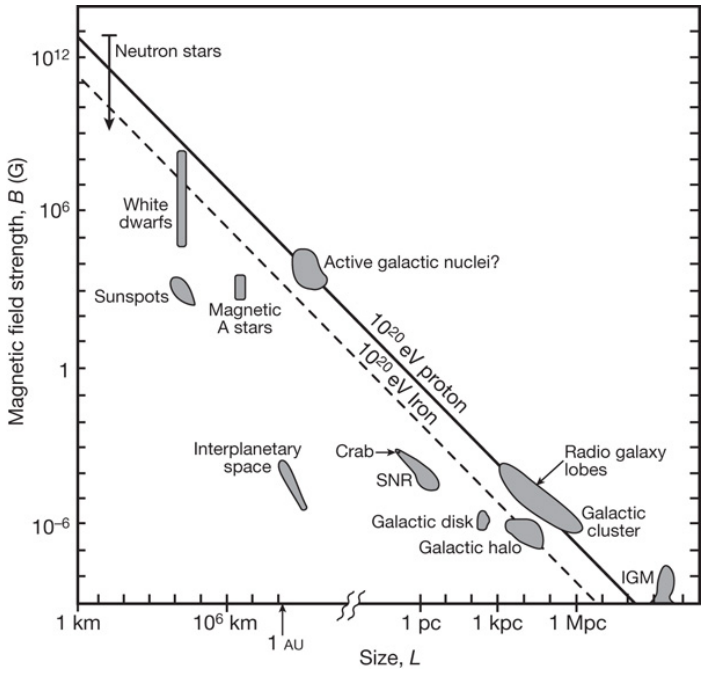

Figure 1.4: Possible sources of UHE protons. The objects that cross the solid black line can accelerate protons up to $E = 10^{20}$ eV. The figure is taken from [2].

One of the most popular ideas where the UHECR come from is indeed the idea of the Local Supercluster (LSC) of galaxies.

1.1.1 The Local Supercluster and its Proton content

Recent observations from the Auger observatory show a correlation between UHECR and the direction of the supergalactic plane. Also other publications, such as [16] give hints that a large galaxy cluster in the centre of the supergalactic plane could be a source of high energy protons. In [21], Matthiae points out that CR with an energy above $E = 5 \times 10^{19}$ eV propagate with a probability of 90% within a distance shorter than 250 Mpc. For protons of energies higher than $E = 10^{20}$ eV this region scales down to a distance of 75 Mpc.
The LSC is the large extragalactic structure in which our Milky Way resides. It is an accumulation of galaxy clusters that form a roughly cylindrical shape of diameter of ~ 40 Mpc and a height of about 10 Mpc. In figure 1.5 one can see the LSC and its

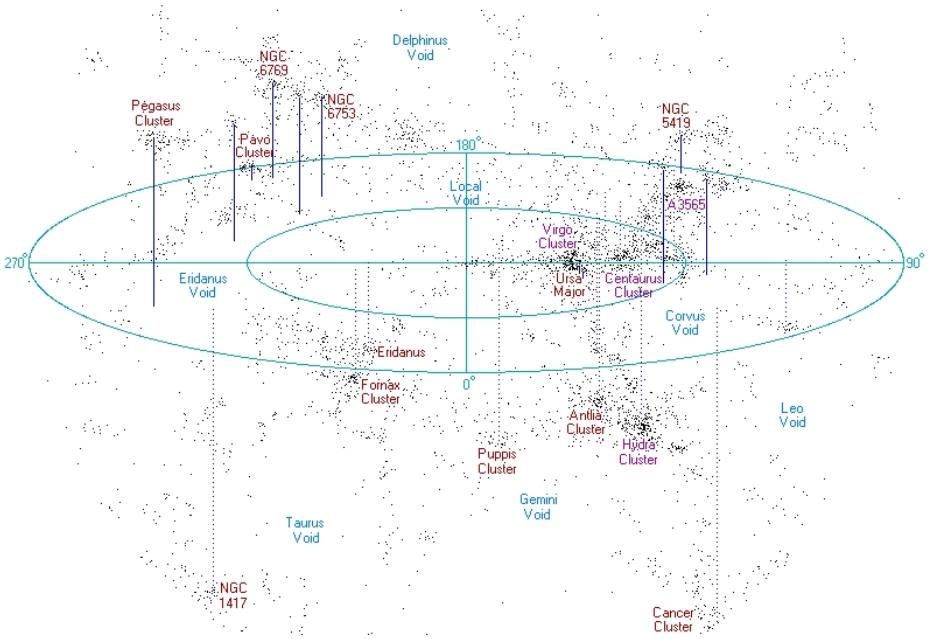

Figure 1.5: The local supercluster (Virgo supercluster) embedded in the larger galactic structure. The central region of the LSC is the Virgo cluster. The Earth is positioned at the edge of the supercluster at the origin of the coordinate system. The figure is taken from the web page *http://www.atlasoftheuniverse.com/200mill.html*.

surroundings. The central region includes the large Virgo cluster of galaxies, the very intense radio source M 87 (Virgo A) and the galaxy M82. The Virgo cluster dominates the structure, this leads to the often used name "Virgo Supercluster", for the entire structure of the supercluster. However, this is not to be mistaken with the "Virgo cluster" which describes only the galaxy cluster in the very centre. The coordinate system in figure 1.5 is not centered at the Virgo cluster, but at the position of the Earth. The Earth is located within the Local Group, a galaxy cluster at the outer edge of the supercluster, so cosmic ray particles that are detected on Earth have to cross almost the entire radius of the supercluster. The distance from the centre of the Virgo cluster to Earth is 17 Mpc.
As one can see in figure 1.5, the supercluster is dense in its central region and thinnes out as the outer rim is approached. This goes well with the assumption that most of the supercluster mass is located in its centre. Some publications, for example [26], claim that even up to 80% of the entire mass is to be found in the central region of the supercluster. It is believed that some of the highest-energy cosmic rays ever detected come from its central galaxy, M87. Since this is the most dense part of the cluster, one assumes that most cosmic ray protons emanate from there. The assumption that the Virgo Cluster of galaxies is the main source of the cosmic ray protons that reach the Earth seems viable and is the "working hypothesis" for this diploma study.

1.1.2 Protons in the LSC

Although the Milky way is located in a less dense area of the LSC, the Earth is bombarded with high energy cosmic rays all the time. The interest of this study lies in the distribution of those within the supercluster, because they are an ideal object to give information on the extragalactic "neighbourhood" of our galaxy. In studying their propagation and comparing it with results from experiments, one can learn much about cosmic ray propagation and the influence of magnetic fields on it.
Predictions for the spectrum on Earth depend greatly on the assumed initial particles and their properties. The determination of the spatial energy density n [$\mathrm{m}^3\,\mathrm{eV}^{-1}$] of the high-energy proton component within the LSC is the aim of this thesis. A detailed knowledge of the proton allocation is desirable and important for simulations and further predictions of secondary particle spectra.
Usually the propagation of UHECR is computed with computer programmes that simulate different influences on the spectrum. Most of these codes work with a constant proton density throughout the region of interest. It is not properly examined if this is plausible for all cases. For example, for the case of the supercluster it is known that the proton density decreases as the distance to the centre becomes larger. For a prediction of proton interactions it is necessary to have a detailed knowledge on their density distribution. This thesis will take the approach of a Gaussian distribution of protons. It is the result of a mathematical model by Berezinsky et al. and will be presented section 2.1. A Gaussian distribution with a declining density seems favourable, since the inner parts of the LSC are more dense than the outer parts.

1.2 And where do they go? – Diffusion and Energy loss

This paragraph is supposed to summarize what is already known about the propagation of cosmic ray protons. They are accelerated in many different ways, which results in a broad energy range. After injection into the supercluster they interact with the ambient medium. They are deflected by magnetic fields that are present throughout the entire LSC and give rise to diffusion and also interact with interstellar gas and ambient photon fields, mostly with photons from the cosmic microwave background.
Within the LSC there is a homogeneous magnetic background field which greatly affects cosmic rays. The origin of this field is not entirely clear, but it can be separated in two major contributions, a large scale component, caused by relic processes of the evolution of the universe, and a local component due to the structures of the supercluster, e.g. individual galaxies. The large scale component is thought to originate from a phase transition, see [24] for further discussion on this. The local component is thought to have several sources, the most prominent being supernova explosions. Since the plasma of a supernova contains ionized particles, it exhibits a magnetic field which is then also dragged into space and spreads over the galaxies. Numerical values

on the magnetic fields in the supercluster vary, but fields larger than 10^{-12} G, see [24], that arise from the adiabatic compression of the primordial magnetic fields can be assumed. According to [24], numbers up to $B = 10^{-6}$ G are feasible in cores of galaxies. Possible constraints of magnetic fields will be discussed in section 2.3.2.
For a proton of energy $E = 10^{18}$ eV and a rather strong magnetic field of $B = 1\mu$G (keep in mind that 1G = 10^{-4} Tesla) equation 1.2 yields $r_g \sim 1.07 \times 10^{-3}$ Mpc. In the case of the LSC it is assumed that the the gyroradius equals the size of the supercluster. To establish a gyroradius of $r_g = R = 20$ Mpc, the cosmic ray energy must be larger. Using equation 1.2, an energy of $E = 10^{20}$ eV has to be provided to achieve this. The interplay with magnetic fields causes low energy protons to be confined within the vicinity of the cluster. For $E < 10^{20}$ eV they differ from a straight line propagation and are deflected several times in the cluster during their propagation. However, how much they are deflected depends on the proton energy and the B-field that is present. Besides the diffusion process they experience also inelastic collisions with other particles. These processes lead to the loss of energy and are very important for the calculations of the spatial proton density. The graphs for the interactions that are considered in this thesis are presented in figures 1.6 –1.10:

1) Pion Production via collisions with interstellar gas:

$$p + p \rightarrow \pi^0 + p + p \quad \text{or} \quad p + p \rightarrow \pi^+ + p + n \tag{1.3}$$

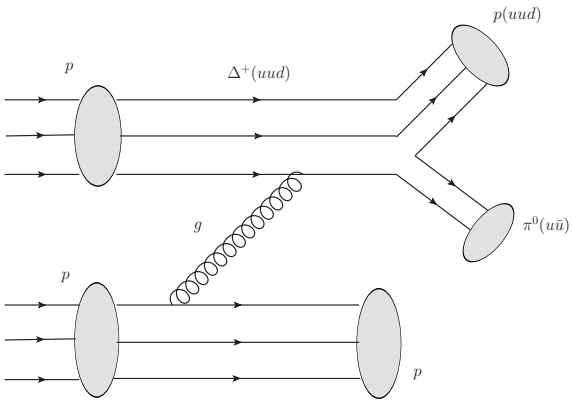

Figure 1.6: The proton-proton collision with the interstellar gas content of the universe. All interaction graphs were done with the JaxoDraw package as it is presented in [6]. This figure shows as possibly resulting particles two protons and a neutral pion.

2) Photopion Production:

$$p + \gamma \rightarrow p + \pi^o \quad \text{or} \quad p + \gamma \rightarrow n + \pi^+ \tag{1.4}$$

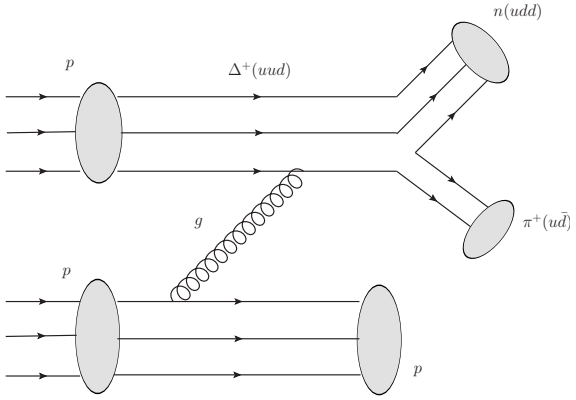

Figure 1.7: The collision between UHE protons and protons from the interstellar gas (ISG) can lead also to the production of proton, neutron and charged pion.

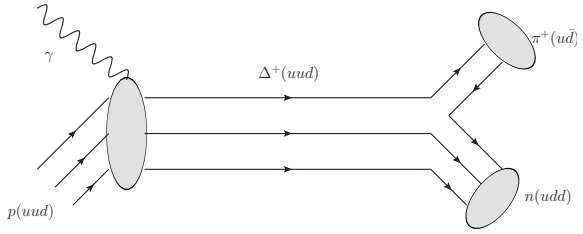

Figure 1.8: The production of a charged pion and neutron as a result of the inelastic collision between UHE proton and a photon from the ambient radiation field.

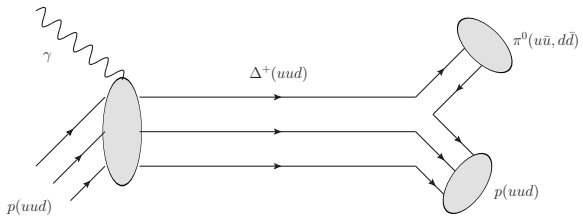

Figure 1.9: The production of a neutral pion and a proton in the process of pion-photoproduction. The photons come from the ambient radiation field.

3) Electron-Pair Production (also named Bethe-Heitler process):

$$p + \gamma \rightarrow p + e^- + e^+ \tag{1.5}$$

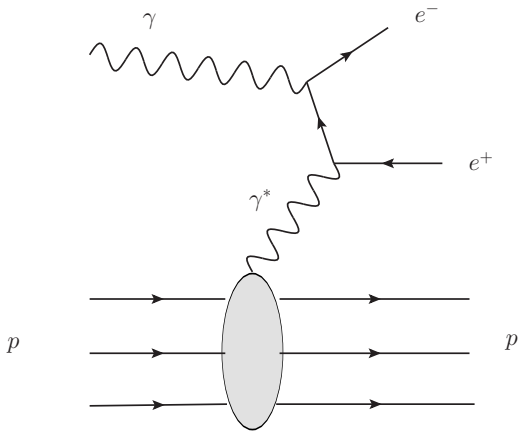

Figure 1.10: The production of an electron-positron pair as a photon and cosmic ray proton collide.

The latter two processes are caused by interactions with ambient photon fields. To be exact, one should mention that not only π-mesons, but also ρ-, η-, K- and ω-mesons can be produced in an interaction between photons and cosmic ray protons. But the single-pion process is by far the most important mechanism, so the investigation of $p\gamma$-interactions is limited to this case. As mentioned in the discussion on the GZK-cutoff, pion production sets in at energies above $E \sim 6 \times 10^{19}$ eV, because only these protons provide enough energy to overcome the threshold energy for this process. Below this proton energy, a similar process takes place, pair production. This is also a collision between the initial cosmic ray proton and a photon from the ambient photon field, but instead of a π-meson, a less energetic electron-positron pair is produced.
The derivation of the equations that describe those energy losses are presented and discussed in the section 2.4.

1.2.1 Nuclei

Abundant heavier nuclei in the UHECR regime are those of lithium, beryllium and boron ($Z = 3, 4, 5$). Even elements up to iron ($Z = 56$) exist, but those heavy elements hardly occur, since they photodisintegrate at ultra-high energies when they collide with background photons:

$$A + \gamma \rightarrow (A - 1) + N, \quad N = n, p \tag{1.6}$$

In such a process single protons and neutrons are released. In his paper [15], Greisen points out that the photodisintegration against photons of the CMB happens at en-

ergies of $E = 5 \times 10^{18}$ eV already. According to this, heavy nuclei should not be a large fraction of the UHECR.

1.3 Aims and structure of this thesis

In this chapter, an introduction on the general subject of cosmic ray particles was given, including a short outlook on the subject of their propagation.
Chapter 2 presents the theoretical basis of the calculations in this study. The physical parameters of diffusion and energy loss of the ultra-high energy protons, which govern particle propagation, are presented and discussed in detail there. Special attention is given to the diffusion coefficient $D(E)$, of which two possible expressions are presented. Additionally, it is examined how the choice of a certain $D(E)$ influences the propagation of the protons within the supercluster. A calculation in section 2.3 will show that these protons are actually confined inside this region, therefore it is advantageous to study their density distribution within the supercluster of galaxies. Since diffusion is closely connected to the energy losses UHE protons experience, a large part of chapter 2 is dedicated to the investigation of the different energy loss processes. The three possible interactions, pion production on interstellar gas protons and background photons, as well as electron-pair production on background photons, are carefully examined. The parameters that influence these processes, the cross section and the inelasticity, are studied in detail, too.
Chapter 3 describes the actual implementation of the processes presented in chapter 2 and describes some numerical assumptions.
The aim of this thesis is to investigate the spatial density distribution of UHE protons. The resulting influence of the different processes and parameters, introduced in chapter 2, is presented in chapter 4. There the results of the proton density calculations are shown. The influences of the individual photon fields are discussed and also other parameters, such as proton energy, propagation time and magnetic field strengths are studied. Finally, the results are matched to observational data from the Auger observatory. This is presented in section 4.7. Chapter 5 summarizes this work and gives an outlook on how the results of this study could be used in the future. In the the appendix, detailed calculations of formulae that are of importance throughout the entire study are given.

Chapter 2

Theoretical preparations

The aim of this chapter is to derive and explain certain formulae that are used throughout the course of this thesis and to look in detail at some of the physical processes that are of interest for determining the spatial density of CR protons. The issues of anisotropy, particle diffusion and energy loss processes are discussed.

2.1 The spatial distribution of Protons

Concrete knowledge on the propagation of cosmic rays is important for detailed predictions of the measured spectra here on Earth. The more particles arrive, the higher the number of secondary particles that can be detected. But since propagation of cosmic ray particles is influenced by many factors, it is difficult (but not impossible) to give reliable predictions. A factor of great uncertainty is e.g. the exact spatial number density of cosmic ray particles. It is thought that they appear abundantly in regions near galactic and extragalactic sources, but for the region between these sources this not clear. The aim of this thesis is to determine the spatial density $n(E, r, t)[\mathrm{m}^{-3}\mathrm{eV}^{-1}]$ of UHE protons. The calculations performed in this study are based on the work of Berezinsky et al. in [4] and [5], therefore references are given to both publications. They describe the same work, but give details on different aspects, so for a thorough understanding both publications should be consulted. Berezinsky et al. investigated the UHECR propagation and focused on a single source model with stationary diffusion. In their paper [5], they present an equation to determine the CR density $n(E, r, t)$ as a function of the proton energy, distance to the source and its propagation time. Berezinsky et al. take into account the interactions of the protons with photons from the CMB, leading to pion- and pair production. The calculations of this thesis extend their work in terms of possible interactions and ambient photon fields. The high energy protons are not only able to interact with the CMB radiation, but also with photons from the extragalatic background light (EBL) and the local supercluster radiation field (SCRF). Moreover, inelastic collisions between UHE protons and interstellar gas protons are taken into account. The expression Berezinsky et al. derived for the proton density is found by solving the differential equation for

the spatial proton density n:

$$\frac{\partial n}{\partial t} - \underbrace{D(E)\nabla^2 n}_{\text{diffusion}} + \underbrace{\frac{\partial}{\partial E}(bn)}_{\text{energy loss}} = \underbrace{Q(E_g)\delta(\vec{r}_g)\theta(t_g)\theta(T-t_g)}_{\text{injection of new particles}}, \tag{2.1}$$

This equation describes the development of the proton density n when cosmic ray protons propagate to Earth from an extragalactic source and are influenced by certain processes. On the right side of equation 2.1, there is a steady production rate of new particles, mediated by a point source that is positioned at $\vec{r}_g$ and is "switched on" at time t_g. It emits particles with energy E_g. In case of the LSC it is assumed that protons can be accelerated up to energies greater than $E_g = 10^{20}$ eV. Besides, a pulsed generation of protons is assumed, the pulse period is given by the time T. The differential source spectrum has a power-law dependence that is taken to be

$$Q(E_g) = K(E_g + E_m)^{-(\gamma+1)}, \tag{2.2}$$

where E_g is the kinetic energy of the protons at the time of generation t_g and E_m is a normalization energy of $E_m = 1$ GeV, see [5]. Classical acceleration models are based on Fermi acceleration and predict naturally a power-law spectrum for the production at the sources, see [21], so this assumption is well established. The constant K describes the maximal output of the source, $K = \int_{E_m}^{\infty} Q(E_g)E_g dE_g$. It is connected with the cosmic ray luminosity L_p via:

$$K = \gamma(\gamma-1)L_p E_m^{\gamma-1}. \tag{2.3}$$

The cosmic ray luminosity L_p is a measure of how much energy is radiated off by the ejection of cosmic ray particles per unit time. The cosmic ray luminosity is measured in erg/sec, where 1erg $= 10^{-7}$Joule $= 1.6 \times 10^{-12}$ eV.
The proton density in a certain volume changes as time elapsed. This change is taken care of by the diffusive term in the differential equation, containing the diffusion coefficient $D(E)$. Furthermore there are energy loss processes which occur, those are described by $b(E) = -\frac{dE}{dt}$ in equation 2.1. The processes conserve the total number of protons inside the cluster, but influence the proton energy and propagation. Equation 2.1 comes from earlier work by Ginzburg and Syrovatskii, see [12], where this equation was also solved. This was done by using a Greens function. A detailed discussion on the solution of the differential equation is therefore left to this book.

In [4], Berezinsky et al. used this solution and fixed the time of the "switch on" of the source to $t_g = 0$. The expression yields then

$$n(E,r,t) = \frac{(\gamma_g - 1)(\gamma_g - 2)L_p}{b(E)E_0} \times \int_{\lambda(E,t-T)E}^{\lambda(E,t)E} \frac{dE_g}{E_0} \left(\frac{E_g}{E_0}\right)^{-\gamma_g} \frac{1}{(4\pi\lambda_0(E,E_g))^{\frac{3}{2}}} \exp\left(\frac{-r^2}{4\lambda_0(E,E_g)}\right), \tag{2.4}$$

with $\gamma_g = \gamma + 1$ and $E_0 = E_m = 1$ GeV from equation 2.3. This expression gives detailed information on the distribution of the protons within the vicinity of a certain source. The spatial proton density depends on the proton energy E, the distance to the source r, the time t between the start of the source and now, the source pulse duration T, the spectral source index γ_g, the luminosity of the source L_p and the energy losses described by $b(E)$. The function $\lambda(E,t)$ relates the energy the protons have at their generation in the source, E_g, with the observed energy E at detection via $E_g = \lambda(E,t)E$. This will be discusses thoroughly in chapter 3.

The parameter λ_0 is determined by

$$\lambda_0(E,E_g) = \int_E^{E_g} \frac{D(E')}{b(E')} dE', \tag{2.5}$$

containing the diffusion coefficient $D(E)$ and energy loss terms. There is a constant interplay between energy loss and diffusion, because particles with a lower energy have a small diffusion coefficient $D(E)$ and diffuse more. This leads to more interactions, more energy loss and in return to a lower $D(E)$ and so on. On the other hand, when $D(E)$ is large, protons travel fast and do not interact much with other particles. This interplay is described by $\sqrt{\lambda_0}$, which yields the diffusive propagation distance for a certain time t. It describes how far a proton can travel when it is subject to certain energy loss processes, specified by $b(E)$, and diffusion.
Equation 2.4 yields a Gaussian distribution of the protons, which is a result of the analytic solution to equation 2.1. However, it matches well the assumption that the inner parts of the supercluster are more dense than the outer parts, so 2.4 yields a good description of the actual situation.
For fixed values of E, r and t, it is now possible to predict the proton distribution at various points within the LSC. The calculations of this study follow to a great extent the calculations in [5] that consider the case of the NGC 4151 Seyfert galaxy as a possible comic proton source. After the results of both studies are compared, the proton density can be examined for different parameter sets also. This will be presented in detail in chapter 4. The exact prediction of $n(E,r,t)$ can lead to a more precise knowledge on the interaction processes the UHE protons undergo at certain positions in the supercluster. This knowledge can also be used to improve propagation codes. The implementation of the variation of n would improve predictions towards

the production of secondary particles and their possible detection rates.

On Earth it is only possible to measure the intensity I of the particles, not the actual particle density n. The particle intensity is the amount of particles that reaches the ground per square meter, per second and sterad. For an isotropic emission of cosmic rays the intensity is connected with the particle density via

$$N\left[\mathrm{m}^{-3}\right] = \frac{4\pi I}{v}. \tag{2.6}$$

In the case of UHECR protons v equals the speed of light c. In this study the total number density N $[\mathrm{m}^{-3}]$ is substituted with the spatial energy density n $\left[\mathrm{m}^{-3}\,\mathrm{eV}^{-1}\right]$. So I is measured in terms of $\left[\mathrm{m}^{-2}\mathrm{sr}^{-1}\,\mathrm{s}^{-1}\,\mathrm{eV}^{-1}\right]$ and yields the proton spectrum.

2.2 Anisotropy

The spatial proton distribution is affected by many factors. Depending on how effective the diffusion process is, the protons are spread out more or less throughout the supercluster. For UHECR is it possible that they resist diffusion and show a correlation between their source and the direction the particles are detected from. This results in a large anisotropy. Therefore the anisotropy of ultra-high energy protons is also examined in this thesis.
Usual definitions on intensity and flux assume that the particles arrive isotropically from all directions. If this is not the case, due to magnetic fields or other disturbing factors, one needs a measure to characterize the anisotropy. This is done with the degree of anisotropy $|\vec{\delta}|$

$$|\vec{\delta}| = \frac{I_{\max} - I_{\min}}{I_{\max} + I_{\min}}. \tag{2.7}$$

This formula yields the percentage of anisotropy and contains the maximum and minimum of the particle intensity as a function of direction, $I = I(\theta)$. It is assumed that the maximal intensity comes from the direction where $\theta = 0$.
However, the formula that used in this study to calculate the degree of anisotropy differs from equation 2.7 and is presented in equation 2.8. Its full derivation, starting from 2.7, is somewhat tedious and left to [4], p. 29 ff. The calculations presented there lead to the expression of

$$\delta(E,r,t) = \frac{3D(E)}{c\,n(E,r,t)} \left|\frac{\partial n(E,r,t)}{\partial r}\right| \tag{2.8}$$

with

$$\left|\frac{\partial n(E,r,t)}{\partial r}\right| = \frac{2\pi K r}{b(E)} \int_{\lambda(E,t-T)E}^{\lambda(E,t)E} dE_g E_g^{-(\gamma+1)} \frac{e^{\left(\frac{-r^2}{4\lambda(E,E_g)}\right)}}{(4\pi\lambda(E,E_g))^{\frac{5}{2}}} \tag{2.9}$$

being simply the derivative of $n(E,r,t)$ with respect to r.

2.3 Spatial Diffusion

Although diffusion occurs in many transport situations and is a rather familiar subject, the question is why does it so effectively influence particle propagation in the supercluster? What are the parameters that play a role and how do they influence CR propagation in detail?
Diffusion itself describes the propagation of particles through a medium until a homogeneous distribution is achieved. This description is suitable for a variety of physical processes: from biological diffusion, e.g. the motion of nutrients in cells, up to the propagation of UHECR in an extragalactic environment – all of those transport processes exhibit diffusion. It is always a transport of particles from regions of high particle concentration to low particle concentration. Diffusion happens until the density gradient is zero (or very small). The exact derivation of the current density of particles leads to Fick's first law:

$$j_x = -\frac{\Lambda\bar{v}}{3}\frac{\partial n}{\partial x} = -D \times \nabla_x n. \tag{2.10}$$

The current density j_x is equal to the product of the concentration gradient ∇_xn and the diffusion coefficient $D = \frac{\Lambda\bar{v}}{3}$, which has a large influence on the diffusion. The current density in equation 2.10 depends not only on the mean free path Λ of the particle, but also on its mean velocity $\bar{v}$. For relativistic particles, protons in this case, the mean velocity is the speed of light and Λ can be as big as an entire galaxy. In this study Λ equals the gyroradius r_g, which is the condition for Bohm diffusion. Bohm diffusion is a very slow diffusion process and therefore contains particles well in a certain volume. The diffusion coefficient is then

$$D(E)_{\text{Bohm}} = \frac{1}{3}\, r_g(E)\, c. \tag{2.11}$$

When the protons are subject to diffusion, they can be completely deflected from their original path lose all their "memory" of where they came from. This de-correlation process is energy dependent: Particles propagate either in a rectilinear or diffusive regime, depending on their energy. Particles with high kinetic energies are in the rectilinear regime, where they hardly diffuse, but travel almost in straight lines. For low kinetic energies they propagate in a diffusive regime. As particles lose energy they can change from one to the other. The distance r a particle can propagate in the diffusive regime is

$$\begin{aligned} &r^2 = D \times t, \text{ in contrast to the rectilinear regime where} \\ &r = v \times t. \end{aligned} \tag{2.12}$$

From equation 2.10 one can find that diffusion is ruled by the diffusion coefficient, it is a measure of how strong this mechanism is.

2.3.1 The diffusion coefficient

The diffusion coefficient $D(E)$ is the parameter that governs diffusion and determines how fast particles diffuse. It is the proportionality factor that describes the strength of the current density j_x. If $D(E)$ is large, the current is high and the particles diffuse fast from one point to another. In contrast, when $D(E)$ is small, it takes a longer time until two different concentrations are equalized. The diffusion coefficient can be described as the "mobility" of the particles, the larger it gets, the faster does diffusion take place. The actual value of $D(E)$ is influenced by magnetic fields in the surrounding medium and by the energy the individual particles have. In this study two different coefficients are used, one is taken from [4] and yields

$$D(E)_{\text{Berezinsky}} = D_0 \times \left(\frac{E}{10^{19}\text{eV}}\right)^{\frac{1}{2}}. \tag{2.13}$$

In their paper, Berezinsky et al. calculate the spatial proton density with this diffusion coefficient. They discuss certain values and propose a general expression of $D(E) = D_0 \times (\frac{E}{10^{19}\text{eV}})^{\beta}$, where β ranges between 0.5 and 0.8 and D_0 between $(1-5) \times 10^{34} \frac{cm^2}{s}$. For the case of the Seyfert galaxy NGC 4151, with which the calculations in [5] are performed, the diffusion coefficient is set to $D_0 = 3 \times 10^{34}\,\text{cm}^2\text{s}^{-1}$. They assume a quasi-regular magnetic field of strength $B \sim 2 \times 10^{-8}$ G.

The other diffusion coefficient is a fit that is taken from a paper by Globus, Allard and Parizot, [13]:

$$D(E) = D_{\text{Bohm}}(E_0)\left(\frac{E}{E_0}\right)^{\frac{1}{3}} + D_{\text{Bohm}}(E_1)\left(\frac{E}{E_1}\right)^{2}, \tag{2.14}$$

where $D_{\text{Bohm}}(E)$ is given by equation 2.11. This diffusion coefficient describes diffusion in a turbulent magnetic field, see section 2.3.2. The values of E_0 and E_1 are chosen such that $2\pi r(E_0)_g = \lambda_c$ and $2\pi r(E_1)_g = \frac{3}{2}\lambda_c$. E_0 is the energy where the transition between the diffusive and the quasi-linear regime takes place. The magnetic field dependence is present in the expression for the gyroradius, equation 2.15. Here, r_g is given as a function of particle energy E, the charge Z ($Z = 1$ for protons) and the magnetic field strength B:

$$r_g[\text{Mpc}] = 1.1\text{Mpc} \times \frac{E[\text{EeV}]}{ZB[\text{nG}]} \tag{2.15}$$

The equation yields the gyroradius in megaparsec, if the magnetic field is provided in nanogauss and the particle energy in EeV (1 EeV=10^{18} eV). Diffusion coefficients are studied by many authors, the ones just presented are only two possible ways to approach this issue. Both were used to analyze the influence of diffusion on the spatial proton density. The full derivation of $D(E)_{\text{Globus}}$ can be found in [13], but some general aspects of this work are presented here as well.
In their study they simulate the trajectories of 100.000 particles with energies from

$E = 10^{16}$ eV up to $E = 10^{20}$eV. Energy losses are omitted. They assume a turbulent field of $B = 10$ nG and a maximal turbulent scale of $\lambda_{max} = 1$ Mpc. Detailed information on the characteristics of magnetic fields is given in section 2.3.2. Based on the simulated trajectories they calculate the average linear distance that is traveled by the cosmic rays

$$\Delta r^2 = 6D\Delta t \tag{2.16}$$

and derive from there what they call the *instantaneous effective diffusion coefficient* D. They examine this with respect to the gyroradius and find a fit to the energy dependence of $D(E)$, equation 2.14.
Figure 2.1 shows the course of $D(E)_{\text{Globus}}$ and $D(E)_{\text{Berezinsky}}$ as a function of energy E.

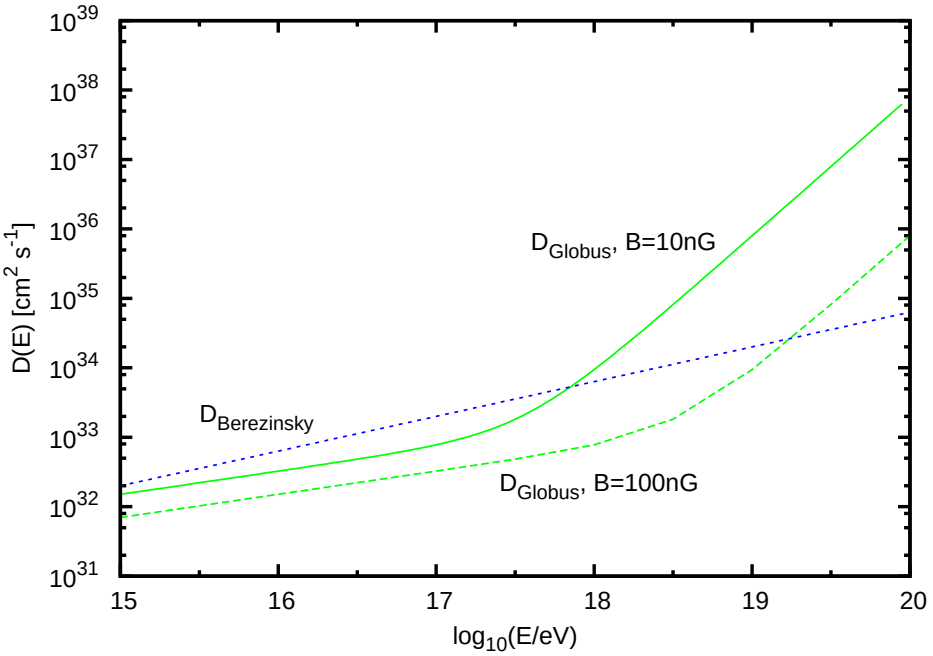

Figure 2.1: The different diffusion coefficients $D(E)$ that are used in this study as a function of the particle energy E. In blue $D(E)_{\text{Berezinsky}}$ from [5] is depicted and in green $D(E)_{\text{Globus}}$ from [13].

In 2.1 it can be seen that both coefficients start in the same range, but differ strongly when energies around $E = 10^{17}$ eV are reached. This is where the propagation changes smoothly from the diffusive $D(E) \propto E^{\frac{1}{3}}$ to the rectilinear $D(E) \propto E^2$ regime for Globus' diffusion coefficient. As expected from equation 2.15, $D(E)_{\text{Globus}}$ decreases with increasing B-field. Berezinskys coefficient shows the $E^{\frac{1}{2}}$-dependency for all particle energies.
Turbulent magnetic fields can lead to long diffusion times of the cosmic ray protons, since they are deflected several times before arrival. Diffusion can even confine protons inside a certain volume, if $D(E)$ is large enough.

The time an UHE proton needs to propagate a certain distance can be approximated with equation 2.12. If this is solved for t,

$$t_{\text{diff}} = \frac{R^2}{2\,D(E)}, \tag{2.17}$$

the diffusion time inside an object with a certain radius R can determined. The factor of two is a conventional choice. Figure 2.2 displays the results of equation 2.17.

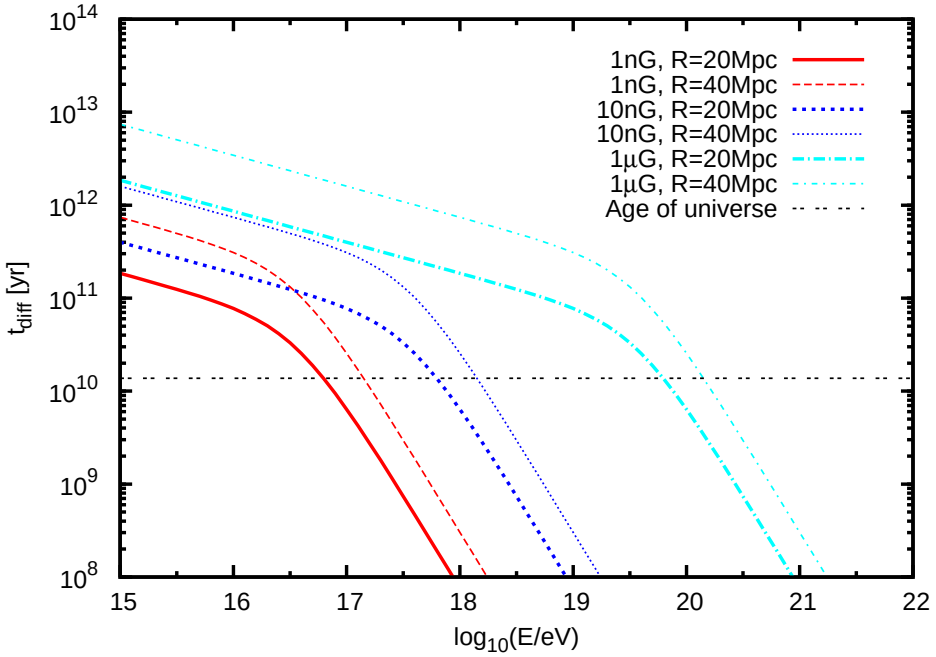

Figure 2.2: The time it takes cosmic ray protons to propagate through the supercluster when they are subject to diffusion. Different field strengths for $D(E)_{\text{Globus}}$ are used. The age of the universe, $t_{universe} = 1.37 \times 10^{10}$ yr is displayed, too.

Since the extragalactic magnetic field inside the supercluster is turbulent, the diffusion coefficient as suggested by [13] is used to calculate t_{diff}. The curves in figure 2.2 vary with magnetic field strength, as is indicated by the different colours, but also in the distance the protons have to propagate. For every field strength two possible propagation distances are considered. If the proton is ejected from a source inside the supercluster, the distance R equals the radius of the supercluster, 20 Mpc. If the protons are ejected from a source at the "other side" of the supercluster, the distance is 40 Mpc. The different distances are indicated as thick and thin lines. The fields range between nano- and microgauss size. The age of the universe, $t_{universe} = 1.37 \times 10^{10}$ yr, is also displayed, to compare the diffusion times t_{diff} with.
The first thing that can be observed in figure 2.2 is that there is no big difference between the different propagation distances. The curves lie close to each other, although the distance for the thin lines is twice as much as for the thick lines. The propagation distance is therefore not the most prominent factor that governs the diffusion time.

The magnetic fields have a larger influence: The red curves display the diffusion time for the case of $B = 1$ nG. One can see that in principle, protons with $E > 10^{17}$ eV are able to leave the supercluster, because their t_{diff} lies below the age of the universe. But both values are very close to each other, so only a small amount of those protons has left the supercluster during the evolution of the universe. More important are protons with energies of $E \sim 10^{18}$ eV, their t_{diff} is a lot shorter than $t_{universe}$. The diffusion coefficient $D(E)$ decreases with B-field strength, so for a fixed energy E the diffusion time becomes longer when B is increased. For $B = 1\mu$G the diffusion time for $E = 10^{18}$ eV in figure 2.2 is three orders of magnitude longer than for $B = 1$ nG. As $B > 1$ nG fields are considered, one sees also that the curves are shifted to higher energies. This is, because now only UHE protons are able to leave the supercluster. When the case of $B = 1\mu$G is considered, it is visible that only very energetic protons with $E \sim 10^{20}$ eV are able to propagate trough the supercluster. Lower energy protons diffuse in the supercluster and are "trapped" inside, because their diffusion time is longer than $t_{universe}$. It is therefore of great interest to investigate the spatial distribution of those protons within the supercluster.
The Auger experiment has detected cosmic ray particles with energies of more than $E = 10^{19}$ eV. The magnetic field strength at which protons with this energy will start to leak from the supercluster is $B = 10$ nG. These curves are displayed in dark blue in figure 2.2. So it can be assumed that the magnetic fields inside the supercluster are larger than 10 nanogauss. For the rest of this study the two values of $B = 10$ nG and $B = 100$ nG are considered when $D(E)_{\text{Globus}}$ is used. For this case, the UHE protons with energies up to $E = 10^{20}$eV do not escape the LSC, but diffuse instead and undergo interactions with interstellar gas and photons, which lead to the loss of energy. Both mechanisms have to be analyzed together.

2.3.2 The influence of magnetic fields

Since magnetic fields inside the supercluster influence the propagation of cosmic rays very strongly, some of their properties are discussed in this paragraph. Although several sources of magnetic fields are present inside the supercluster, there is only vague knowledge on the actual distribution, intensity or time evolution of those fields.
As mentioned in section 1.2, there are two regimes of magnetic fields, an ordered large scale component from relic processes and a turbulent smaller scale component, which is local. The ordered component comes from relic processes of the evolution of the universe, the turbulences are caused by the local galaxy environment. For the propagation of UHECR only the turbulent small scale fields are important, the ordered component is negligible. The basic idea is that protons scatter resonant on the turbulences of the fields and are therefore diffused. But this can only happen when the turbulent scale is of the same range as the gyroradius r_g of the proton. The interaction between wave and particle occurs only on a certain scale, so not all field components come into play. The turbulences of magnetic fields are caused by turbulences of the surrounding plasma. The main processes that lead to this are thought to be motion

of giant gas clouds, supernovae explosions and stellar winds. Those processes cause density fluctuations of the plasma , which in return cause electromagnetic fluctuations. In case of a supernova burst, the magnetic field is ejected into the interstellar medium along with the plasma from the star. Magnetic plasma is also constantly ejected by AGN, featuring fields of the size of fractions of micro Gauss. Important for the actual scattering are the maximal turbulent scale λ_{max} and the coherence length λ_c that corresponds to the distance over which the magnetic field is spatially coherent and shows only small fluctuations. The coherence length is usually in the order of λ_{max}.
The fields that are taken into consideration for this work are assumed to be turbulent, Kolmogorov-like. Such fields are characterized by a power-law dependence of the wave number k. The wave number is the magnitude of the wave vector $\vec{k}$ and depends on the length scale of the field turbulence $k = \frac{2\pi}{\lambda}$. The larger the turbulent scale, the smaller k and the field strength. Contrariwise, short scales λ yield larger k and larger magnetic fields. In the case of a Kolmogorov field, the power-law is k^q, with $0 < q < 1$, which is suggested by observations of the interplanetary medium, see for example [23].
Berezinsky et al. assume a turbulent magnetic field that comes from magnetic bubbles. The field arises due to galactic winds, see [4], page 165 that flow outwards and drag the magnetic fields along. The field freezes out and forms a bubble around the galaxy, the radius being of the order of the distance between the individual galaxies, $R_{bubble} = 1$ Mpc. Calculations in [4] show, that the fields produced in this way give gyroradii that are larger than R_{bubble} for UHECR, so protons are able to scatter off of those bubbles. For energies above $E = 5 \times 10^{19}$ eV even multiple scattering on separate bubbles is possible.
Globus et al. assumed a turbulent magnetic field, with a variance of $\sqrt{< \|\vec{B}^2\| >} = 10$ nG and a maximal turbulent scale of $\lambda_{max} = 1$ Mpc. The field has a Gaussian distribution with mean zero and a coherence length of

$$\lambda_c \simeq \frac{\lambda_{max}}{5} \simeq 0.2\,\text{Mpc}. \tag{2.18}$$

The factor 5 is convention, also lower values are possible. The power-law dependence of the wave number that was mentioned shows up in the equation for Globus' diffusion coefficient in equation 2.14 as $\sim E^{\frac{1}{3}}$.

2.4 Energy losses

As mentioned, cosmic ray propagation is governed by both, diffusion and energy losses. Both processes occur simultaneously and influence each other. This section is supposed to give details on the actual formulae that are used in order to calculate the energy losses.

2.4.1 Inelastic pp- scattering: UHE Protons and Interstellar gas (ISG)

Interstellar gas is located everywhere throughout a galaxy between the individual stars, thinning out as outer edges of the galaxy are reached. Its main component is hydrogen ($\sim$ 89%), followed by other light elements such as helium ($\sim$ 9%) and a little amount of heavy, metal like elements. Since hydrogen is subject to ionization, the interstellar gas contains many single protons. The UHE protons from the CR sources collide with these low energy gas protons, creating a Δ^+-resonance and produce new, less energetic, nucleons. In figures 1.6 and 1.7 in chapter 1 it could be seen that this are either protons and neutral pions or neutrons and charged pions. The Δ^+-resonance is excited only when the collision of the two protons has the threshold energy of $E \sim 1.2$ GeV. Otherwise, the regime of multipion production is entered, where the collision sets free several pions.

In this study, the energy loss experienced by cosmic ray protons due to collision with the ISG is calculated according to a formula by Mannheim and Schlickeiser in [20]:

$$-\left(\frac{dE}{dt}\right)_{pp} = \int_0^{\pi_{max}} dE_\pi \times P(E_\pi, E) = 0.65\, c\, n_{\mathrm{gas}} \sigma_{\mathrm{inel}} \theta\left[E - 1.22\ \mathrm{GeV}\right], \qquad (2.19)$$

where θ is a Heavyside function that equals one for $E > 1.22$ GeV. This value is the threshold energy that must be present in order to produce π-mesons, $E > E_{th} = m_p + 2m_\pi + \frac{m_\pi^2}{2m_p} \approx 1.22$ GeV. For the evaluation of equation 2.19 one needs detailed knowledge on the gas density of the ISG and the cross section σ_{inel}. It is assumed that a large fraction of the supercluster matter appears in the gaseous phase, where roughly 40% of the matter is to be found in the state of cold gas ($T < 10^5$ K) and the rest in warm or hot gas ($T > 10^5$ K). The observation of hot gas by Boughn et al. in [8] yields a value of $n_{\mathrm{gas}} = 2.5 \times 10^{-6}\mathrm{cm}^{-3}$ for the density of the ISG. This is consistent with simulations by Kravtsov et al., see [14] and therefore the chosen value for the proton-proton collisions in this study. The cross section for the pp-interaction is larger than the one for $p\gamma$-processes, therefore one could assume that pp-interactions dominate the energy losses. But as will be seen in figure 2.7, pp-collisions are almost independent of the energy of the UHE protons and this prevents the process from domination. Details on the influence of the cross section can also be found in [22].

2.4.1.1 Cross section and Inelasticity

For the cross section σ_{inel} of the interaction an equation from Kelner et al. in [18] is used. In this paper, they give a parametrization to the cross section for the pp-collision as follows:

$$\sigma_{\text{inel}}[\text{mb}] = 34.3 + 1.88L + 0.25L^2 \times \left[1 - \left(\frac{E_{th}}{E}\right)^4\right]^2, \tag{2.20}$$

where $L = \ln\left(\frac{\text{E}}{1\text{ TeV}}\right)$. This is a fit to experimental data and numerical simulations of proton-proton interactions. The simulations are performed with the SIBYLL code, which is a public available code for simulating particle interactions, see [10] for details. Figure 2.3 shows the course of the cross section, as a function of the proton energy E (or E_p as it is labeled in the figure). The closed dots represent experimental data from *http:wwwppds.ihep.su:8001/c5-5A.HTML*, the open dots the SIBYLL simulations. The solid line is the parametrization from equation 2.20.

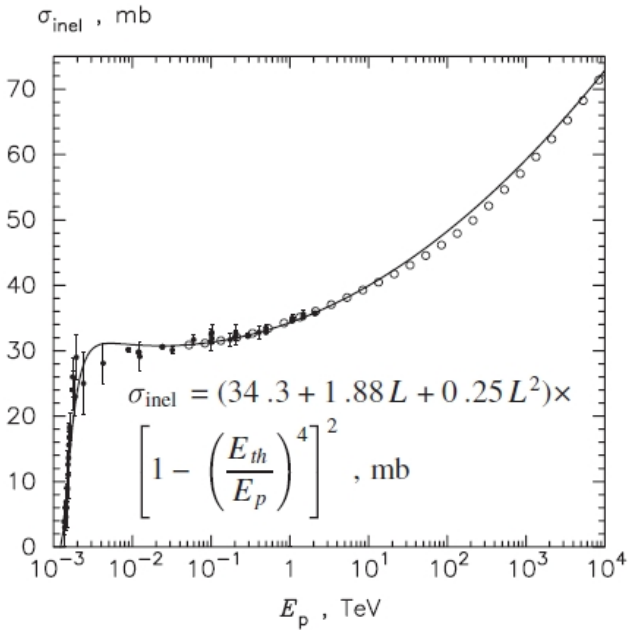

Figure 2.3: Inelastic cross section σ_{inel} of pp collisions. The solid line indicates the parametrization from equation 2.20, the closed points are from *http:wwwppds.ihep.su:8001/c5-5A.HTML*. The open points are calculations with the SIBYLL code.

The interaction sets in when $E_p > 1$ GeV, the cross section being approximately 30 mb. Then the cross section increases gradually. Although the figure displays only energies up to $E = 10^{16}$ eV, the parametrization can be used for a wider energy range, see [18], as is done in this study.
Another important factor for the calculation of energy losses is the inelasticity K of an interaction. This parameter describes the relative amount of energy that is lost during an interaction, $\frac{\Delta E}{E}$, having values of $0 < K < 1$. This energy is transferred to the secondary particles, in the case of pp-collisions pions and nucleons. In [20], Mannheim assumes that the initial energy is bisected between the secondary particles,

$K = 0.5$. This assumption is already implemented in equation 2.19. The detailed derivation of this expression can be found in [20].
The results of the energy loss due to pp-collisions are presented in figure 2.7, which displays the time the protons need in order to drop to $1/e$ of their initial energy. Proton-proton collisions are rather easy to calculate, σ_{inel} and n_{gas} can simply be inserted in equation 2.19.
The case for pion and electron-pair production is more complicated and needs some more attention.

2.4.2 Inelastic $p\gamma$- scattering: Photopion production

As seen in figures 1.8 and 1.9 in chapter 1, the production of pions does not only occur when an UHECR proton collides with a gas particle, but also when it collides with a photon from ambient gas. Thus the resulting π-meson has often the name photopion. This happens, because in an extragalactic environment the number density of such low-energy photons is often higher than the density of ambient gas. Hence photon-induced reactions dominate the interaction of UHE protons, see also [9]. Similar to the interaction with interstellar gas, the intermediate step in $p\gamma$-collisions is an excitation of a Δ^+-resonance, if the threshold energy for this is reached. If more energy than the threshold energy is present, the regime of multipion production is entered. The formula that is used for the energy loss calculations for this process is also taken from [20]:

$$-\left(\frac{dE}{dt}\right)_{p\gamma} = \frac{m_p c^3}{2\gamma_p} \times \int_{\frac{\varepsilon_{th}}{2\gamma_p}}^{\infty} d\varepsilon n_\gamma(\varepsilon)\varepsilon^{-2} \times \int_{\varepsilon_{th}}^{2\gamma_p\varepsilon} d\varepsilon'\varepsilon'\sigma(\varepsilon')K_p(\varepsilon'). \tag{2.21}$$

To understand the physical value of this expression it is instructive to take a closer look at this double integral.
The expression consists of one integral that covers the energy densities of the photon fields $n(\varepsilon)$ and another that accounts for the different angles of the incoming photons. If a photon of a certain energy ε collides head-on with a proton, the centre-of-mass energy E_{CM}, which is present in the rest frame of the proton, has its maximal value (see appendix A for a detailed calculation). The value of E_{CM} decreases as the collision angle becomes larger, reaching its minimal value when proton and photon are collinear. This dependence on the incident angle is accounted for by the ε'-integration. At the same time this also handles the change in the cross section, since $\sigma(\varepsilon')$ is actually $\sigma(E_{CM}(\varepsilon'))$ and therefore dependent on E_{CM}. This dependence is presented in the short derivation below. E_{CM} is calculated from the square of the sum of four-vectors ($p = (\varepsilon, \vec{p})$) of the colliding photon and proton. A photon is massless and the collision happens in the rest system of the proton; accordingly $m_\gamma = \vec{p_p} = 0$:

$$\begin{aligned} E_{CM}^2 &= (p_\gamma + p_p)^2 \\ &= \underbrace{m_\gamma^2 c^4}_{=0} + m_p^2 c^4 + 2\varepsilon_\gamma \varepsilon_p - \underbrace{2\vec{p_\gamma}\vec{p_p}c^2}_{=0} \\ &= m_p^2 c^4 + 2\varepsilon_\gamma \varepsilon_p \\ &= m_p^2 c^4 + 2\varepsilon' E_p \quad \text{with nomenclature from 2.21} \\ &= m_p^2 c^4 + 2\varepsilon' m_p c^2 \quad \text{since the proton is at rest} \end{aligned} \tag{2.22}$$

The integral over the photon energy $d\varepsilon$ is necessary, because photon fields in general contain a broad spectrum of photon energies. This is addressed in an energy dependent number density $n(\varepsilon) = \frac{dN}{dV\, d\varepsilon}[\mathrm{m}^{-3}\mathrm{eV}^{-1}]$.
The three different photon fields that are considered in this thesis all lead to the same reaction products. But the probability for the interactions differs among the fields, because they have different spectral energy distributions. Hence they interact with protons of different energies to provide the necessary threshold energy.
Information on the individual evolution of fields and their impact on the pion production and is given in section 2.5. A detailed derivation of equation 2.21 can be found in appendix B.

2.4.2.1 Cross section and Inelasticity

The cross section and inelasticity are major influences on the "effectiveness" of $p\gamma$-interactions as they are for pp-collisions. The larger σ or K are, the more likely it is that inelastic collisions actually take place. They appear in the energy loss formula in the $d\varepsilon'$-integral.
In [18], Kelner et al. present a plot of the cross section, as it is determined by calculations with the SOPHIA code. This code uses Monte Carlo simulations of hadronic interactions with radiation fields to study the different parameters of the reaction. The results of the calculations are presented in figure 2.4, along with a parametrization of the cross section. One sees that σ rises rapidly as the threshold energy is approached, resulting in a large peak of almost 0.6 mb at the Δ^+-resonance when ε' equals 0.3 GeV. Afterward it descends to ~ 0.14 mb and slowly increases as the photon energy in the rest frame ε' continues to rise. After the Δ^+-peak the regime of multi-pion production is entered, which can be seen in the rise for $\varepsilon' > 100$ GeV.
However, Kelner et al. do not give a fit in their paper, this is taken from the Particle Data Group web page, *http://pdg.lbl.gov/2010/reviews/rpp2010-rev-cross-section-plots.pdf*. There a parametrization for the total cross section of $p\gamma$-collisions is given:

$$\sigma(E_{CM}^2) = \alpha + \frac{\beta}{(E_{CM}^2)^\gamma} + \delta \times (\zeta + \ln(E_{CM}^2))^2. \tag{2.23}$$

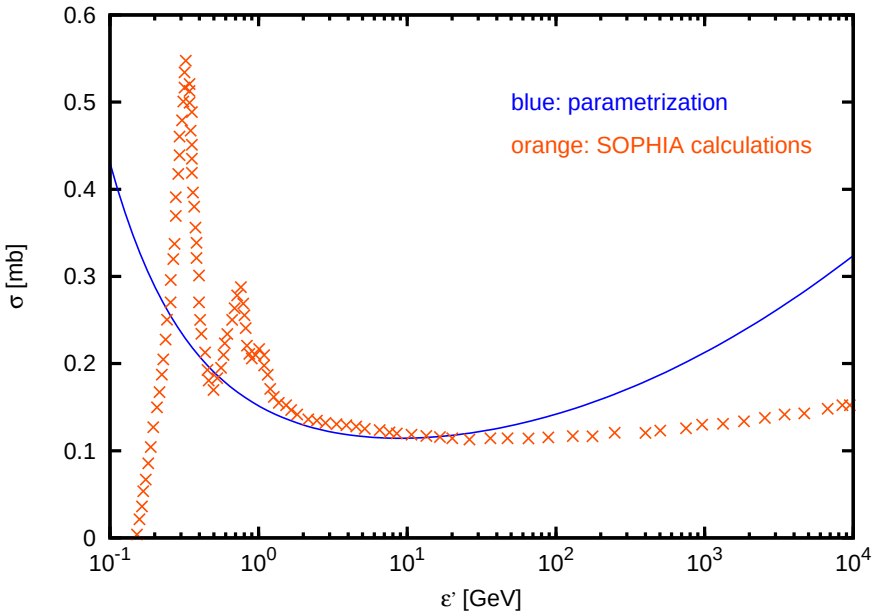

Figure 2.4: The orange dots display the total cross section for $p\gamma$-collisions as is is determined with SOPHIA calculations in [18]. The blue curve represents the parametrization of $\sigma_{p\gamma}$, with equation 2.23.

The used values are presented in the following table:

α	0.10908323347151504
β	0.03165050238465333
γ	0.458147574571271
δ	0.0009474657178335319
ζ	-3.3644184990774306

Table 2.1: The parameters of equation 2.23, taken from *http://pdg.lbl.gov/2010/reviews/rpp2010-rev-cross-section-plots.pdf* .

The parametrization in equation 2.23 describes, except for the strong peak at the Delta-resonance, the course of $\sigma_{p\gamma}$ in figure 2.4 well. At $\varepsilon' = 0.5$ GeV it starts with $\sigma \sim 0.2$ mb, decreases slightly for higher ε' and starts to grow again as values of $\varepsilon' > 10$ GeV are approached. The only difference occurs for very high photon energies, when $\varepsilon' > 100$ GeV. At this point the parametrization yields higher cross sections than figure 2.4 proposes. The values are bigger by a factor 1.5–2.0.
For the calculations with equation 2.21, the following values for inelasticity and cross section are used:

$0.2\,\text{GeV} < \varepsilon' < 0.5\,\text{GeV}$:

$$\begin{aligned} \sigma &= 0.34 \ \ \text{mb} \\ K &= 0.2 \end{aligned} \tag{2.24}$$

and for $\varepsilon' > 0.5$ GeV:

$$\begin{aligned} \sigma(E_{CM}^2) &= \alpha + \frac{\beta}{(E_{CM}^2)^\gamma} + \delta \times (\zeta + \ln(E_{CM}^2))^2. \\ K &= 0.3 \end{aligned} \tag{2.25}$$

For energies around the threshold energy for the Δ^+-resonance a constant value of the cross section of $\sigma = 0.34$ mb is assumed. The inelasticity is assumed to be $K = 0.2$. For higher energies the cross section is then described by the parametrization in equation 2.23, since those values correspond well to figure 2.4 for $\varepsilon' > 0.5$ GeV. The inelasticity is set to $K = 0.3$.
Berezinsky et al. use different numbers, they choose a constant inelasticity of $K = 0.5$ throughout the entire energy range of ε'. For $E \gg 3 \times 10^{20}$ eV they use a cross section of $\sigma \approx 1 \times 10^{-28}\text{cm}^2$ which equals 0.1 mb. Below this energy they use $\sigma(\varepsilon') = \sigma_0(\frac{\varepsilon'}{\varepsilon_{th}} - 1)$, where $\sigma_0 = 4 \times 10^{-28}\text{cm}^2$ and $\varepsilon_{th} = m_\pi$. Both values can be found in [4], page 128 ff. Since the energy loss results $\left(\frac{dE}{dt}\right)_{p\gamma}$ depend strongly on the cross section and the inelasticity, there will be different values for $\left(\frac{dE}{dt}\right)_{p\gamma}$ when the results of Berezinsky et al. and this study are compared. The chosen values for K and $\sigma_{p\gamma}$ in this study are larger than the ones Berezinsky et al. use, thus the energy losses will be larger, too. This can be seen as the results for the spatial proton densities are compared in section 4.3.

2.4.3 Inelastic $p\gamma$- scattering: Pair production

Next to pion production, the process of pair production has to be investigated when dealing with $p\gamma$-interactions. The calculations in this study are based on computational work by Tanja Kneiske and go back to the paper of George R. Blumenthal, who derived in [7] the essential formula for the reaction of any CR with atomic number A ($A + p \rightarrow A + e^- + e^+$) that produces an electron-positron pair:

$$-\frac{dE}{dx} = \alpha r_0^2 Z^2 (m_e c^2)^2 \int_2^\infty d\xi \; n\left(\frac{\xi m_e c^2}{2\gamma_p}\right) \frac{\phi(\xi)}{\xi^2}, \tag{2.26}$$

where m_e is the electron mass, Z the charge, r_0 the classical electron radius and $\alpha = 1/137$. In this thesis only the case for protons is considered. The full derivation of the used formula can be found in [7].
If the situation of the laboratory frame in figure 2.5 is considered, one can see that

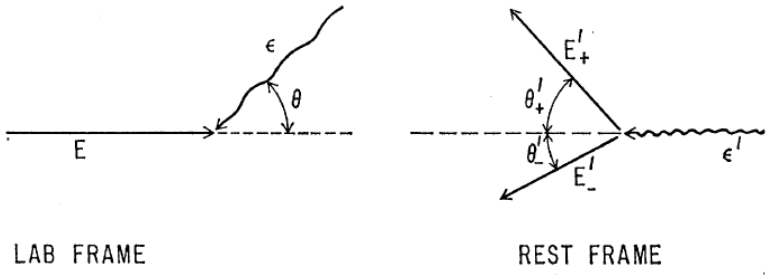

Figure 2.5: The pair production process in the laboratory and rest frame of the proton as presented in [7]. The picture on the left shows the collision of proton and photon as is seen in the laboratory frame. The right picture illustrated the final situation in the rest frame of the proton after e^- and e^+ have been produced.

the argument of the incident angle, that was given in the previous paragraph on pion production, holds here also. In a head-on collision, when $\theta = 0$, the centre-of-mass energy reaches its maximal value. For a larger incident angle θ it decreases. The threshold energy that is necessary for the interaction to take place is $\varepsilon' > 2m_e c^2$, the energy for the production of the $e^- e^+$-pair. It is naturally a lot lower than the one for pion production, so the pair production process sets in for lower proton energies. The generated electron and positron have an energy of E'_- and E'_+ and form exit angles of θ_- and θ_+, respectively. The energy loss equation that is presented in [7] is derived for an isotropic distribution of photons. This can be seen in the integrand of the ξ-integral of equation 2.26. When this formula is compared to equation 2.21, it stands out that both expressions have the same form of the integrand for the integration of photon energies, $\frac{n(\varepsilon)d\varepsilon}{\varepsilon^2}$ and $\frac{n(\xi)d\xi}{\xi^2}$. The equations look similar, since they principally describe same physical situation. In both cases a high energy proton interacts with a photon from an isotropic background field, only the reactions products and the kinematic values differ.
The integrand for the pair production equation, $\phi(\xi)$ contains the inelasticity and the cross section. To be able to calculate the energy loss per unit time traveled (instead of unit distance) one has to multiply equation 2.26 by the speed of light c.

2.5 Photon fields

Radiation fields play a great role in terms of pion and pair production in $p\gamma$-collisions. Therefore the three fields that are taken into account in this study are discussed here once more.

The Cosmic Microwave Background

The CMB is a radiation field that is present throughout the entire universe and is described very well by a blackbody spectrum of temperature of $T = 2.75$ K. It is a

relic radio field that originated from the transition of the universe from an opaque to a transparent state, when photons decoupled from matter. The photons were set "free" at this point and followed the overall evolution of the universe. The photons cooled down while the universe expanded until they reached today's temperature. The CMB appears as an isotropic, almost constant field and has only very small fluctuations in the range of $\frac{\Delta T}{T} = 10^{-5}$. It is described by a Planck distribution

$$\frac{n(\varepsilon)}{\varepsilon^2} = \frac{1}{(\hbar c)^3}\frac{1}{\pi^2} \times \left(\frac{1}{e^{\left(\frac{\varepsilon}{kT}\right)} - 1}\right) \tag{2.27}$$

and enters the loss integrals when the integral over all possible photon energies $d\varepsilon$ is evaluated. It significantly contributes to the energy losses. For proton energies $E > 10^{19}$ eV the interactions with the CMB yield the dominant reaction process, inducing the GZK-cutoff that was mentioned in chapter 1 before.

The Extragalactic Background Light

Contrary to the cosmic microwave background, the EBL and the SCRF are not universal, but influenced by many different sources such as galaxies and stars. The extragalactic background radiation field is a diffuse multiwavelength field originating from galaxies in and outside the supercluster. Objects from every epoch, from first stars up to present galaxies, contribute to the EBL. Within the supercluster, the EBL can be assumed as constant. Its spectral energy distribution is shown in figure 2.6. In this distribution there are clearly two distinct peaks visible. The one at wavelength $\lambda = 1\mu$m represents the cosmic ultra-violet (UV) background, the other at $\lambda = 100\mu$m represents the cosmic infrared (IR) background. The latter originates from starlight that is absorbed by dust in galaxies and then re-emitted in the infrared wavelength band. The UV- contribution comes from UV radiation that fills the universe since the reionization epoch. Most radiation comes from previous generations of massive stars and quasars.

The Supercluster Radiation Field

The supercluster radiation field is similar to the EBL. It is produced by the galaxies inside the supercluster and gives rise to an almost constant field between the individual galaxies. It has to be taken into account, because there are many individual galaxies in the supercluster and they are close to the source of UHECR protons. The photons from the supercluster galaxies are present in the propagation region of those protons and influence immediately the proton propagation. Their contribution can simply be added to the already mentioned fields.

For the calculations with SCRF and EBL, limits on the individual spectral energy distributions of the two fields were used. These come from studies by Tanja Kneiske, see [19]. The photon fields she provided are displayed in figure 2.6.

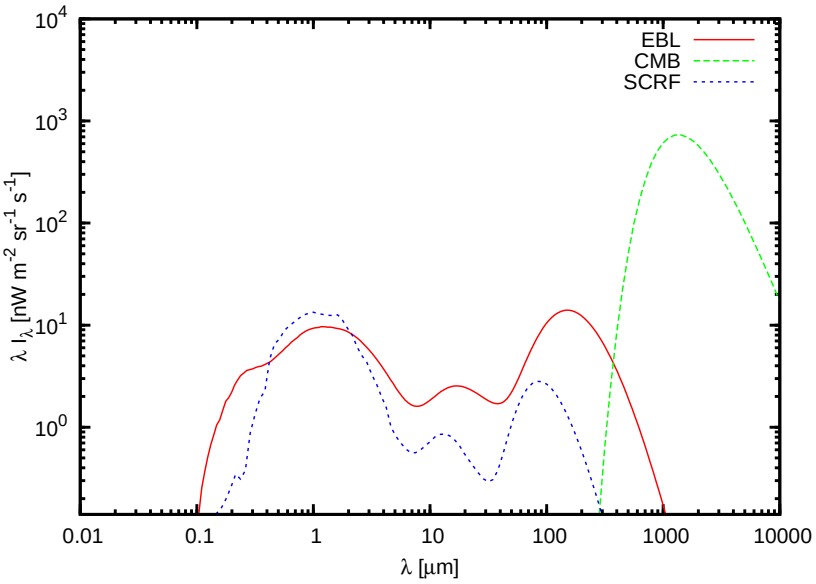

Figure 2.6: Spectral energy distribution of the photon fields used in this study. The EBL and SCRF data come from models by Tanja Kneiske, see [19].

In this figure one can see the spectral energy distributions of the three different fields. Not only the EBL, but also the SCRF has maximal values in the UV and IR region. Besides, one can see that a smaller peak is present for wavelengths of $\lambda \sim 10\mu$m. This is called the optical background. The shape of the EBL and SCRF distributions are very similar, but the EBL lies slightly higher. This influences the energy losses and can be seen in figure 2.7, too.
The CMB has a different shape. Its maximal value lies in the microwave range and clearly dominates in this region. Its peak lies about two orders of magnitude above the contribution from EBL and SCRF at a photon energy of $\varepsilon \sim 10^{-3}$ eV. In terms of energy losses it has the most impact, because its high frequency tail provides just the right photon energy to produce π-mesons with UHE protons. This lead to significant energy losses and is shown in figure 2.7 as well.

2.6 Energy loss results

In figure 2.7 the time t_{loss} is displayed, which elapses until the initial energy E of a proton has dropped to $1/e$. This timescale is approximated with the expression

$$t_{\text{loss}} = E \times \left(\frac{dE}{dt} \right)^{-1} . \tag{2.28}$$

As a guideline the age of the universe is also displayed. Figure 2.7 shows the loss times for all interactions that were mentioned in this chapter: inelastic proton-proton

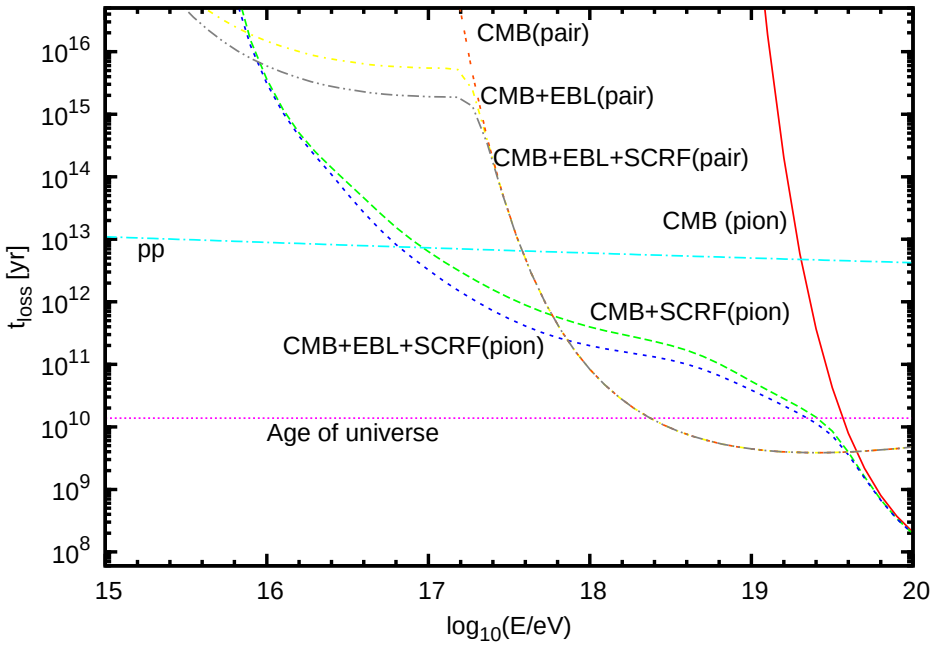

Figure 2.7: Loss times $t_{\text{loss}} = E \times (\frac{dE}{dt})^{-1}$ as a function of proton energy E. The loss times for the UHECR protons are calculated with equations 2.19, 2.21 and 2.26.

collisions and proton-photon collisions that lead to the production of pions or electron-positron pairs. For the interactions with photons, the contributions of the CMB alone and the addition of the other two photon fields are displayed:

$$\frac{dE}{dt} = \left(\frac{dE}{dt}\right)_{CMB} + \left(\frac{dE}{dt}\right)_{EBL} + \left(\frac{dE}{dt}\right)_{SCRF}. \tag{2.29}$$

The energy losses due to collisions with the interstellar gas, which are displayed in light blue in the figure, have almost no effect on the UHE protons. The corresponding loss times lie many orders of magnitude above the age of the universe. This means that in a physically significant time they have not experienced a loss of energy and proton-proton collision can therefore safely be neglected. Moreover, a feature that was addressed in section 2.4.1 can be seen in the figure. The energy losses $\frac{dE}{dt}$ and therefore also the loss times are indeed almost independent of the proton energy E. The curve for t_{loss} is nearly constant throughout the entire range of ultra-high energies.

The red, blue and green curves represent the energy losses due to pion production. The red curve describes the losses that are caused by the interaction of protons and CMB photons only. The green and blue curves add the contributions of the SCRF and the EBL. As mentioned in the previous section, the influence of these two radiation fields is similar, because their energy distributions are similar, too. In appendix A the calculations show that the threshold energy for pion production in the centre-of-mass frame is 145 MeV. Since the maxima of the SCRF and the EBL are in the UV and IR energy range, both provide photon energies that lead to the

needed threshold energy when the photons collide with protons of $E < 10^{19}$ eV. In figure 2.7 it is visible that the EBL has a higher energy density than the SCRF. If the green and blue lines are compared, one can see that when the EBL is added, t_{loss} decreases significantly. There are more EBL photons present, thus more protons collide with them. However, for energies below $E = 10^{18}$ eV, the impact of the EBL and SCRF becomes smaller and smaller. Only at energies slightly below the GZK cutoff do they play a significant role.
For proton energies above $E = 10^{19}$ eV the CMB dominates pion production, although the CMB consists of low-energy photons. The mean energy of a CMB photon is $\langle\varepsilon\rangle = 7 \times 10^{-4}$ eV, this corresponds to a proton energy of $E \approx 10^{20}$ eV to provide the needed centre-of-mass energy. But due to the high-frequency tail of the Planck distribution, pion production sets in at lower proton energies already. The GZK-cutoff shows up at $E = 6 \times 10^{19}$ eV. The corresponding loss times (red curve) decrease steeply at this energy. This is caused by the energy distribution of the CMB photons, which is steep too, see figure 2.6. Besides, the cross section influences t_{loss} also. In section 2.4.2.1 one can see that there is a sharp rise in the cross section at the region of the Δ^+-resonance. This lead to a sudden rise in $\frac{dE}{dt}$ and a decrease in the energy loss times above $E = 10^{19}$ eV.

The orange, yellow and grey curves show the loss times for pair production. Like before, the CMB alone and the addition of the other radiation fields are presented. As for the case of pion production, the CMB photons have the largest influence on t_{loss}. The threshold value for pair production lies below the one for pion production. In [20] the necessary proton energy is given by $E = 7 \times 10^{17}$ eV, so this process will set in at smaller proton energies. The orange curve approaches the age of the universe for this certain energy. But pair production becomes a significant loss process only at $E > 10^{18}$ eV. The reason for this is the inelasticity of the process. The cross section for pair production is quite large, but K is small ($K < 0.2$), so only little energy is transferred to the e^+e^--pair. The protons keep much of their initial energy, this limits the "effectiveness" of the interaction in terms of the proton's energy loss. Thus photopair production does not dominate $p\gamma$-interactions. As for the pion production, the other two radiation fields lead to different t_{loss} curves, but there is not such big influence. Contributions of the EBL and the SCRF are negligible for pair production, because t_{loss} lies below the age of the universe only for interactions with CMB photons.

Chapter 3

Implementation

3.1 Setting the boundaries for the spatial proton density $n(E, r, t)$

It's a long way to the top (if you wanna Rock' n' Roll).
From the album *T.N.T.* by AC/DC

The calculations in this thesis are performed using a code in the programming language C, which was written during the months of this study. It contains all parameters for the solution for $n(E, r, t)$ that were discussed in the last chapters. But as one more look at expression 2.4 is done, one notes that every parameter except the integral boundaries has been discussed. As mentioned in section 2.1, this relation connects the energy at observation E with the energy the CR proton had when it was generated in the source via

$$\begin{aligned} E_g &= \lambda(E,t) \times E \qquad \text{or} \\ E_g &= \lambda(E, t-T) \times E. \end{aligned} \tag{3.1}$$

E_g describes the energy the cosmic ray protons hold when the source is "switched on" at $t = 0$. Energy E stands for the energy at arrival, after a certain amount of time has passed and the protons have propagated to Earth. The expression $\lambda(E,t) \times E$ describes a certain E_g that a cosmic ray proton started with and can have different values, according to the individual processes that occur during the propagation.
The amount of energy a proton has at a certain time depends on its interactions. In the last chapter, the problem of energy losses was thoroughly discussed — now they become once more important. The integral in equation 2.4 sums up all contributions from those protons that reach the Earth with the energy E at a certain time. Since they may undergo different interactions, there are several "starting" values of E_g that lead to the same E after the propagation time t has elapsed.

Before further discussion of the individual time scales is presented, it is important to know that the nomenclature changes for the rest of this study. Instead of t for the propagation time and T for the source pulse length, the variables t_f (= final propagation time) and P (= pulse length) are used.

The time, a cosmic ray proton propagates from source to Earth depends on the point in time, when it was ejected from the source. The maximal possible propagation time follows from the ejection of the proton at the "switch on" of the source. Note that t_f and P start at the same time $t = 0$, but P is in general shorter than t_f. After a time P, when the source is "switched off", the ejected protons propagate until t_f has elapsed. Therefore t_f is called the propagation time. Contrary to this, the minimal propagation time occurs at $t_f - P$, when protons are ejected at the "switch off" of the source. The longer the propagation time for the proton is, the more interactions take place and the more energy is lost. In equation 2.4, the arrival energy is fixed, so the protons that are detected with a fixed $E(t)$ must have had different starting energies E_g. Accordingly, the different propagation times set natural boundaries on E_g. The lowest possible E_g arises for the propagation time of $t_f - P$, so this is the lower bound of the integral in 2.4. The upper bound of the integral, the highest possible E_g, is therefore described by a propagation time of t_f. If t_f and the pulse length P are identical one speaks of a continuous source.
The crucial point is the determination of E_g. For the calculations of the spatial proton density, only the arrival energy E, the time the proton has propagated and the interactions it may have been subject to, $b(E)$, are known. But to solve equation 2.4, it is necessary to "calculate back" to the energy with which the proton was released from it source, E_g.
To begin with, the actual *energy losses*, starting from a fixed energy at generation ($E_g = const.$) of the proton are calculated. The energy evolution is calculated along the characteristic of E. This is done, because $b(E)$ is defined as an energy loss:

$$b(E) = -\frac{dE}{dt} \tag{3.2}$$

Besides, those results can be checked against the t_{loss} results from figure 2.7. The results and the discussion are presented in section 4.1.
The starting point of the calculations for energy losses is equation 3.2, which consists of the different expression for $\frac{dE}{dt}$, given in equations 2.19, 2.21 and 2.26. For a better understanding the term for pion production between a proton of energy E_p and a photon of energy ε is presented here once more:

$$-\left(\frac{dE_p}{dt}\right)_{p\gamma} = \frac{m_p c^3}{2\gamma_p} \times \int_{\frac{\varepsilon_{th}}{2\gamma_p}}^{\infty} d\varepsilon n_\gamma(\varepsilon)\varepsilon^{-2} \times \int_{\varepsilon_{th}}^{2\gamma_p\varepsilon} d\varepsilon'\varepsilon'\sigma(\varepsilon')K_p(\varepsilon'). \tag{3.3}$$

The different parameters were discussed already, but the important feature of this equation is that $b(E) = -\dot{E}$ is given in a form that cannot be solved analytically. Moreover, the right-hand side of expression 3.3 has no explicit time dependency, but

depends only on the energy E_p of the cosmic ray proton. Therefore, this integro-differential equation has to be solved numerically. To do this the energy losses have to be assumed as continuous. Until now, it did not matter, if the protons lose their energy in several interactions or just one. But to be able to solve the differential equation, the assumption of a continuous loss is necessary. The calculation is is done by using available tools from the GNU scientific library (gsl). The used routine for solving the ODE is the Bulirsch-Stoer method. A detailed presentation of the implementation is left to appendix C, as it might be helpful for someones future work. The next step of the calculation is to modify the code in such a way that it is able to calculate back from a given E to the original $E_g(t)$. The loss processes are calculated back in time, and the energy loss turns into an *energy gain*, $\dot{E} > 0$. With this the final results for the spatial proton density, $n(E, r, t)$ can be calculated. They are checked against the results of calculations from Berezinsky et al. in section 4.3. With the comparison, one is able to see if the ODE was solved correctly. After the check of the correct implementation, the EBL and SCRF contributions can be considered.

3.2 Details on Numerics

3.2.1 Planck distribution

An important parameter in equation 3.3 is the Planck distribution $n(\varepsilon)$, which describes the spectral density distribution of the cosmic microwave radiation. This distribution is given by

$$n(\varepsilon) = \frac{\varepsilon^2}{\pi^2} \frac{1}{(\hbar c)^3} \times \frac{1}{\left(e^{\left(\frac{\varepsilon}{kT}\right)} - 1\right)}. \tag{3.4}$$

In equation 3.3 it is integrated over the photon energy ε. As long as $n(\varepsilon)$ has "proper" values, the integral yields good results. But when the proton energy E_p rises to very high values, the energy of the matching photon to produce the necessary threshold energy can be very low. In that case, when $\varepsilon \to 0$, the exponential function in equation 3.4 becomes one and this causes numerical problems in the calculation. This happens for the boundary calculations of equation 2.4 when large E_g appear. This problem can be solved by the Rayleigh-Jeans law: the problematic term, $e^{\frac{\varepsilon}{kT}}$, is approximated such that the exponent is expanded for small values:

$$e^x = 1 + x + \frac{x^2}{2} + \dots \tag{3.5}$$

If this is inserted back into 3.4 one gets:

$$n(\varepsilon) = \frac{\varepsilon kT}{\pi^2(\hbar c)^3.} \tag{3.6}$$

This expression can handle small values of ε, as long as $\varepsilon > 0$. In the C-code this expression of the photon density $n(\varepsilon)$ is used whenever $\frac{\varepsilon}{kT} < 10^{-5}$.

3.2.2 Limit on E_g

The calculation that provides the proton density can calculate back to any arbitrary $E_g(t)$. But a maximum energy of $E_{\mathrm{g,max}} = 1.22 \times 10^{28}$ eV, the Planck energy, is chosen, simply because this is one of the biggest possible energies in a physical context. Usually astronomical objects accelerate particles only up energies of $10^{21} - 10^{22}$ eV, but there can be in principle particles with higher energies. This could be relic particles from early epochs of the universe or particles that have gained their energy in decays. The Planck energy is defined by $E_{\mathrm{Planck}} = \sqrt{\frac{\hbar c^5}{G}}$, where G is the gravitational constant ($G = 6.67 \times 10^{-11}\,\mathrm{m^3 kg^{-1} s^{-2}}$) and $\hbar$ the Planck constant ($\hbar = 1.05 \times 10^{-34}\,\mathrm{Js}$). Since the boundaries of the density integral depend on E_g, the idea was to use this dependency to check how big E_g can be assumed. The results of the calculations from this study were compared with the Berezinsky results. The obtained results showed that it does not matter if $E_g(t)$ is of the order of 10^{25} eV or 10^{28} eV, so $E_{\mathrm{g,max}} = 1.22 \times 10^{28}$ eV has been implemented in the C-code.

3.2.3 Limit on $D(E)$

As seen in equations 2.13, 2.14 and figure 2.1, the diffusion coefficient is a continuous function of the proton energy E. It can have arbitrarily high values if E is large enough. Protons with larger $D(E)$ propagate faster through space. But the speed of light set a natural boundary on the diffusion coefficient. Looking at equation 2.12, this can be converted to $\frac{R}{t} = \frac{D(E)}{R}$. Now, $\frac{R}{t}$ yields the velocity with which the protons propagate. If this is taken to be less than the speed of light, the diffusion coefficient has to satisfy

$$D(E) < R\,c. \tag{3.7}$$

With a given distance R to the particle source the coefficient $D(E)$ is limited. For the radius of the supercluster, $R = 20$ Mpc, this yields a diffusion coefficient of $D_{\mathrm{max}} = 1.8 \times 10^{35}\,\mathrm{cm^2 s^{-1}}$. But since also smaller distance of just a few megaparsec are to be considered, a maximal diffusion coefficient of $D_{\mathrm{max}} = 3 \times 10^{35}\,\mathrm{cm^2 s^{-1}}$ is chosen for implementation. The course of the individual $D(E)$ and $D(E)_{\mathrm{max}}$ is shown in figure 3.1.

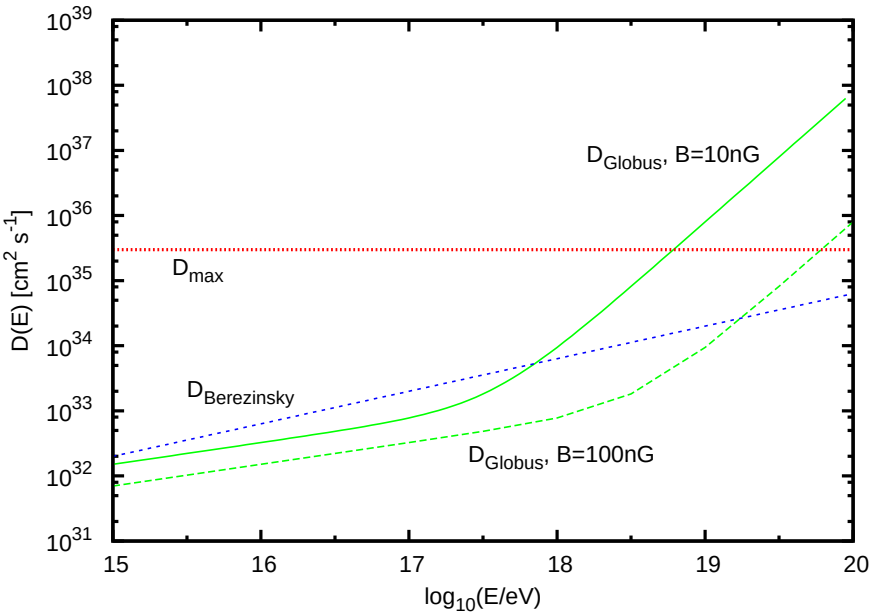

Figure 3.1: The course of the different diffusion coefficients used in this study and $D_{\max} = 3 \times 10^{35}\,\mathrm{cm^2 s^{-1}}$ that is chosen for the calculations.

From the x-axis of figure 3.1, one can tell the energy at which the limitation sets in. For a magnetic field of $B = 10$ nG this happens at $E \sim 10^{18.7}$ eV, for $B = 100$ nG at $E \sim 10^{19.7}$ eV. The diffusion coefficient Berezinsky et al. use is not influenced by the limitation.

Chapter 4

Results

4.1 Characteristics for E(t)

In the following paragraphs, the energy loss calculations as discussed in chapter 3 are presented. Then the actual spatial density distribution results are shown. The comparison between the results of this study and the ones from Berezinsky et al. is made and the influence of certain parameters, such as P, t_f and B is studied.

The first calculations are concerned with the time evolution of the proton energy if only pion photo-production takes place. The calculations are done for different initial energies E_{in}, which characterize the energy from which the evolution starts at $t = 0$. Before adding the EBL and SC radiation field, it is interesting to know how the loss process affect the time evolution in general, so first only CMB photons are examined. Equation 2.21 is used as energy loss and the ODE solved for this expression. Since this reaction leads to the GZK-cutoff, the losses should only be significant for energies well above 10^{19} eV. The results of the first calculations are presented in figure 4.1.
One sees clearly the effect of the GZK-cutoff in this figure, lower energy protons are not influenced very much. When, exemplary, the curve for protons of an initial energy $E_{\text{in}} = 10^{19.8}$ eV is taken into consideration, one can tell from figure 4.1 that they lose only a small amount of their initial energy. The reason is that this E_{in} lies just above the threshold energy for the $p\gamma$-collisions with CMB photons, so these protons are not influenced by this process very much. For smaller energies the influence is even lower. When one looks at protons of energies around $E_{\text{in}} = 10^{19}$ eV, it can be seen that they experience no influence due to $p\gamma$-interactions, because they simply do not provide enough centre-of-mass energy to produce π-mesons.
Looking at higher energies, the pictures changes. The curve of $E_{\text{in}} = 10^{22}$ eV, for example, falls off steeply towards lower energies, because there the $p\gamma$-interaction starts to play a role. The curve looks constant in the beginning, but this is a result of the continuous loss assumption and of the logarithmic scale of $E(t)$. In principle it could decrease also after a short time t, but for the continuous loss assumption this happens only for larger t. The curve is therefore not constant, it only changes

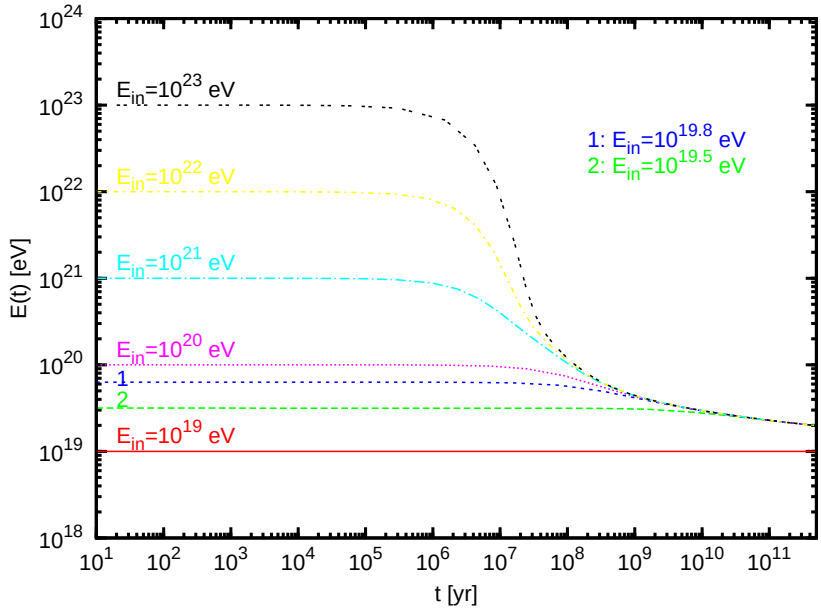

Figure 4.1: The characteristic of $E(t)$ due to reactions with CMB photons for various initial energies E_{in}. The calculations are done with the method discussed in chapter 3.

very slowly. It should be noted that although it looks as if all curves converged to one single line, this is not the case. Every $E(t)$ curve has its own characteristic. A zoom deep into the region above the time of $t = 10^{10}$ yr, would show the individual curves. They lie very close to each other, but every line is determined by its individual starting value E_{in}.
The results in figure 4.1 seem reasonable, but to be reassured of the correctness of the calculations, one can check the ODE solutions against previous results.

For this, it is instructive to take once more a look at figure 2.7, but concentrate on a different energy range, see figure 4.2. If this is compared with figure 4.1, it is possible to compare the loss times and the change in energy. Figure 4.2 shows the time it takes until the initial proton energy has dropped to $1/e$. The energy $E = 10^{20}$ eV is reached for a time $t_{\text{loss}} \sim 2 \times 10^8$ yr. When this time is read off the x-axis in figure 4.1, one sees that indeed the graphs of $E_{\text{in}} = 10^{21}$ eV and $E_{\text{in}} = 10^{22}$ eV have the value of $E(t) = 10^{20}$ eV at this certain time. Just to emphasize this: An initial energy of more than 10^{20} eV has dropped to $E(t) = 10^{20}$ eV after a time of 2×10^8 yr — this is exactly what was expected to happen from figure 4.2. One should keep in mind that both figures were acquired with totally different approaches, for 4.2 merely the approximation $t_{\text{loss}} = \left(\frac{dE}{dt}\right)^{-1} \times E$ was used, whereas for 4.1 the entire machinery for solving a differential equation was utilized! Of course, the two methods should yield the same results, but the verification of this assumption is advantageous. Since both figures yield the same values, the solution of the differential equation is correct and therefore the implementation was done correctly, too.

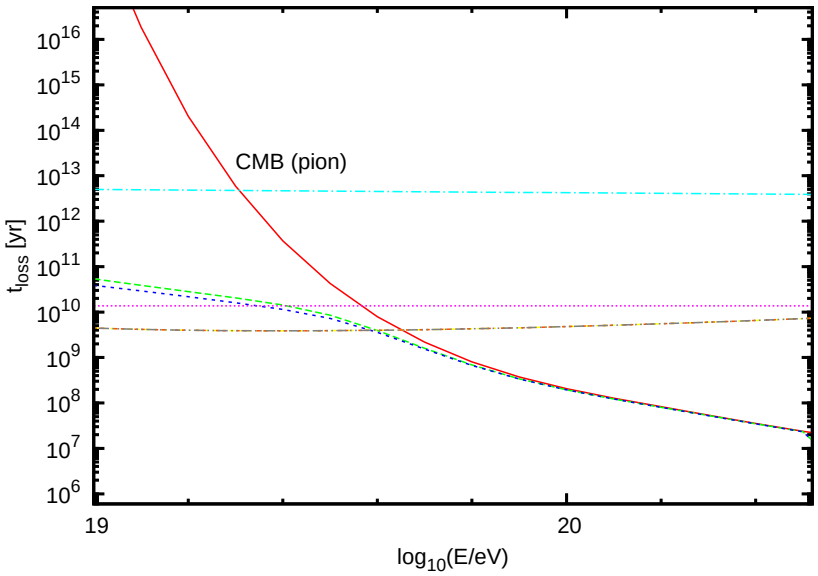

Figure 4.2: This is the same figure as 2.7, only with a different energy range. Here, only the red CMB curve is important, so this is marked. The other colours are the same as in figure 2.7.

Now the different types of energy loss can be fully exploited. Also, the boundaries for equation 2.4 can be calculated.

4.2 Are the EBL photon field and the SCRF important?

The results for $E(t)$ can be used to investigate the importance of the individual photon fields, which were discussed earlier on. It is instructive to look at the energy losses if the UHE protons *only* interact with the radiation fields and the addition of all photon fields separately. Those solutions are displayed in figure 4.3 and show the temporal evolution from a certain starting energy E_{in}. The $E(t)$ curves are similar to the ones that resulted from investigating the pion production mechanism due to CMB photons in figure 4.1.

If both fields, EBL and SCRF, are compared with one another, one can see that the EBL plays a greater role for the production of π-mesons. Protons that interact with EBL photons are more likely to produce π^0 or π^+, because the EBL has a higher spectral energy density. This could be seen in figure 2.6 already for the region of 10 μm and 100 μm. The EBL densities are larger than the cluster field by a factor of 3–4. The interactions with the EBL radiation field occur more frequently and $E(t)$ therefore starts to depart from its initial value E_{in} earlier. This can clearly be seen in figure 4.3, the pink curves start to drop down earlier than the orange ones.

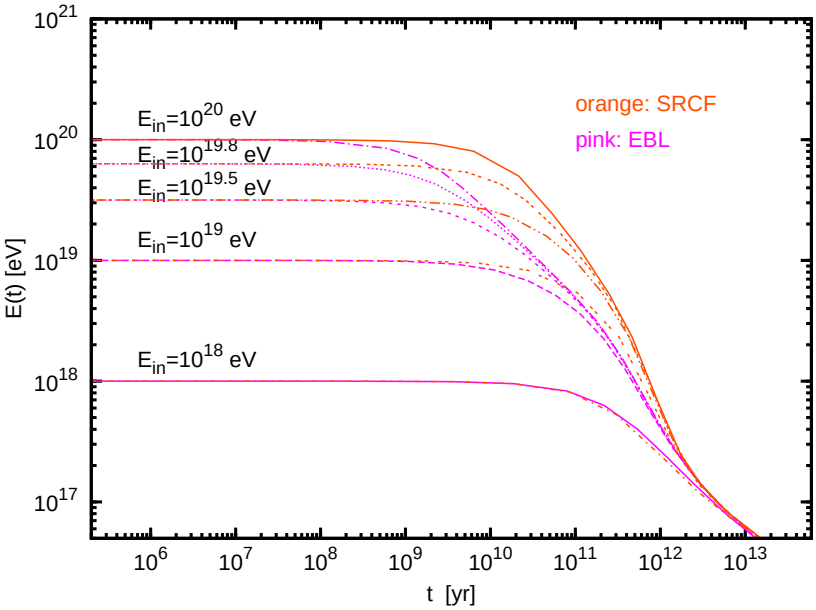

Figure 4.3: The temporal energy loss curves for pion production if the UHE protons interact only with the EBL and the SCRF. The orange curves show the interaction with the SCRF only, the pink ones with EBL only.

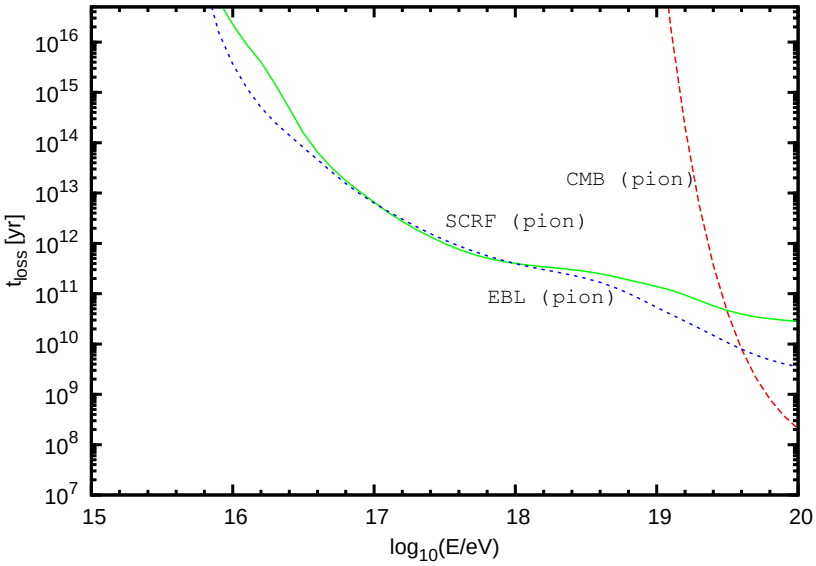

Figure 4.4: t_{loss} for the separate radiation fields of figure 4.3, green is the supercluster field, blue the extragalactic background light. EBL and SCRF act similar, whereas the CMB (red line) dominates in the UHECR regime.

For completeness, also the time scales t_{loss} for the individual interactions of the photon fields are presented here. Whereas figure 2.7 shows the loss time curves for an interaction of SCRF+CMB and SCRF+EBL+CMB, respectively, here the separate radiation field curves are presented. When looking at figure 4.4 one can tell that the influence of both fields changes with the proton energy E. For a proton of $10^{17} - 10^{18}$ eV, t_{loss} is almost the same for the EBL and the SCRF contribution. This corresponds to the region in figure 2.6 where both radiation fields have a similar spectral energy distribution. Below and above this energy range, the EBL dominates the loss processes, yielding shorter t_{loss}. For energies around 10^{20} eV, t_{loss} is shorter by almost an order of magnitude than for lower E.
The dominance of the EBL is visible in the $E(t)$ plot in figure 4.3, too. For the value of $E_{\text{in}} = 10^{18}$ eV, both curves take almost exactly the same course, whereas for $E_{\text{in}} > 10^{18}$ eV the pink EBL curve starts to decline earlier than the orange one. Again, one sees the difference of one order of magnitude that is visible in figure 4.4. If the curve with $E_{\text{in}} = 10^{19.5}$ eV is considered, the time where $E(t)$ departs from its plateau region is approximately $t = 3 \times 10^8$ yr. For the SCRF curve this value is taken to be $t = 2 \times 10^9$ yr, about one order of magnitude higher.
As E_{in} is increased even more, the divergence between EBL and SCRF curves becomes larger, they split at earlier times t. This is clear, because for the very high energies of $10^{19}\text{eV} - 10^{20}$ eV in figure 4.4, the spread between the blue and the green curve has its largest value. For a long time t, all curves nearly fall together as it happened before in figure 4.1 for the CMB interactions. The explanation is therefore the same: The curves for different E_{in} do have an individual course, but they end up at similar values after long interaction times t.
In figure 4.4 is also the CMB interaction curve depicted. One can see clearly the sharp GZK-cutoff, contrary to the photon fields, which act "gradually". Their loss curves show no sharp drop.

Nevertheless, as soon as the CMB interactions are considered, this process dominates over all other contributions. The two figures, 4.5 and 4.6, show the temporal evolution $E(t)$ for the addition of CMB photons and the particular photon fields. The CMB curves are depicted in red, the individual photon fields in orange and pink. The blue dots mark the addition of CMB and EBL or CMB and SCRF, respectively. What is expected is that for $E_{\text{in}} < 10^{19}$ eV, the two other radiation fields dominate the energy losses, but for energies E_{in} larger than a few 10^{19} eV the CMB interaction should be the dominant process. This is exactly what is found in figures 4.5 and 4.6.
Both figures deal with $E_{\text{in}} = 10^{19}, 10^{19.5}, 10^{19.8}$ eV and 10^{20} eV. For the case of $E_{\text{in}} = 10^{19}$ eV it can be seen that the red curve is constant for all energies and the other curves decline. For this certain energy there is no significant interaction with CMB photons, only with photons from the EBL and the SCRF. Therefore the blue dots follow exactly the pink and orange field curves, not the red course for the CMB interaction. The situation is different for higher initial energies E_{in}. If, for example, the curves for $E_{\text{in}} = 10^{20}$ eV are considered, one sees that the resulting blue $E(t)$ dots follow first the course of the CMB interactions. This can be seen as long as

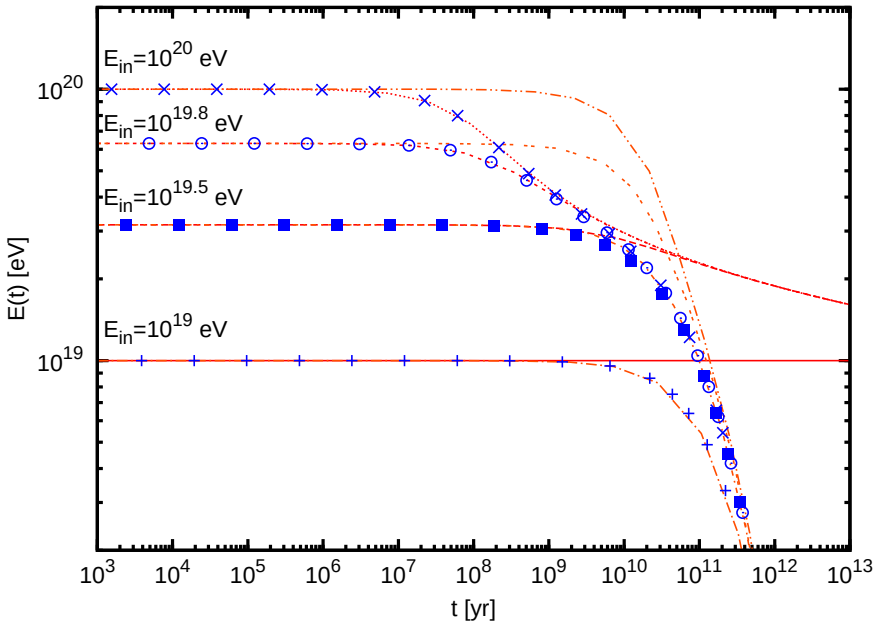

Figure 4.5: The energy losses as they occur when protons collide with CMB photons (red curves) or photons from the SCRF (orange curves).

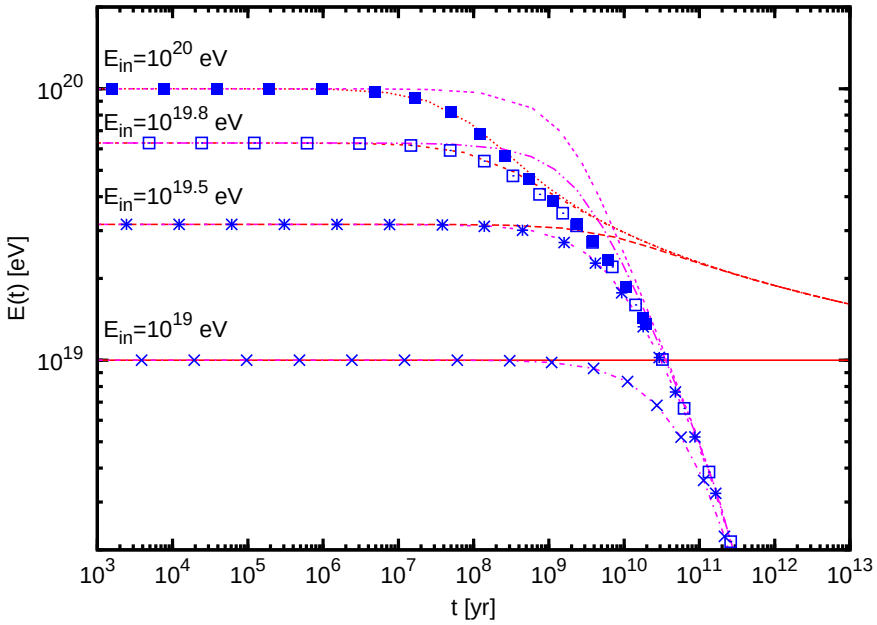

Figure 4.6: The energy losses as they occur when protons collide with CMB photons (red curves) or photons from the EBL (pink curves).

$E(t)$ is high enough to generate the threshold energy for the pion production on CMB photons. As soon as the energy $E(t)$ drops below the GZK threshold energy, the blue dots start to follow the course of the photon fields. This behaviour is seen for the EBL and the SCRF individually in figures 4.5 and 4.6. Like in figure 4.3, it is visible that the EBL dominates. The dots in figure 4.6 start to differ from the CMB lines at $t \sim 10^9$ yr, whereas the dots in the SCRF figure 4.5 start to diverge from the CMB curve at $t \sim 8 \times 10^9$ yr.

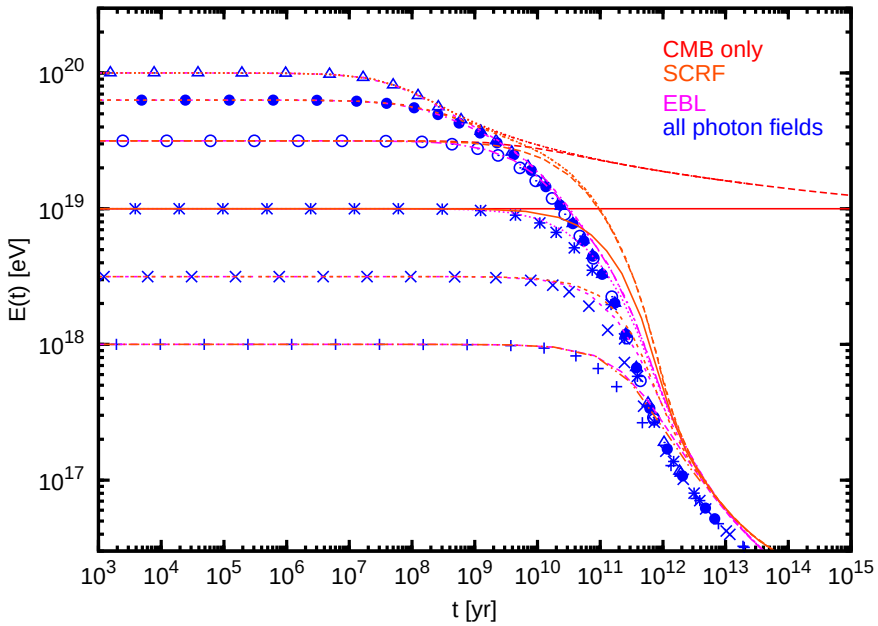

Figure 4.7: The interaction with CMB in contrast to CMB and the other photon fields. The red curves show CMB interaction only, orange CMB+SCRF, pink CMB+EBL and the blue dots describe the addition of all three.

Figure 4.7 presents once more the effects of the individual radiation fields and shows also the contribution of the addition of all radiation fields. The red curves show the energy losses if the protons only interact with CMB photons. The orange and pink curves show in each case the contributions of CMB+EBL (pink) and CMB+SCRF (orange). The blue dots depict the contributions of all radiation fields together, CMB+EBL+SCRF.
As in the previous figures, the blue dots first follow the red CMB curve and begin to follow the pink and orange curves after some time. When $E(t)$ becomes too low for the $p\gamma_{\mathrm{CMB}}$ reaction, the interaction with the EBL and SCRF photons sets in. The co-interaction of the EBL and SCRF radiation field can also be seen in figure 4.7. For the curves with energy $E_{\mathrm{in}} = 10^{18.5}$ eV and $E_{\mathrm{in}} = 10^{18}$ eV, one sees a deviation from the orange and pink field curves. The blue dots (all radiation fields combined) start to drop somewhat earlier at $t \sim 10^{11}$ yr and stay then below the orange and pink curves. The addition of both, EBL and SCRF, increases the losses in the regime of $E = 10^{18}$ eV. $E(t)$ becomes smaller than it would be with the interaction of only

one field alone (CMB+EBL or CMB+SCRF). This behaviour is expected, because for protons of $E(t) \sim 10^{18}$ eV there are more photons available if the two background fields are added, as would be for one field alone.
To wrap up this discussion, one can safely say that the extragalactic background light as well as the supercluster radiation field play an important role in the case of pion photo-production. They are not the prominent process for energies above the GZK-threshold, but are responsible for significant losses below this value. However, the case of pair production has not been considered yet.
As important as the extragalactic background light and supercluster field seem for the pion production process, they are not important when the process of pair production is considered along with the pion production. The main information about the influence of the different radiation fields on pair production can be gained from figure 2.7 already. If only the case of pair production (the grey, yellow and orange lines) is considered, there is a similar picture as for the pure pion production (red, blue and green lines). In figure 2.7 the loss times are shown for the CMB integration only (orange) and for the contributions of CMB+EBL (yellow), CMB+EBL+SCRF (grey), respectively. The curve for the interaction with CMB photons only dominates, there is a sharp decrease in t_{loss} at an energy around $E = 2 \times 10^{17}$ eV. At this proton energy, the centre-of-mass energy of the collision is large enough to produce the electron-positron pair. If the proton energy is lower, the interaction takes place with the EBL or the SCRF photons. But the interaction with CMB photons is clearly the dominant energy loss channel, since t_{loss} for EBL and SCRF interactions lies well below the age of the universe. If one calculated the temporal evolution for pair production, the resulting $E(t)$ curves would look similar to the ones for pion production that have been mentioned above. Therefore this is not presented here. This process does not play a significant role before proton energies of $E = 3 \times 10^{18}$ eV are reached. And at this point, the pair production is completely dominated by interactions with CMB photons. In the case of pair production only the CMB contribution is important.
The overall picture is the following: For energies between $E = 10^{16.5}$ eV and $E = 10^{18}$ eV the losses are dominated by pion production on EBL and SCRF photons, see figure 2.7. In the range between $E = 10^{18}$ eV and $E = 10^{19.6}$ eV electron pair production dominates, but only the interaction with CMB photons. Above the GZK-threshold, the pion production due to CMB photons dominates, as could be seen many times by now. Those are the loss mechanism that were finally implemented in the code in order to determine the spatial proton density $n(E, r, t)$.

4.3 Evaluation of the the integral

In [4], Berezinsky et al. used a single-source model, which goes back to previous calculations of Giler et al.,[11], where the propagation of UHECR within the framework of the supercluster of galaxies was considered.
The model used by Berezinsky et al. is fixed by the choice of source (cosmic ray luminosity L_p, distance r), the parameters that govern the particle propagation ($D(E)$

and $b(E)$), the pulse length P and the injection index γ_g. The values they chose were defined by the properties of the Seyfert I galaxy, NGC 4151 that served as an "example source" for the Virgo galaxy, since its distance from the Earth is close $r = 13.2$ Mpc, albeit not the same as the distance between Virgo cluster and Earth, $r = 17$ Mpc. A cosmic ray luminosity of $L_p = 10^{44}\,\mathrm{erg\,s^{-1}}$ is taken.

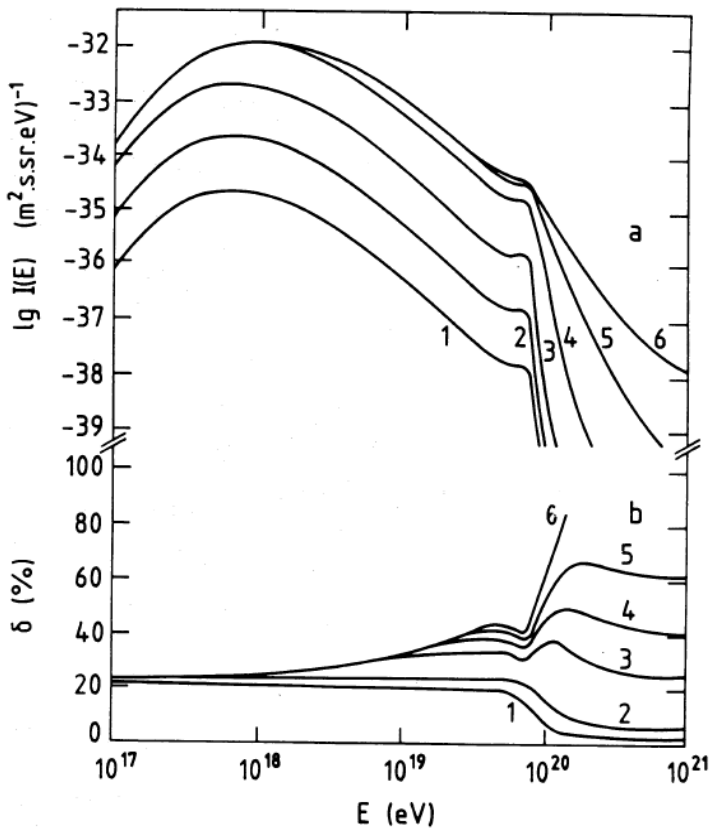

Figure 4.8: Spectrum and anisotropy from the calculations in [4] as a function of the energy E at detection of the protons. The numbers in both panels indicate different source pulses: 1: $P = 10^5$ yr, 2: $P = 10^6$ yr, 3: $P = 10^7$ yr, 4: $P = 10^8$ yr, 5: $P = 2.5 \times 10^8$ yr, 6: $P = 3 \times 10^8$ yr. The corresponding anisotropy is shown in the lower panel.

The density $n(E, r, t)$ is calculated with the given values and compared with the results of [4]. There, Berezinsky et al. consider only the energy losses that are caused by scattering on the blackbody CMB photons.
First, only those interactions with CMB, EBL and the SCRF are implemented that lead to the production of pions. This is depicted in figure 4.9. Only later was pair production added, which is shown in figure 4.10. This lead to surprising results.
The red curves in both figures show the spectra resulting from the CMB interaction,

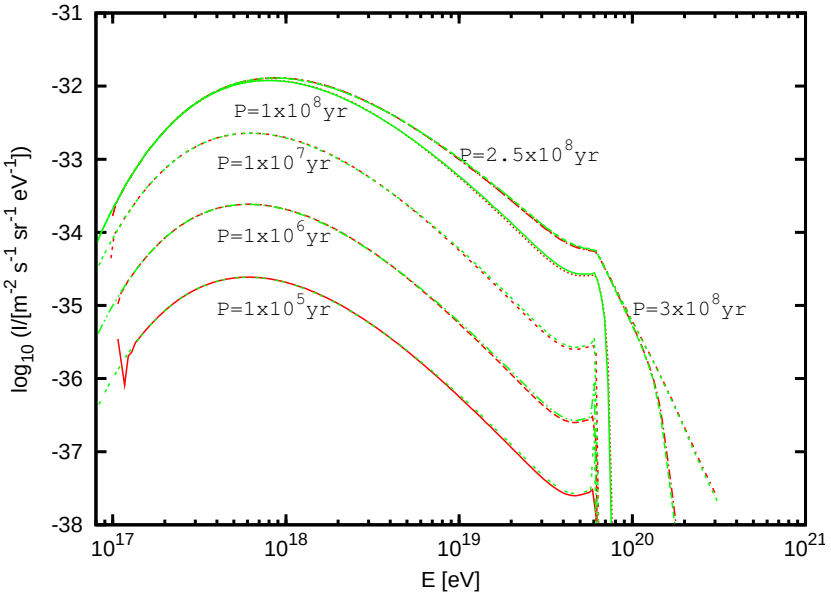

Figure 4.9: The spectra for different source pulses P as a function of the arrival energy E of the protons, as it is shown in 4.8, too. The red curves show the results for the interaction with CMB photons, pion- and pair production. The green curves show the results if only pion production in considered, but with the contribution of all three photon fields.

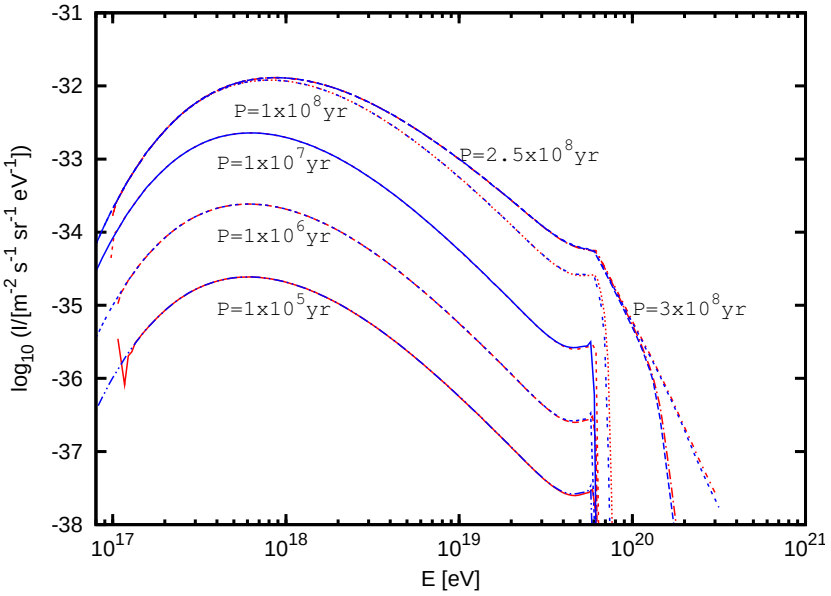

Figure 4.10: The spectra for different source pulses P as a function of the arrival energy E of the protons. The red curves are the same as in figure 4.9. The blue curves show the results of pair production on CMB photons and pion production on all three radiation fields added up.

producing both pions *and* electron-positron pairs. These curves should correspond to the results of Berezinsky et al. in figure 4.8. Figure 4.9 shows beside the CMB interaction also the curve for pion production with all radiation fields combined. This are the green lines and they show an interesting behaviour — they match the red curves! This is not at all obvious, since the two curves describe two different processes. The red curve exhibits pair production, whereas the other curve does not. When figure 2.7 is considered once more, one can see that the loss times for the energy range between $E = 10^{18}$ eV and $E = 10^{19}$ eV are dominated by pair production, whereas in the region below $E = 10^{18}$ eV t_{loss} is dominated by the pion production on the EBL and the SCRF. So one would assume that the differences in t_{loss}, which are several orders of magnitude, show up in the curves for the spectra, too. But this is not the case, the EBL and SCRF in pion production "act" like pair production. The actual differences in t_{loss} play no important role in the integral for the spatial proton density n.
However, this does not influence the final results much, as one can tell from figure 4.10. Here pair production on CMB photons and the pion production on all three radiation fields are taken into account. This curve is displayed in blue. This is the final choice of possible interactions that was used for the rest of this study.
Nevertheless, one can take a closer look at the three different curves, which is done in figure 4.11. It is a zoom in at the peak of three curves from 4.9 and 4.10 at $E \sim 10^{18}$ eV. It shows that the green and blue curve do not match exactly, but that the values are indeed very close to each other. The photon field contributions in green lie just below the pair production curve, whereas the blue and red curves coincide. This means that the contributions of pair and pion production do differ, but the influence is not as big as expected from figure 2.7.

The blue curves in figure 4.10 show on the x-axis the proton energy E after a propagation distance of $r = 13.2$ Mpc. The y-axis shows the corresponding intensity I of the protons.
In [4] Berezinsky et al. consider a propagation time of $t_f = 3 \times 10^8$ yr and different pulse durations P of the source, as indicated at the curves in figure 4.8. The same parameters are chosen for the calculations of this study to be able to compare with those results. The results of both studies match well, as can be seen in figure 4.10. Considering the different pulses P in figure 4.10 and keeping the arrival energy E fixed, one sees that the intensity, rises with the length of the pulse. This is not surprising, because the longer the source "produces" protons, the more are present and can in the end be detected on Earth. If instead of the proton energy E, the pulse period is kept fix, one detects a behaviour that was mentioned in chapter 2 already. Protons with energies slightly above the GZK-threshold interact frequently with the CMB photons, lose much energy and are shifted to lower energies. Therefore the intensity increases as arrival energies $E < E_{GZK} \approx 6 \times 10^{19}$ eV are approached. These protons have then just the right energy to take part in the pair production process and appear at even lower energies. So the intensity rises even more as lower E are considered. The resulting curves peak around 10^{18} eV, which is just the energy at

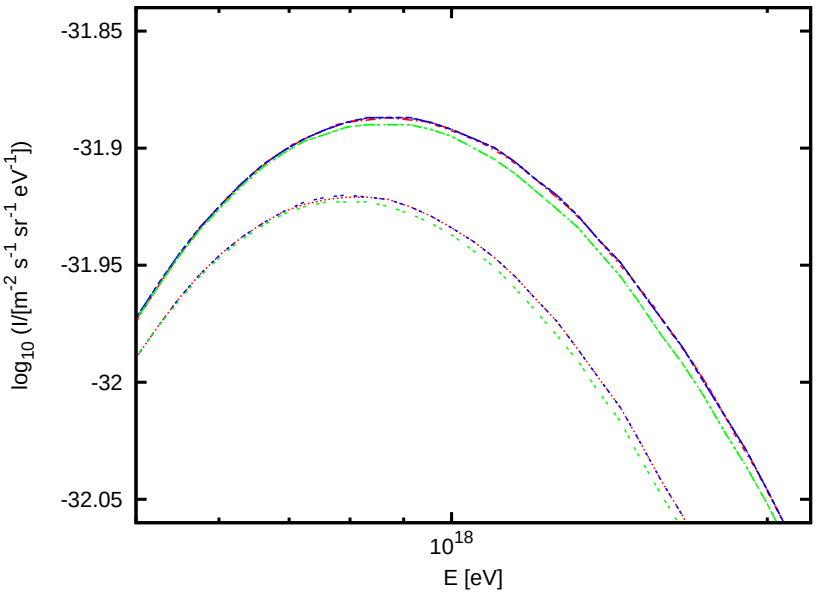

Figure 4.11: Close-up on the $P = 2.5 \times 10^8$ yr and $P = 10^8$ yr curves from the previous figures 4.9 and 4.10.

which the pair production starts to decline, so the protons "pile up" at this energy. The photon fields provide less matching photon, so interactions decline.
The general cutoff at the "high energy" end of the spectrum is caused by the GZK-cutoff. There are hardly protons with $E > 6 \times 10^{19}$ eV detected, because most are shifted to lower energies. The intensity of those high-energy protons is very low. They can only be detected at a significant amount for long pulses, $t_f \sim P$ or for the case of a continuous source. If protons are produced at the very end of a long pulse, it is possible that they just had a few interactions and did not lose much of their initial energy. Those protons can be detected with energies well above the GZK-threshold energy, as can be seen in figure 4.10.
The steepness of the cutoff for short pulses can be explained with the values for the inelasticity and the cross section that are chosen for this study. Since the values of $\frac{dE}{dt}$ depend greatly on σ and K, the spectral curves of Berezinsky et al. and this study do not match entirely. Although the calculations of this study use an inelasticity of $K = 0.3$, which is smaller than the one Berezinsky et al. use, the loss terms $\frac{dE}{dt}$ are larger. This is the result of the larger cross section σ, which ranges up to $\sigma \sim 0.4$ mb. Therefore $\frac{dE}{dt}$ is larger and the intensity decreases, leading to a sharp cutoff of the spectrum for $E \approx 8 \times 10^{19}$ eV.

4.3.1 Intermezzo: Collisions with Interstellar Gas

Possible interactions of the ultra-high energy protons are discussed in section 1.2, where also the interaction with interstellar gas is introduced. In chapter 2 however, the curves for t_{loss} in figure 2.7 show that this interaction is in fact negligible when

the energy regime of $E > 10^{17}$ eV is considered. There, the photon-induced collisions dominate. But it is still interesting, if pp-collisions influence the proton density just below the regime of UHECR. Figure 4.12 displays how these collisions influence the proton spectrum on Earth when $E < 10^{17}$ eV. The blue curves are the extension of the spectrum curves from figure 4.10. Those included the pion and pair production that is caused by the collision of photons and protons. The curves for the pulse $P = 10^7$ yr and $P = 2.5 \times 10^8$ yr are presented. The additional influence of the pp-interactions is shown by the pink dots.

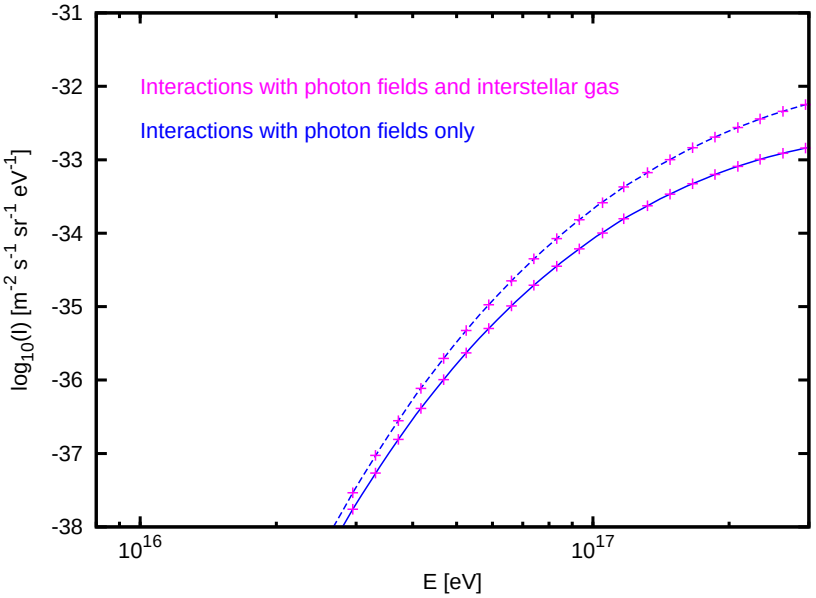

Figure 4.12: The influence of the pp-collision with interstellar gas. The blue curves correspond to the ones in figure 4.10. The pink dots take additionally the pp-interactions into consideration. The two curves present the pulses of $P = 10^7$ yr (lower curve) and $P = 2.5 \times 10^8$ yr (upper curve).

One can tell from 4.12 that there is no significant difference between the lines and the dots, although the t_{loss} curves for the individual processes differ by several orders of magnitude for energies around $E = 10^{16}$ eV, as can be seen in figure 2.7. If the gas density was greater than $n_{\text{gas}} = 2.5 \times 10^6$ cm^{-3}, the influence had to be checked again, but for this chosen value the pp-interactions can indeed be safely neglected.

4.3.2 Adding the B-fields

It was mentioned before that the propagation of UHECR protons is strongly influenced by diffusive processes. The influence of different magnetic fields on the spatial density is to be discussed here. The spectra with the diffusion coefficients from [13] and [4] are compared in figure 4.13 and 4.14. Note that not the intensities, but the actual spatial densities n [m^{-3}eV^{-1}] as they follow the calculations with equation 2.4 are compared.

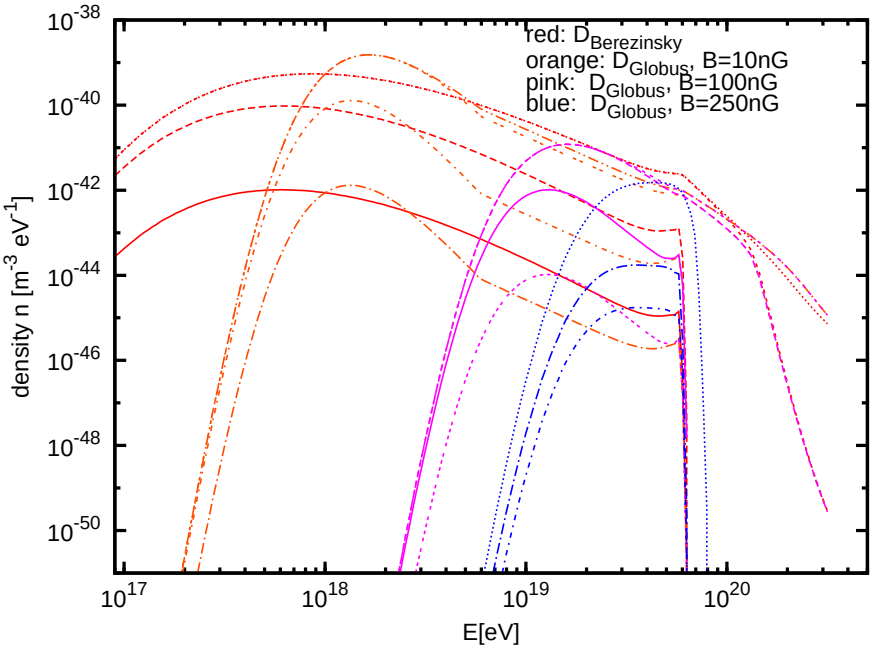

Figure 4.13: The proton density with different $D(E)_{\text{Globus}}$. The curves represent pulses of $P = 10^5, 10^7$, 2.5×10^8 and 3×10^8 yr. The shortest period is the bottom graph and longer P yield higher densities. For the case of $B = 250$ nG only the pulses where $P > 10^6$ yr are shown. For a better comparison, the curves with $D(E)_{\text{Berezinsky}}$ are presented in red, too.

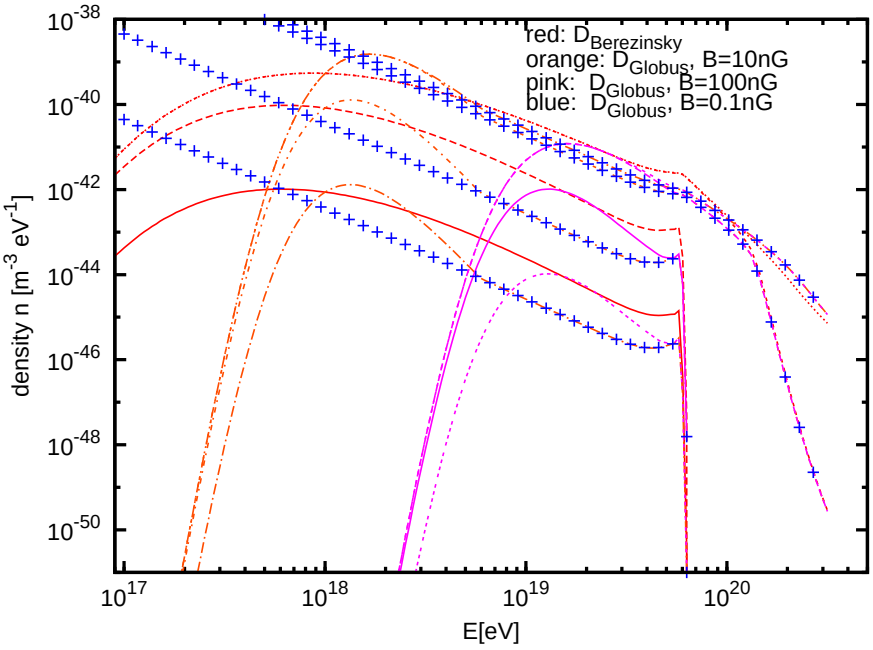

Figure 4.14: The proton density with $D(E)_{\text{Globus}}$, but different magnetic field strengths than in figure 4.13. The four pulses are again $P = 10^5, 10^7, 2.5 \times 10^8$ and 3×10^8 yr.

The results with $D(E)_{\text{Globus}}$ are depicted in orange, pink and blue in figure 4.13. The general behaviour of the curves is the same as in figure 4.10, the number density at a fixed energy E rises with the length of the source pulse P. The longer P, the more protons are emitted and the more are able to reach the Earth. If one examines instead a fixed pulse period and varying E, one sees the same shape as in figure 4.10, too. The density curves rise for the energy range between $E = 10^{20}$ eV and $E = 10^{19}$ eV, peak at a certain energy and start to decline as lower energies are reached. This behaviour has been detected in figure 4.10 before and yields the same explanation.
The curves for a field of ten nanogauss show a dent at the energy of 5×10^{18} eV. This is exactly the point where the limitation for the diffusion coefficient, which was discussed previously in section 3.2.3 sets it. If one compares the energy of the dent in figure 4.13 to the energy in figure 3.1, where the diffusion coefficient reaches the value of D_{max}, one sees that they match. But this does not influence the overall course of the orange $B = 10$ nG curves. They peak at approximately 10^{18} eV, because they undergo effective loss processes for $E > 10^{18}$ eV and slide to energies of $E \approx 10^{18}$ eV. Below this energy they can only interact with the EBL or the SCRF. As before, this does not happen very often, so the protons are "piled up" at $E \approx 10^{18}$ eV. As the magnetic field strength is increased, the overall position of the curves changes. The densities become lower and the curves move towards higher energies. This can be explained by stronger diffusion: UHE protons are kept closer to their source as the magnetic field grows. Only protons released with a sufficient energy can overcome the magnetic fields and propagate the distance of 13.2 Mpc to Earth. These protons are consequently detected with a higher energy, so the curves are shifted to higher values of E. For $B = 100$ nG, the density peaks at $E = 10^{19}$ eV, just below the GZK-threshold.

The peak moves to even higher values of E, as the magnetic field strength reaches a value of $B = 250$ nG, which is shown in blue in figure 4.13. Moreover, the features of the curves for $B > 10$ nG vanish, they "shrink" and make a thorough discussion of those curves impossible.
So figure 4.13 sets an upper limit to the magnetic field strength, 100 nG. This value is used for the rest of this study. But what happens if fields lower than 10 nG are present?
This can be seen in figure 4.14, where the blue dots indicate a field strength of $B = 0.1$ nG. It seems as if those curves would not peak at all, but actually they do, but below $E = 10^{17}$ eV. It is interesting to note that they converge with the 10 nG curves, after D_{max} sets in. For a field of 0.1 nG, the limitation of $D(E)$ set is at lower energies already so at a certain point they have to converge with other D_{max} curves.
A field of $B = 10$ nG is taken as the lower bound for the fields strengths. The choice of magnetic field strengths is reasonable within the supercluster, as was discussed in section 1.2 already.
The curves that result from the final choice of field strengths are presented in figure 4.15 once more. If the continuous source case of $P = 3 \times 10^8$ yr is considered it is

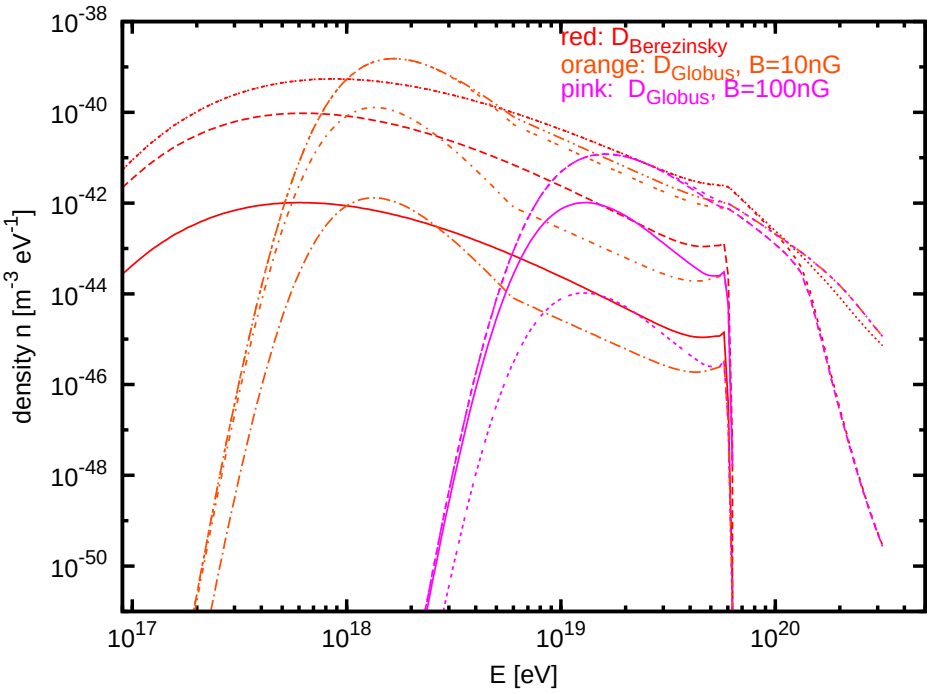

Figure 4.15: The final choice of magnetic fields that are studied in this thesis. The pulses are the same as in the two previous plots: $P = 10^5, 10^7, 2.5 \times 10^8$ and 3×10^8 yr. The distance to the source is $R = 13.2$ Mpc.

visible that the curves for $B = 10$ nG and $B = 100$ nG fall together above an energy of $E = 6 \times 10^{19}$ eV. This is the energy at which the limitation of the diffusion coefficient sets in for $B = 100$ nG, so consequently the curves have to meet. One should keep this feature in mind, section 4.6 will go back to this.

4.3.3 Anisotropy

Looking back to the lower panel of figure 4.8 one can gain information about the anisotropy of the protons from NGC 4151. The curves show low anisotropy values for short source pulses and increasing values as the pulses become longer. But this describes only the general sketch of the anisotropy curves. All curves in the lower panel of figure 4.8 show a dent just before $E = 10^{20}$ eV. This is the same energy, at which a bump occurs in the intensity in the upper panel. A sudden change in n refers to a change in $\frac{\partial n}{\partial r}$, so the anisotropy changes abruptly below $E = 10^{20}$ eV. The numbers at the anisotropy curves in figure 4.8 indicate the different pulse lengths of the source. For the shortest pulse one sees a decline of the anisotropy after 10^{20} eV, the value falls from 20% below 10%. For all longer pulses the course of the anisotropy curves is different. Values lie in the range of 20% up to 70 %, but decrease at the high-energy end of the curves. The only exception is the curve for the continuous source, $t_f = P$. The anisotropy keeps rising over the entire proton energy range. What causes this behaviour?

For short pulses the anisotropy is almost constant at low values over the entire energy range. This means that there is no strong correlation between the direction the protons are detected from and the direction of NGC 4151. This can be explained when the distance the protons have to cover during their propagation is taken into account. When the protons from a short pulse arrive on Earth, there are hardly any protons with energies above $E = 10^{20}$ eV left. Moreover, they had a lot of time to diffuse. So the detected number of those protons is simply to low to establish any correlation. Therefore the anisotropy decreases just before $E \approx 10^{20}$ eV. For the mentioned longer pulses this changes.
The longer the source pulse, the later can protons be produced, the more protons with high energies arrive on Earth. Those anisotropy curves do not show a sharp cutoff for high detection energies, but a smooth or no decline. For a continuous source there are even extremely energetic particles with $E > 10^{20}$ eV arriving all the time, so the anisotropy for this can reach up to 100%. This is the reason for the constant rise of the uppermost anisotropy curve in figure 4.8.

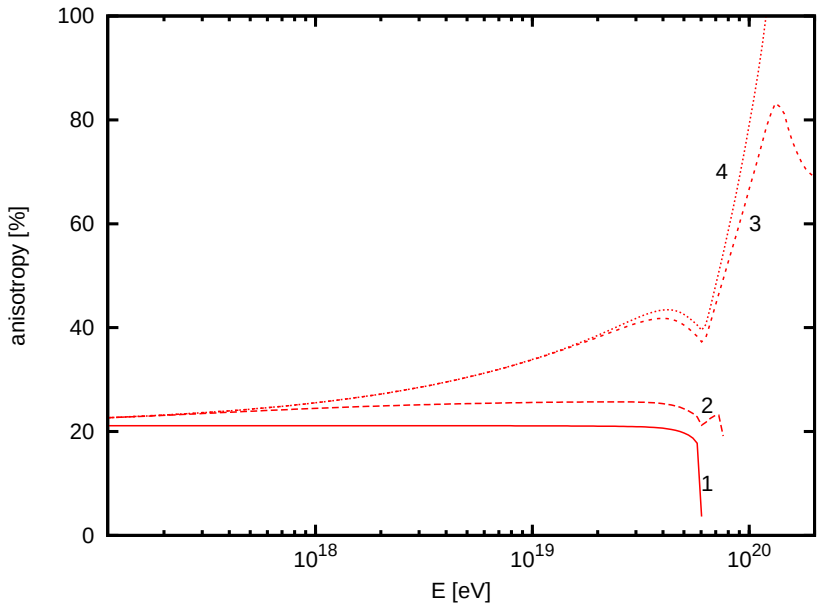

Figure 4.16: Anisotropy for the spectral curves with $D(E)_{\text{Berezinsky}}$ in figure 4.10. The numbers on the curves indicate different pulse lengths, 1: $P = 10^5$ yr, 2: $P = 10^8$ yr, 3: $P = 2.5 \times 10^8$ yr and 4: $P = 3 \times 10^8$ yr and correspond to 1, 3, 5 and 6 in figure 4.8.

When the anisotropy results of this study are compared with the Berezinsky plot, one can document a similar behaviour for the calculations. This is expected, because also the spectral curves matched well. Figure 4.16 presents the anisotropy as it is calculated with equation 2.8 for the case of $D(E)_{\text{Berezinsky}}$. The displayed curves in figure 4.16 indicate source pulses of $1 : P = 10^5$ yr, $2 : P = 10^7$ yr, $3 : P = 2.5 \times 10^8$ yr and $4 : P = 3 \times 10^8$ yr length. One can see that the curve labeled 1 for the shortest pulse

$P = 10^5$ yr matches well the results from Berezinsky et al. The curve is constant over the entire energy range and declines at $E \sim 6 \times 10^{19}$ eV, when the GZK-cutoff sets in. The anisotropy lies just above 20% before the fall. The two longest pulse curves, labeled 3 and 4, show a similar behaviour as the Berezinsky results, too. There is however a difference in the curve for $P = 2.5 \times 10^8$ yr. The curve for the calculation of this study show a sharp decrease for energies larger than $E = 10^{20}$ eV, whereas the curve in figure 4.8 exhibits a smooth decline. This is caused by the choice of σ and K for $\frac{dE}{dt}$. The energy losses in this study are more prominent for $E > 10^{20}$eV, the density decreases abruptly and the anisotropy curve drop sharply. For the case of a continuous proton source both studies yield the same results, the anisotropy curve for $P = 3 \times 10^8$ yr rises continuously.

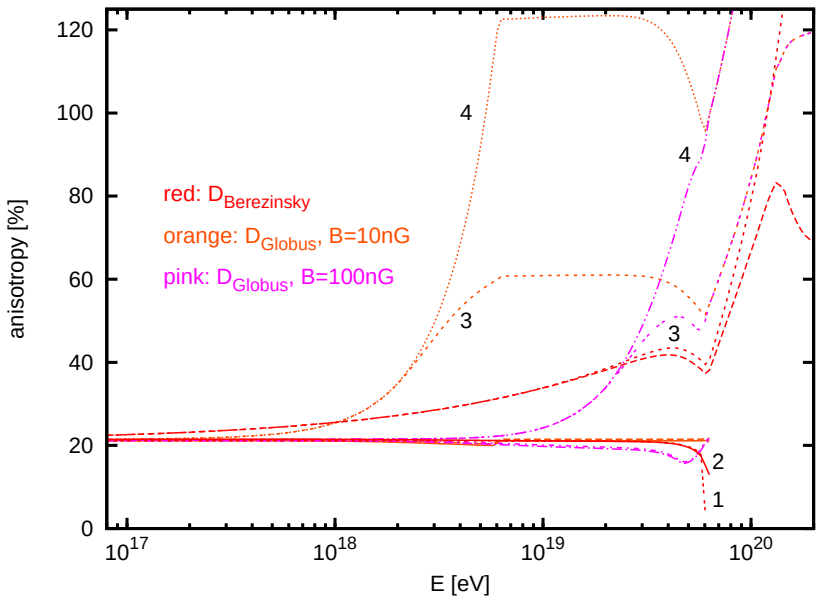

Figure 4.17: The anisotropy as it is calculated with equation 2.8, for several pulses and $D(E)_{\text{Globus}}$. The values, 1: $P = 10^5$ yr, 2: $P = 10^7$ yr, 3: $P = 2.5 \times 10^8$ yr and $4 : P = 3 \times 10^8$ yr are the same as in figure 4.15 where the corresponding proton density is shown. The curves with $D(E)_{\text{Berezinsky}}$ are shown for comparison.

The anisotropy results for $D(E)_{\text{Globus}}$ are presented in figure 4.17. The red curves are the same as in figure 4.16 and are displayed to compare the other curves with. As for the density plot, the pulses of $1 : P = 10^5$ yr, $2 : P = 10^7$ yr, $3 : P = 2.5 \times 10^8$ yr and $4 : P = 3 \times 10^8$ yr are considered.
The two shortest curves with $D(E)_{\text{Globus}}$ show a similar behaviour than the red ones. They have an anisotropy of roughly 20% throughout the entire energy range. The curves seem to stop at a certain point, but this is caused by the abrupt decline in proton density that comes out of the calculation. The spectral curves in figure 4.16 tend to decline steeply, because of the chosen values for K and σ and this behaviour appears also in the anisotropy plots. For an energy of $E \sim 10^{20}$ eV, the successive data points yield an anisotropy of almost zero. If those values would be depicted, the

decrease of all curves with short pulses would fall together and one could not distinguish between the individual pulse lengths. So the data points where the anisotropy is close to zero are, for the sake of a better comprehensibility, not shown in figure 4.17.
In general, the anisotropy curves with $D(E)_{\text{Globus}}$ show a similar behaviour than the ones with $D(E)_{\text{Berezinsky}}$, but there are some differences. These show up when the curves are studied in detail. The two curves with the shortest pulses match, no matter what the actual B-field is. All are almost constant and yield anisotropy values around 20%. A general feature of all curves is that the anisotropy rises as the pulses become longer. This is where differences between the diffusion coefficients emerge. The difference in $D(E)$ shows the influence of different magnetic field strengths. One can see from the different colours that the anisotropy starts to rise at different energies. For the case of $D(E)_{\text{Berezinsky}}$, this rise sets in at $E \sim 10^{18}$ eV, for $B = 10$ nG at slightly lower energies and for $B = 100$ nG at $E \sim 10^{19}$ eV. The anisotropy rises later for larger field strengths. This is, because the stronger the magnetic field around the source, the closer the protons are kept in this region. When a field of 100 nG is present, protons must have larger energies to overcome this as they would have if a magnetic field of only 10 nG was present. So this explains the rise in anisotropy for larger energies for the 100 nG field. In return, the rise sets in at lower energies for a smaller field. Since Berezinsky et al. assume a field of $B = 2 \times 10^{-8}$ G, it is clear that the red curves lie between orange and pink ones.
When the orange curves are studied, the limitation of the diffusion coefficient can be seen again. This is visible in the "plateau" region between $E = 7 \times 10^{18}$ eV and $E = 3 \times 10^{19}$ eV. Another feature of these curves are anisotropies above 100%. These values are actually unphysical, but nevertheless they describe a general idea.
The smallest magnetic field that is considered in this study is $B = 10$ nG. This is not big enough to diffuse protons throughout the entire supercluster. Some protons have an energy that is large enough to overcome the diffusion and propagate straight to Earth. Thus, a relation between the source direction and the direction from which the protons are detected is established. The anisotropy rises to large values. For the other magnetic field strengths such high anisotropies arise only for the case of a continuous source. A continuous source emits protons with very high energies also at the end of the propagation time. These protons do not lose much of their initial energy and when they are detected it is evident that they originated from the source. This explains the high anisotropy values.
The results of figure 4.15 can also be used for determining the magnetic field strength in the cluster. The Auger experiment has measured an anisotropy of $\sim 30\%$ for energies above $E > 10^{19}$ eV, see [25]. If this number is taken as a constraint, the field strength that has to be present in the supercluster can be determined with the calculated curves. The curves rule out a field of $B = 10$ nG, $B = 100$ nG will fit the measurements. The case of a continuous source is ruled out as well, since this yields anisotropies that are larger than 30%.

4.4 A longer propagation time

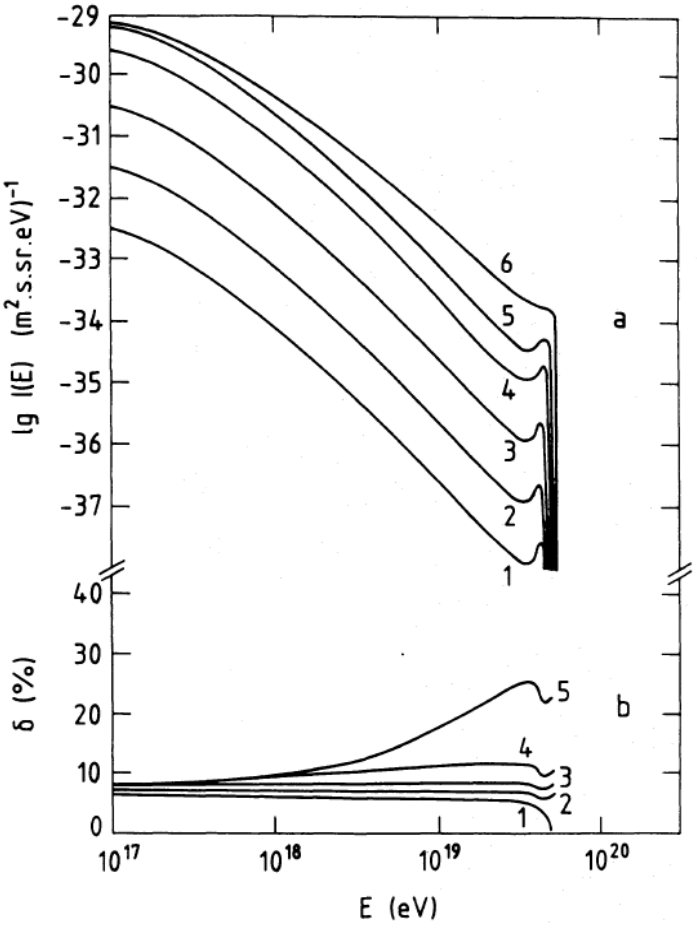

Figure 4.18: Spectrum and anisotropy from the Berezinsky calculations with a longer propagation time $t_f = 10^9$ yr. The spectra curves represent the following pulses: 1: $P = 10^5$ yr, 2: $P = 10^6$ yr, 3: $P = 10^7$ yr, 4: $P = 10^8$ yr, 5: $P = 3 \times 10^8$ yr and 6: $P = 10^9$ yr. The corresponding anisotropies are displayed as well. These are calculated for 1: $P \leq 10^7$ yr, 2: $P = 3 \times 10^8$ yr, 3: $P = 5 \times 10^8$ yr, 4: $P = 8 \times 10^8$ yr and 5: $P = 10^9$ yr. The figure is taken from [5] where $R = 13.2$ Mpc.

The calculations that are done so far give some insight in how the density distribution of UHE protons changes, if different source pulses, diffusion coefficients and B-field strengths are taken into consideration. The propagation time in all cases was $t_f = 3 \times 10^8$ yr. This number was chosen to be able to compare the results from this study with the results from [4]. In their paper [5], Berezinsky et al. calculate the spectrum and anisotropy also for a prolonged propagation time of $t_f = 10^9$ yr. The results are presented in figure 4.18 taken from their paper.
The overall shape of the curves is still the same, but some features have changed. One

can see that the maximal density moves from $E = 10^{18}$ eV to $E = 10^{17}$ eV. Besides, the cutoff energy of the curves is lower than before. In figure 4.8 it was just below $E = 10^{20}$ eV, now it can be found at $E \sim 5 \times 10^{19}$ eV. This is caused by the change of propagation time. A longer t_f moves the cutoff to lower energies, because the protons have more time to lose energy and thus the entire spectrum is moved "downwards" in energy. The cutoff itself is now more pronounced, all curves fall off very steeply and come down to very similar values. The results from the calculations of this study are presented in figure 4.19.

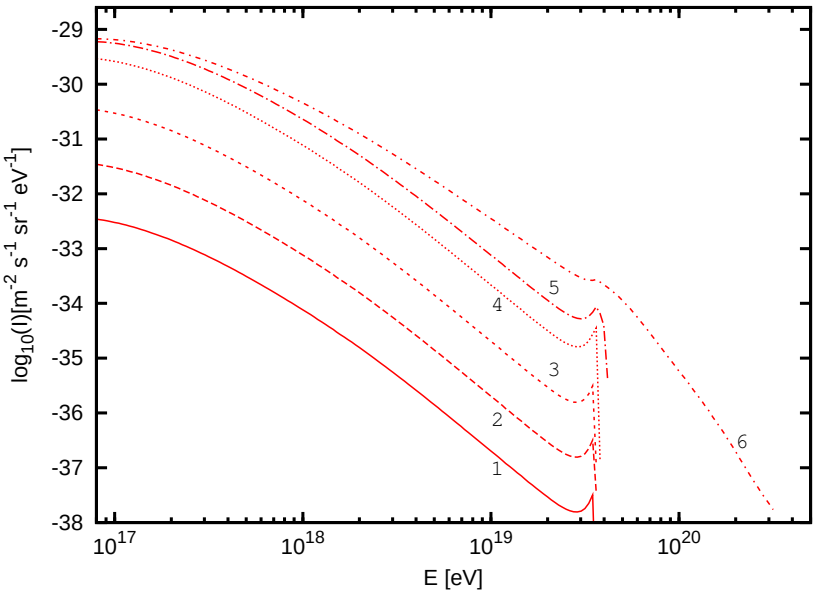

Figure 4.19: The calculated spectra for a propagation time of $t_f = 10^9$ yr and $D(E)_{\text{Berezinsky}}$. The curves indicate source pulses of 1: $P = 10^5$ yr, 2: $P = 10^6$ yr, 3: $P = 10^7$ yr, 4: $P = 3 \times 10^8$ yr and 5: $P = 10^9$ yr. The curves should match the results from [5] in figure 4.18.

The general comparison between the two figures shows that the results match for most pulses. The general shift of the maxima, which is seen in figure 4.19 as well, comes from the fact that the protons propagate longer. A significant difference can be seen for the longest pulse $P = 10^9$ yr. Whereas in figure 4.18, all curves decline sharply before $E = 10^{20}$ eV, the longest pulse in 4.19 does not. The reason for this is probably the source output that is allowed. The maximal energy with which a proton can be ejected from its source is set to $E_{\text{max}} = 1.22 \times 10^{28}$ eV. This is a very large number, but is used to see how the assumptions of this model behave under such extreme conditions. Moreover, the choice of maximal energy did not influence the calculations for the shorter propagation time of $P = 3 \times 10^8$ yr, figures 4.10 and 4.8 match very well. If the maximal proton energy at generation was set to a lower value, the curves in figure 4.19 would decline for $E < 10^{20}$ eV. But so there are protons present that are detected with $E > 10^{20}$ eV, even after a propagation time of 10^9 yr.
For the curves labeled 1–5 only those data points are plotted that have an intensity

that is not close to zero. Otherwise the curves would fall together and one could not investigate their behaviour properly. In general it can be pointed out that the intensity rises for the prolonged propagation time of $t_f = 10^9$ yr compared to $t_f = 3 \times 10^8$ yr. If the propagation time is prolonged, more protons are able to propagate to Earth and yield a rise in intensity and proton density, respectively. The rise can be seen especially well for energies of $10^{17} - 10^{18}$ eV. The protons that were detected with $E > 10^{18}$ eV for $t_f = 3 \times 10^8$ yr, move to lower E for a longer propagation time. Besides, the general feature can be seen that longer pulses yield higher intensities. The longer propagation time t_f is reasonable, because it allows to take early source in the universe into account as well.
Next it is to be investigated how the curves look if $D(E)_{\text{Globus}}$ is used. Those results can be found in figure 4.20:

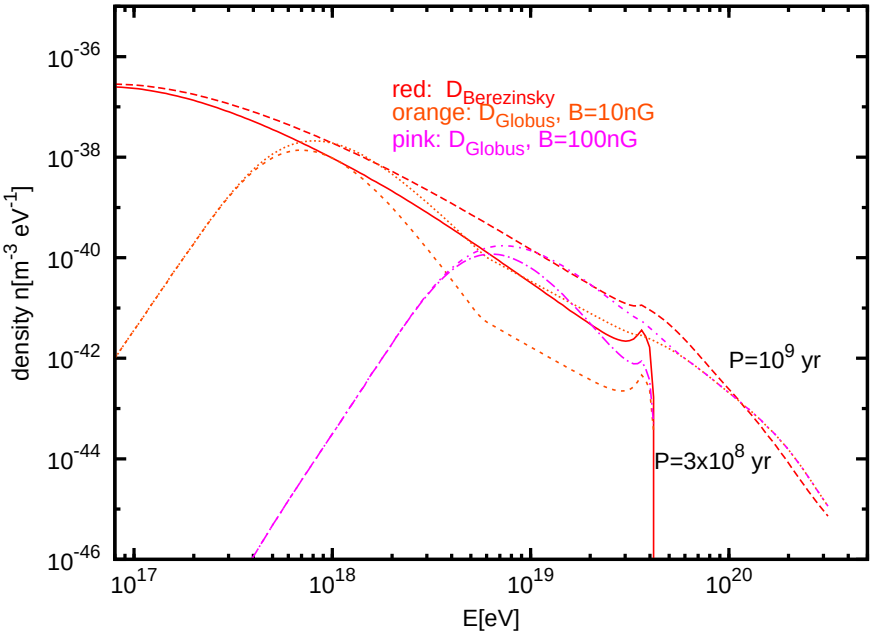

Figure 4.20: This figure presents the proton density for a prolonged propagation time. Here the the influence of $D(E)_{\text{Globus}}$ (pink and orange curves) can be seen in contrast to the red curves for $D(E)_{\text{Berezinsky}}$. Only two pulses are shown, $P = 3 \times 10^8$ yr and $P = 10^9$ yr.

To make this figure less crowded, only two pulse lengths, $P = 3{\times}10^8$ yr and $P = 10^9$ yr are considered. The red curves are the same as in figure 4.18 with the Berezinsky diffusion coefficient. From first sight, one can tell that all curves with the shorter pulse decline before 10^{20} eV and show a similar course as could be seen for the shorter propagation time $t_f = 3 \times 10^8$ yr in figure 4.15. All decline at the same energy $E \sim 4 \times 10^{19}$ eV. The curves with $D(E)_{\text{Globus}}$ have the density maxima at higher energies than the ones with $D(E)_{\text{Berezinsky}}$. This is consistent with earlier results of $t_f = 3 \times 10^8$ yr. Interesting to note is that the energy at which the density maxima for $D(E)_{\text{Globus}}$ occur, has not changed. The $B = 10$ nG curves peak at $E \sim 10^{18}$ eV,

the $B = 100$ nG curves at $E \sim 10^{19}$ eV in both figures, 4.15 and 4.20. This is in disagreement with the $D(E)_{\text{Berezinsky}}$ curves, where a shift of the maxima is seen. The actual density values are roughly the same as before, too. A possible explanation is the high energy at generation. Although the protons are able to propagate longer, there are enough protons that arrive with at energy of $E = 10^{18}$ eV and $E = 10^{19}$ eV, respectively. The limitation for $D(E)$ can be seen again for an energy $E > 5 \times 10^{18}$ eV. for $B = 10$ nG.
As before in figure 4.15, the curves for a magnetic field of strength $B = 10$ nG yield higher density values than the curves for $B = 100$ nG. This is because protons need less energy to overcome a magnetic field with a smaller value. If a magnetic field with $B = 10$ nG is present, there are more protons available that have the right amount of energy to overcome this certain field and propagate to Earth.

4.4.1 Anisotropy

The anisotropies that arise for $t_f = 10^9$ yr and $D(E)_{\text{Berezinsky}}$ are presented in figure 4.21.
The curves presented should be in agreement with the curves from the lower panel in figure 4.18. To a great extent they match very well. The exact comparison can be done between the individual curves 1, 2, 5 of figure 4.18 and curves, 2, 3, 5 of figure 4.21, since those describe the exact same pulse lengths. But the most important features in anisotropy can be examined even if the pulses have only similar length. The first thing one can tell from figures 4.18 and 4.21 is that the anisotropy has declined for all pulses. This is, because the protons propagate and diffuse longer and arrive therefore from all directions and yield a smaller anisotropy than before. For the short pulses the same behaviour as in figure 4.8 can be seen: Their anisotropy is constant throughout the entire energy range, but with an anisotropy of roughly 6%, instead of 20%.
For the curves with longer pulses, e.g. number 4 where $P = 8 \times 10^8$ yr, one can see that the anisotropy rises to higher values than in figure 4.8 for $E > 10^{18}$ eV. Protons in 4.21 are able to diffuse more and lose more energy in interactions, consequently the anisotropy rises for larger E, since only high-energy protons have enough energy to resist the diffusion.
In 4.21 it can also be seen that dip of the anisotropy curves moves down in energy. This happens, because the cutoff energy of the intensity curves is shifted too, as can be seen in 4.19. The change in n at $E \sim 4 \times 10^{19}$ eV correspond to the change in $\frac{\partial n}{\partial r}$ for the anisotropies.
For the energies above the dip the curve progression cannot be compared properly between figures 4.18 and 4.21, since the curves in 4.18 stop at $E \sim 5 \times 10^{19}$ eV. In their paper [5], Berezinsky et al. do not give any explanation for this. The results of this thesis however show a steady rise in anisotropy, see curves 4 and 5 in figure 4.21. This feature arise only for the longest pulses $P \simeq t_f$, when protons are constantly ejected. Those lose only a small part of their initial energy as they propagate to Earth. While those high-energy protons appear seldom for short pulses, they come more in more

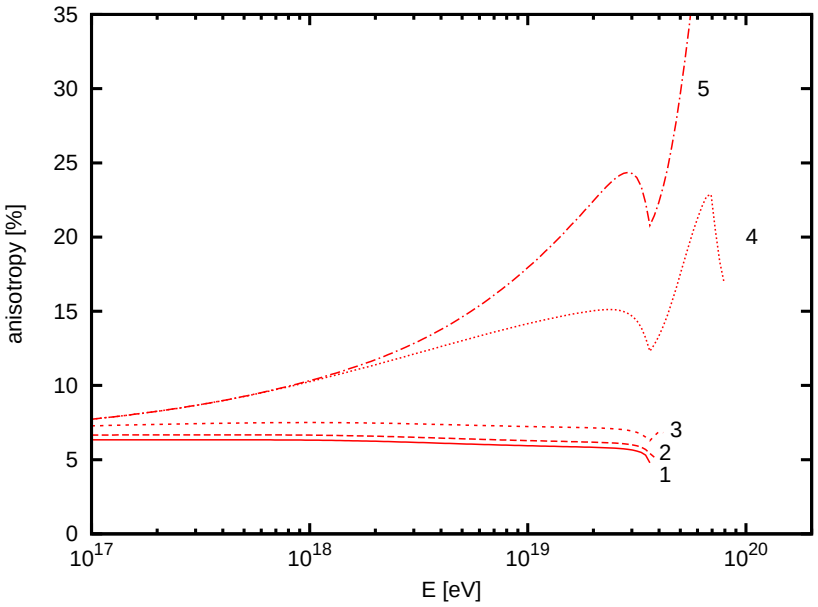

Figure 4.21: This plots shows the corresponding anisotropies to figure 4.19 with $D(E)_{\text{Berezinsky}}$. The numbers on the curves correspond pulses of 1: $P = 10^6$ yr, 2: $P = 10^8$ yr, 3: $P = 3 \times 10^8$ yr, 4: $P = 8 \times 10^8$ yr and 5: 1: $P = 10^9$ yr. These anisotropies can be compared with the lower panel in figure 4.18. where the propagation time is $t_f = 10^9$ eV.

abundantly for the continuous source case, the anisotropy rises.

Figure 4.22 shows the anisotropies when the diffusion coefficient $D(E)_{\text{Globus}}$ is applied along with a prolonged propagation time. When comparing the anisotropy curves in figure 4.22 one can draw the same conclusions as for the shorter propagation time. There is hardly any difference between the Globus and the Berezinsky diffusion coefficient for the shortest pulses. All those curves show a constant anisotropy of less than 10% and have a little dip before they decline at $E \sim 4 \times 10^{19}$ eV. This energy is lower than before, because the cutoff of the spectrum is shifted, too.

All anisotropy curves with a medium pulse lengths, $P = 8 \times 10^8$ yr, in figure 4.22 start with an anisotropy of roughly 10% and rise as higher E are approached.

The curves describing the continuous source scenario exhibit very large anisotropies for high E, since high-energy protons are constantly ejected.

As before in figure 4.17, the $B = 10$ nG curve rises quickly and yields anisotropy values which are very close to 100%. The information this gives is the same as before: If a magnetic field of $B = 10$ nG is present, there are many protons that can overcome this are able to propagate directly to Earth. Those protons must be produced in the end of the propagation pulse, otherwise they would not have enough energy to overcome the magnetic field. If they are detected, a strong correlation between the direction of the source and the protons can be established. For the case of a stronger magnetic field of $B = 100$ nG, as it is depicted in pink, the anisotropy is lower. This field strength would require even more energetic protons to overcome the field. Those

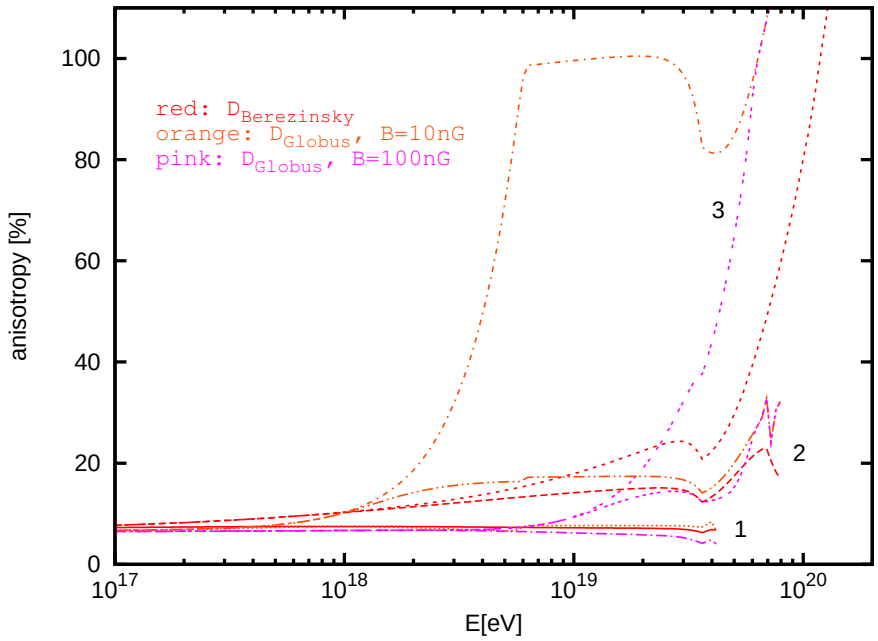

Figure 4.22: This figure presents the corresponding anisotropies to figure 4.20. The numbers denote pulses of 1: $P = 3 \times 10^8$ yr, 2: $P = 8 \times 10^8$ yr and 3: $P = 10^9$ yr. The also show the difference between the two diffusion coefficients. The propagation distance is still $R = 13.2$ Mpc.

do not occur that often, therefore their anisotropy is smaller.
In terms of magnetic field predictions according to Auger measurements it can only be pointed out that the continuous source case is ruled out by the calculated curves. The anisotropy of those curves is too high. Contrary, all other pulse lengths yield anisotropies that are too small. The choice of diffusion coefficient does not influence those results.

4.5 Varying the distance to the source

The results so far were all presented as a function of energy E at detection of the protons, but $n(E, t, r)$ also has a time and distance dependence, the latter one is considered now. The aim of this thesis is to gain knowledge on the proton distribution within the supercluster, so it is interesting to know how the density changes as one proceeds from the centre to the outer rim of the LSC. In this section the plots show the proton density with respect to the distance r from the source. The energy at detection is fixed. The parameters, such as cosmic ray luminosity L_p and spectral index of the source γ_g are still as they have been described in the first paragraph of this chapter, $\gamma_g = 2.1$ and $L_p = 10^{44}\,\mathrm{erg\,s^{-1}}$. The "test source" is still NGC 4151. The interest lies in the overall shape and behaviour of the curves, so it is reasonable to do calculations with NGC 4151 first.

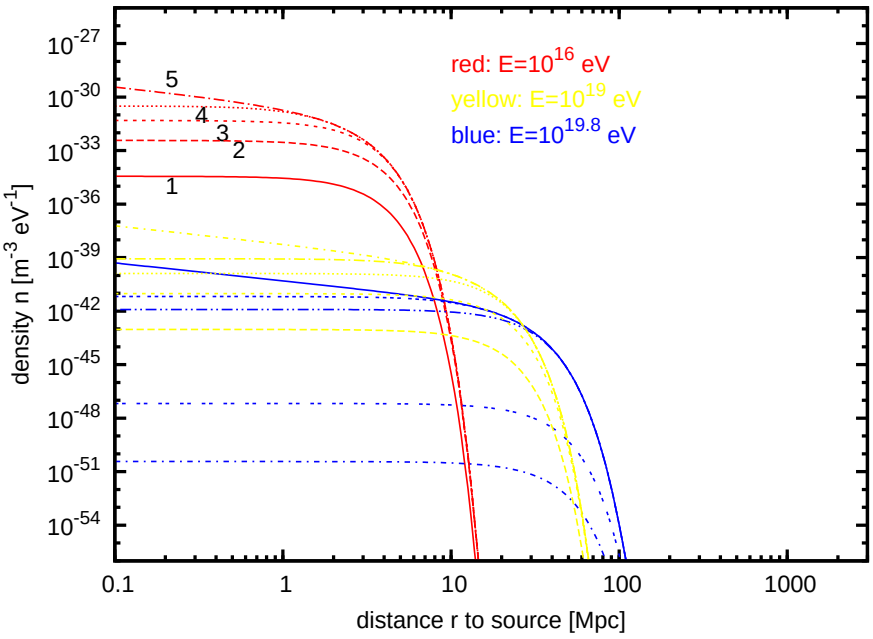

Figure 4.23: The spatial density $n(E, r, t)$ for different energies E and different pulses P. The curves show 1: $P = 10^5$ yr, 2: $P = 10^6$ yr, 3: $P = 10^7$ yr, 4: $P = 10^8$yr, 5: $P = 3 \times 10^8$ yr, as before in figure 4.10. The energies at detection E are $E = 10^{16}$ eV (red), $E = 10^{19}$ eV (yellow) and $E = 10^{19.8}$ eV (blue).

Figure 4.23 displays three different energies at arrival: $E = 10^{16}$ eV (red), $E = 10^{19}$ eV (yellow) and $E = 10^{19.8}$ eV (blue). To discuss the curves in this chapter thoroughly, it is necessary to start with the"default values", $D(E)_{\text{Berezinsky}}$ and a propagation time of $t_f = 3 \times 10^8$ yr. Figure 4.23 yields the results for this certain choice of parameters. Five different pulses are shown.
One should note that the curves for the different energies at detection have the same course, although the interactions that lead to this energy differ. Whereas for high E the interactions with CMB photons dominate, the EBL and SCRF play a role for $E < 10^{18}$ eV. The curves for the individual pulses P of a certain E differ from one another in terms of proton density. The longer the pulse, the higher the measured density, no matter if the protons arrive at one or ten megaparsec distance. A longer pulse P implies naturally a larger density, because the longer a source is active, the more protons are emitted. What can be seen, exemplary in the red curves for $E = 10^{16}$ eV, is that the density slowly declines over some distance and starts to drop rapidly at one point. The curves look constant, but this is caused by the logarithmic scale. For example, the density of the yellow curves has dropped about 2–3 orders of magnitude at $R \approx 20$ Mpc in contrast the very centre of the supercluster.
The same behaviour is found for a higher E, but there the densities start to decline at larger distances r. As the energy E of the detected protons rises, the "plateau" becomes longer. The reason for this is that protons which have a higher energy at ejection from the source are able to "survive" for a longer period of time and are

therefore able to propagate a larger distance, even if they lose energy due to various processes.
The curves for the continuous source in 4.23, labeled 5, shows an interesting feature. It rises as the inner part of the cluster is approached. This shape is caused by the continuous injection. Protons that are emitted shortly before the source pulse ends, propagate only a short distance, they do not have much time to diffuse from the source. The rise is therefore prominent for the first few megaparsec of the supercluster. Figure 4.23 shows also that only protons with $E > 10^{16}$ eV can arrive on Earth. Protons with smaller E diffuse during their propagation and do not "survive" a distance of $r = 17$ Mpc.

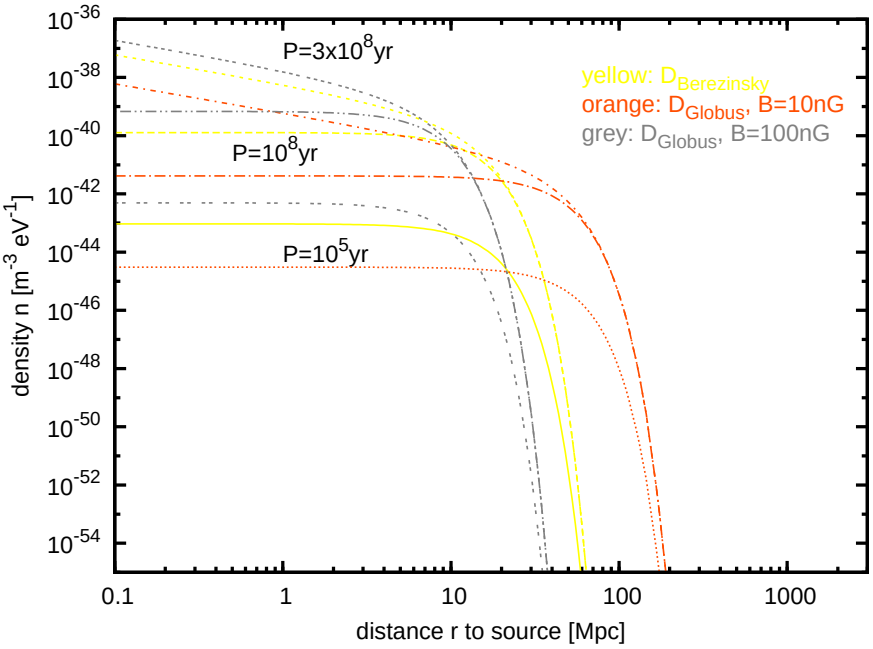

Figure 4.24: The influence of $D(E)_{\text{Globus}}$ on the proton density across the supercluster. All protons are detected with an energy of $E = 10^{19}$ eV at various points inside the cluster. The yellow curve is the same as in figure 4.23. The propagation time is $t_f = 3 \times 10^8$ yr.

Figure 4.24 takes the curve of $E = 10^{19}$ eV as base to compare the influence of $D(E)_{\text{Globus}}$ and $D(E)_{\text{Berezinsky}}$. To guide the eye, the yellow curve is the same in both figures 4.23 and 4.24. In figure 4.24 only three pulses are displayed: $P = 10^5$ yr, $P = 10^8$ yr and $P = 3 \times 10^8$ yr. At first sight, the general shape of the curves does not change with the choice of diffusion coefficient. However, the different coefficients have an influence on the individual curves. When $D(E)_{\text{Globus}}$ and a field of $B = 10$ nG are applied, the protons reach farther distances than for $B = 100$ nG. This means that protons with a certain energy can overcome the magnetic field of $B = 10$ nG easily and propagate a longer distance than field of $B = 100$ nG would allow. If the orange and the grey curves are compared, on sees clearly that they orange curves start to decline later. Both field strengths have the same properties when it comes to the

different pulses P. As before, a higher density is detected as the pulse length rises — a longer source activity yields more protons and therefore a higher density. The rise for the case of $P = t_f$ for small r can be seen, too.

Anisotropy

The corresponding anisotropies for the curves presented in figure 4.24 are shown in figure 4.25. The results look quite different from the previous anisotropy plots. This has two reasons: First, not the energy, but the distance dependence of the anisotropy is shown and second, the used formula for the anisotropy is different from equation 2.8. This equation cannot be used, since it only holds for a fixed distance r. Now, the anisotropy is calculated by

$$\begin{aligned} \delta &= \frac{3\,D(E)}{c\,n} \times \frac{\Delta n}{\Delta r} \\ &= \frac{3\,D(E)}{c\,n} \times \frac{n(E, r+\Delta r, t) - n(E, r, t)}{(r+\Delta r) - r}, \end{aligned} \tag{4.1}$$

which causes the ragged course of the curves. The individual values for $n(E, r, t)$ are very small, therefore also the difference Δn. To provide an exact course for the anisotropy curves, Δn is chosen very narrow, causing the ragged curves. Solving this purely numerical problem and is a task for future work. This would lead to a smooth course of the curves. But the general shape of the curves is the feature one is interested in, so the raggedness is a tolerable problem.
The colours represent the same diffusion coefficients as in figure 4.24: yellow $D(E)_{\text{Berezinsky}}$, orange and grey $D(E)_{\text{Globus}}$. Also the pulse periods are the same as in 4.24. The shortest pulse yields the bottom curve of every colour. The yellow curves peak at a distance of $r = 40$ Mpc with an anisotropy between 30% and 40%. The grey curves have their maximal anisotropy at a shorter distance (20 Mpc) and reach only a maximal anisotropy value of 20%. The peaks in figure 4.25 are, as for earlier plots, related to the change of n. The maxima occur at those energies, where the change of n is the largest. This causes a maximal change in $\frac{\Delta n}{\Delta r}$ and therefore both features arise at the same E.
Since equation 4.1 contains the density difference, $n(r) - n(r + \Delta r)$, its value grows as the density changes much within a small distance Δr. The distance at which the anisotropy has its biggest value is purely determined by the calculations, but it coincides with the distance the Earth has from NGC 4151 for the grey $B = 100$ nG curves.
For the continuous source case, $P = 3 \times 10^8$ yr, the anisotropy grows as the centre of the LSC is approached. This rise occurs for all curves and is independent of the actual diffusion coefficient. The reason for the increase of the anisotropy is the rising density, which was seen in figure 4.24 already. If the protons are detected close to the source, one consequently measures protons that come from the direction of the source and therefore the anisotropy rises for smaller r. If the anisotropies in 4.25 are

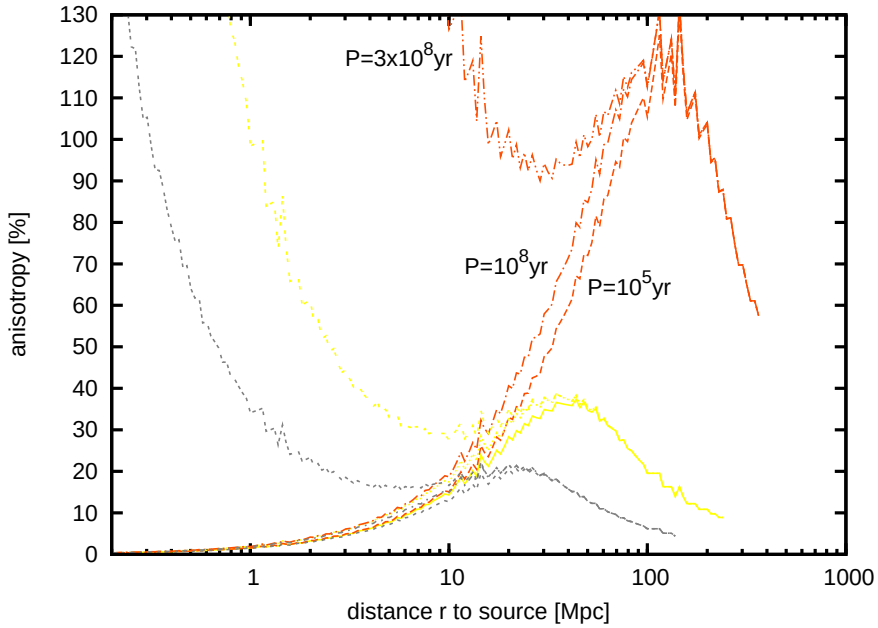

Figure 4.25: The corresponding anisotropies to figure 4.24 are presented here. The colours represent the same field strengths as before. All curves have the same energy at detection $E = 10^{19}$ eV and are calculated with equation 4.1.

compared to the Auger measurements in [25], it is visible that magnetic fields have to be larger than $B = 10$ nG and $P < t_f$.

The next to last subsection in 4.4 described the densities that arise when the propagation time is prolonged to $t_f = 10^9$ yr. The following figure examines this for the case of a varying distance r to the proton source.

The yellow curves that were introduced in figure 4.23 are displayed again to give values where the other curves can be compared to. They exhibit the propagation time of $t_f = 3 \times 10^8$ yr, all other curves (red, blue and green) in 4.26 have a propagation time of $t_f = 10^9$ yr. Every colour has two different pulses, $P = 10^8$ yr and $P = 10^9$ yr to compare between a very short pulse and the continuous case. All curves in figure 4.26 deal with an energy at detection of $E = 10^{19}$ eV of the protons.

First the attention is turned to the difference between the yellow and red lines. Both are calculated with the Berezinsky diffusion coefficient, but have different propagation times t_f. One would assume that the proton density decreased with longer t_f and this can actually be seen in the figure. The bottom curves (both red and yellow) have a pulse period of $P = 10^8$ yr, but the red curve shows a density that is about one order of magnitude lower than the yellow one. For a longer t_f the particles have more time to diffuse and interact, so the number of protons that are detected at a certain distance r decreases. An interesting feature can be seen for those curves, when the continuous ejection case is displayed. This happens for the upper red and yellow curves. For the red curve the values are $t_f = P = 10^9$ yr, for the yellow one $t_f = P = 3 \times 10^8$ yr.

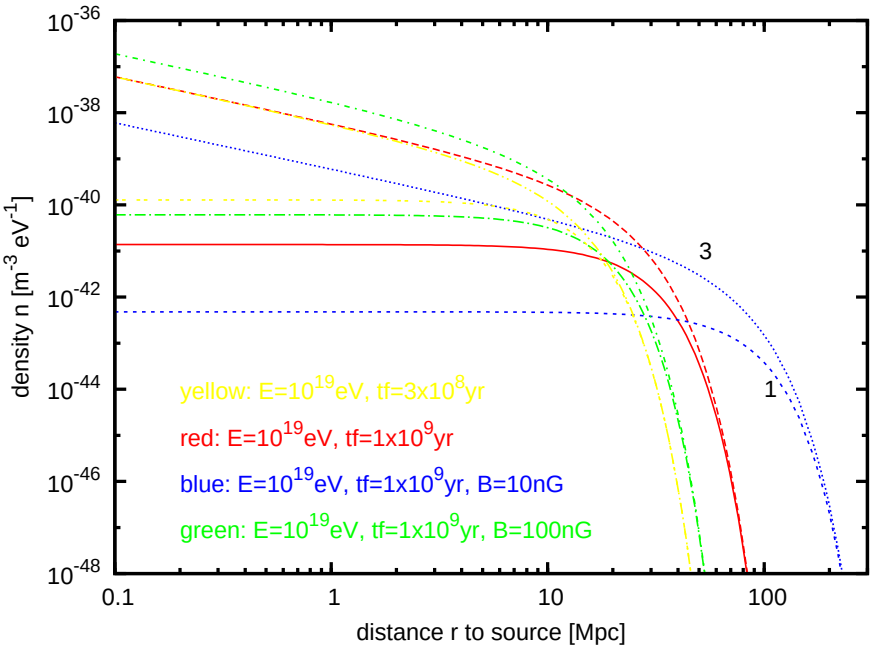

Figure 4.26: The proton density within the cluster for a propagation time of $t_f = 10^9$ yr (red, blue, green) and $t_f = 3 \times 10^8$ yr (yellow). The numbers represent different pulses: 1: $P = 10^8$ yr and 3: $P = 10^9$ yr, where the short pulse corresponds to the lower curves. The energy at detection E is still $E = 10^{19}$ eV.

Both lines show the increase in density when small distances are approached, as was discussed earlier in 4.24. Moreover, they converge for small distances. Apparently, the propagation time does not have a large influence when $P = t_f$ and $r < 1$ Mpc are examined. In both cases are protons constantly ejected, so the density rises close to the source, no matter what the actual propagation time is. When distances larger than $r = 10$ Mpc are considered, both lines diverge. For a longer t_f protons have more time to propagate and are able to reach farther distances. The red lines start to decline at $r = 30$ Mpc, the yellow ones on the other hand already at $r = 10$ Mpc. In figure 4.24 it could be seen that for a $B = 10$ nG field the protons could generally propagate further out into the supercluster than for a 100 nG field, because large magnetic fields keep the protons close to the source. This is also visible in 4.26, the blue curves start to decrease at roughly $r = 110$ Mpc, which is already outside of the supercluster. In contrast, the green curves drop around $r = 10$ Mpc already.

Anisotropy

The corresponding anisotropies are presented in figure 4.27.

The previous anisotropy plot for $t_f = 3 \times 10^8$ yr showed that the anisotropy has reasonable values, as long as P is shorter than t_f. For the continuous source case the anisotropy rises to unphysical high values in figure 4.25. A very similar picture can be seen for the anisotropy in case of $t_f = 10^9$ yr. As for the density plot, first the

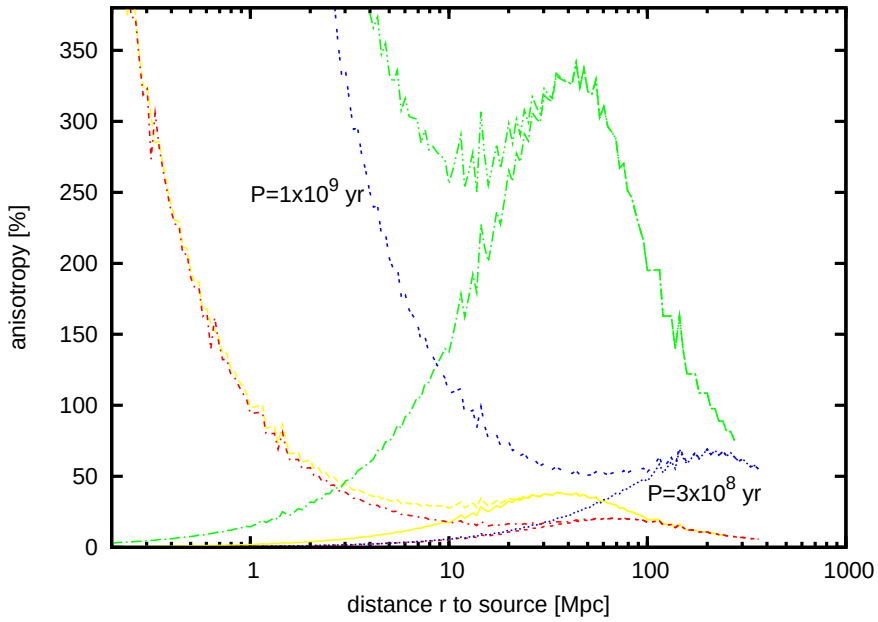

Figure 4.27: The anisotropies for a prolonged time $t_f = 10^9$ yr. The colours in this plot correspond to the ones in figure 4.26: yellow: $D_{\text{Berezinsky}}$ with $t_f = 3 \times 10^8$yr, red: $D_{\text{Berezinsky}}$ with $t_f = 10^9$yr, blue: D_{Globus} with $B = 10$ nG, green: D_{Globus} with $B = 100$ nG.

yellow and red curves are compared, since they show the general difference between the two propagation times. In figure 4.27 only two different pulses are displayed, $P = 3 \times 10^8$ yr and $P = 10^9$ yr. The rise of the proton density for small distances is also seen. As the case of $P = t_f$ is considered, the anisotropy rises steeply as r decreases. In figure 4.26 it could be seen that the yellow and red curves converged for small distance and $P = t_f$. This feature appears in figure 4.27 too, the lines converge for $r < 3$ Mpc. The maxima of both curves are however to be found at different distances to the source, $r = 30$ Mpc and $r = 70$ Mpc. In terms of the Auger measurements in [25], the case of $t_f = 3 \times 10^8$ yr is more favourable.
The blue curves denote the case of $B = 10$ nG, the green ones $B = 100$ nG for $t_f = 10^9$ yr and $D(E)_{\text{Globus}}$. The maxima of the curve for $B = 10$ nG and $P = 3 \times 10^8$ yr occurs for $r > 100$ Mpc and has a value of more than 50%. This corresponds to the course of the curve in the density plot 4.26. At the vicinity of the Earth the anisotropy lies below 20%. When the $B = 10$ nG curves are compared to the $B = 100$ nG curves in figure 4.27, an unexpected feature arises. In all previous figures, the anisotropy for the 100 nG field was smaller, here it is suddenly larger. Even the short pulse curve blows up and yields a very high anisotropy. The continuous source curve is depicted in 4.27 only, to show that the overall behaviour is in principle the same as for the other "continuous curves".

Recalling the various plots in this chapter one can conclude that the density distribution of UHE protons inside the supercluster is strongly dependent on all parameters,

the pulse length P, the propagation time t_f and the magnetic fields. Also the choice of $D(E)$ influences the intensity and anisotropy. The Auger anisotropy measurements seem to favour a magnetic field larger than $B = 10$ nG for the case of $D(E)_{\text{Globus}}$. The case of $D(E)_{\text{Berezinsky}}$ actually matches the Auger measurements even better, although there the magnetic field is only slightly higher than nanogauss size. Berezinsky et al. assumed a field of $B = 2 \times 10^{-8}$ G. The density plots give valuable information about the proton density as it could be measured at Earth. With this information the spectra of secondary particles could be calculated. The proposed rates could vary from the ones gained by propagation codes where the proton density is often assumed to be constant. If such propagation codes included the change of the proton density, the results would describe the actual physical situation a lot better.

4.6 Calculations for $E = 6.3 \times 10^{19}$ eV

The calculations in the previous section are performed for an energy at detection of $E = 10^{19}$ eV. But since Auger measured the anisotropy for an energy of a few 10^{19} eV, it is instructive to examine this detection energy as well. The figures in this section correspond to figures 4.24, 4.25, 4.26 and 4.27 of section 4.5, the only difference being $E = 10^{19.8}\text{eV} = 6.3 \times 10^{19}$ eV.
First the change in proton density across the supercluster is presented for a propagation time of $t_f = 3 \times 10^8$ yr. Figure 4.28 presents the difference between the two diffusion coefficients for this certain propagation time. The blue curve in this plot is the same as in figure 4.23, it describes the density for $E = 10^{19.8}$ eV and $D(E)_{\text{Berezinsky}}$ and is shown to guide the eye. The orange and grey lines show the influence of $D(E)_{\text{Globus}}$. The presented pulses are $P = 10^5$ yr, $P = 10^8$ yr and $P = 3 \times 10^8$ yr.
The general behaviour of the grey and orange curves agrees well with the expectations from the figures of the last section. It can be seen that the longer the pulse P, the higher the resulting density at Earth. The distance over which the proton density declines slowly is larger for longer P. The curves for $P = 10^8$ yr decline steeply at $r \sim 100$ Mpc. When looking at the short pulse $P = 10^5$ yr curve, the decline sets in at a distance of $r \sim 80$ Mpc already. The continuous source case shows a steady increase in the spatial density as the inner parts of the supercluster are approached. This corresponds well with earlier results of $E = 10^{19}$ eV in figure 4.23.
The most interesting feature of this figure is the comparison between the different magnetic field strengths for $D(E)_{\text{Globus}}$ — there is no difference! The orange curves for $B = 10$ nG and the grey curves for $B = 100$ nG coincide. This seems surprising at first, but becomes clear as the figures 4.15 and 3.1 are examined. While carefully studying figure 4.15, it can be seen that for energies above $E = 5 \times 10^{19}$ eV, the orange and the pink curves for the different magnetic fields fall together. This is seen most clearly for the case of $P = 3 \times 10^8$ yr in figure 4.15. At this point the limitation for $D(E)$ sets in for both cases $B = 10$ nG and $B = 100$ nG. Hence the agreement of the curves in figure 4.28 is no coincidence, since the arrival energy of $E = 6 \times 10^{19}$ eV lies in the region of $D(E)_{\text{max}}$. In this figure the density rises for small r and the continuous

source is seen again.

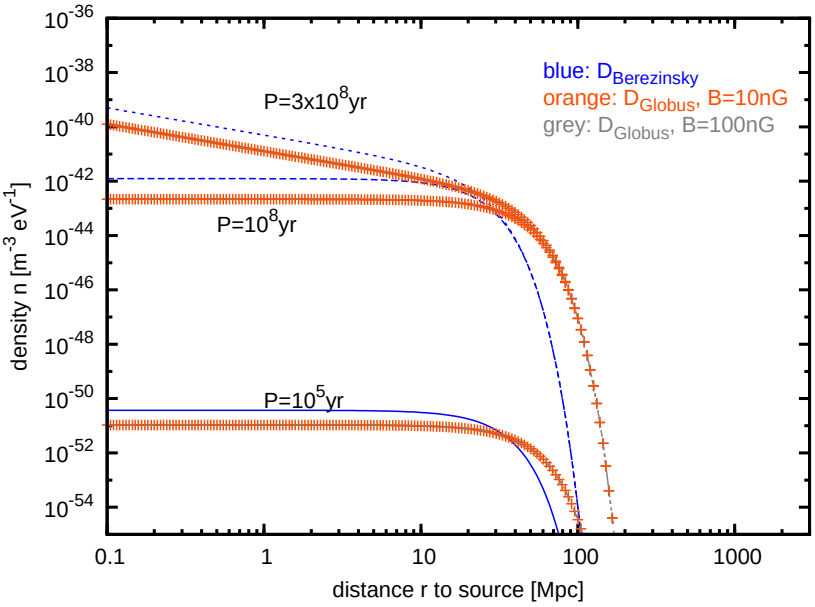

Figure 4.28: The proton density within the supercluster when an energy at detection of $E = 6.3 \times 10^{19}$ eV is assumed. The figure compares the influence of the different diffusion coefficients and shows the source pulses $P = 10^5$ yr, $P = 10^8$ yr and $P = 3 \times 10^8$ yr.

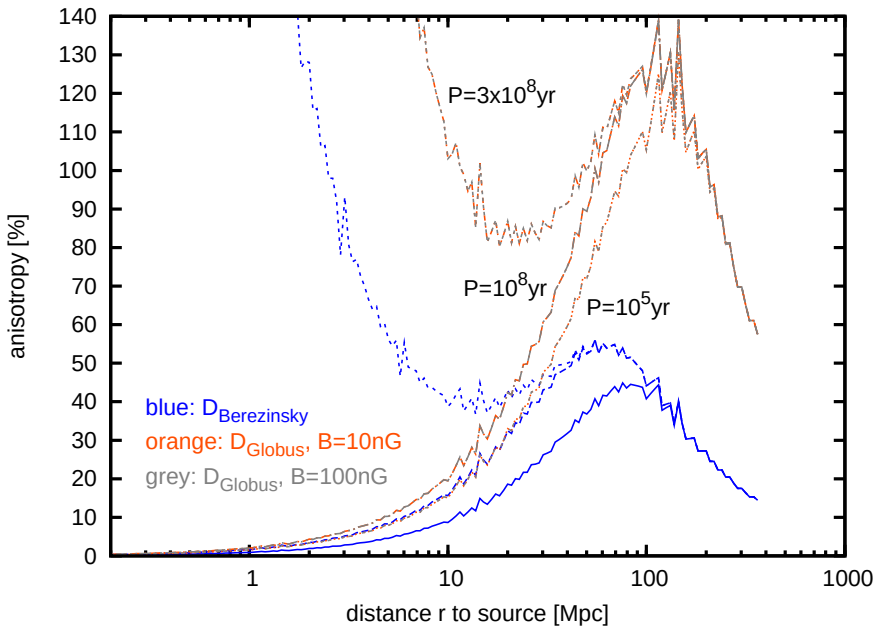

Figure 4.29: The corresponding anisotropy for the parameters used in figure 4.28. The same source pulses and the same diffusion coefficients are used. The anisotropy is calculated with equation 4.1.

The agreement of the $D(E)_{\text{Globus}}$ curves can also be seen for the anisotropy curves. Figure 4.29 shows the anisotropy that arises for the curves in figure 4.28. In the vicinity of the Earth at $r \sim 17$ Mpc, the anisotropy is roughly 30% – 40%, which goes well with the Auger measurements. The continuous source curves yield, as in the previous section, values of more than 100% anisotropy. The curves for $D(E)_{\text{Berezinsky}}$ give more reasonable results. They show an anisotropy of maximal 60% for source pulses shorter than the propagation time t_f. For the distance of $r = 17$ Mpc, they yield values between 15% and 30%. The anisotropy is even slightly higher as for the case of $E = 10^{19}$ eV in figure 4.25.
The rise in anisotropy for t_f=P and small r is also seen in figure 4.29.

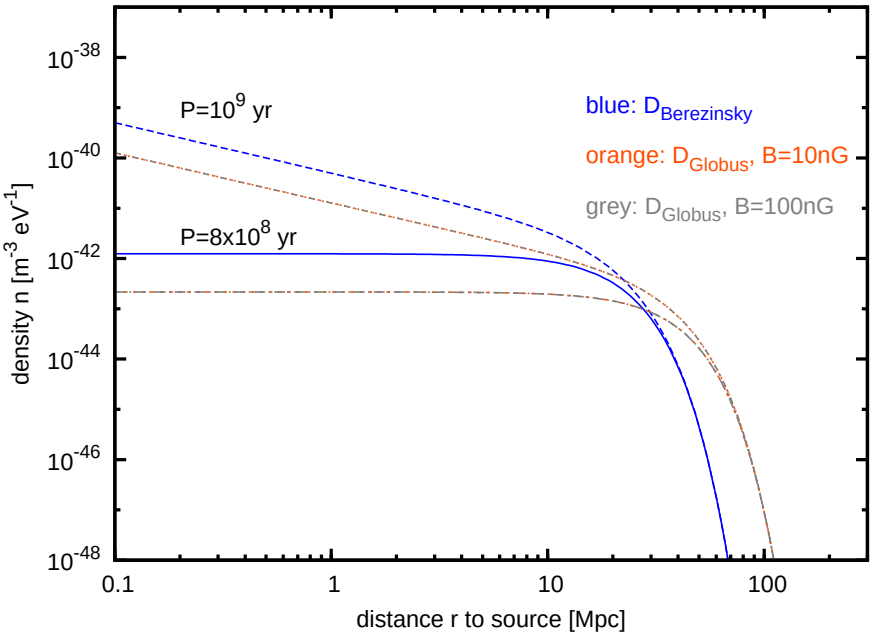

Figure 4.30: The proton density as a function of distance to the source at a propagation time of $t_f = 10^9$ yr. The curves for two different pulse lengths, $P = 8 \times 10^8$ yr and $P = 10^9$ yr, are shown. The orange and grey curves coincide due to $D(E)_{\text{max}}$.

Figure 4.30 displays how the proton density changes if the propagation time is prolonged to $t_f = 10^9$ yr. The values do not change much. As before, the curves for the continuous source case rise as smaller r are approached. This figure depicts again that for an energy of $E = 10^{19.8}$ eV there is no difference between the magnetic field strength of 10 nG and 100 nG when $D(E)_{\text{Globus}}$ is used.
The corresponding anisotropy curves for figure 4.30 are presented in figure 4.31. This shows the anisotropy for $D(E)_{\text{Berezinsky}}$ and for $D(E)_{\text{Globus}}$. Since $B = 10$ nG and $B = 100$ nG will give the same results, only the case of $B = 10$ nG is presented in the figure. If this is compared to figure 4.29, where the same situation is presented for $t_f = 3 \times 10^8$ yr, one cannot tell a big difference between the two plots. This is not surprising, the corresponding density plots 4.30 and 4.28 showed similar results, too. If the information the anisotropy plots give is used to constrain the magnetic fields, the

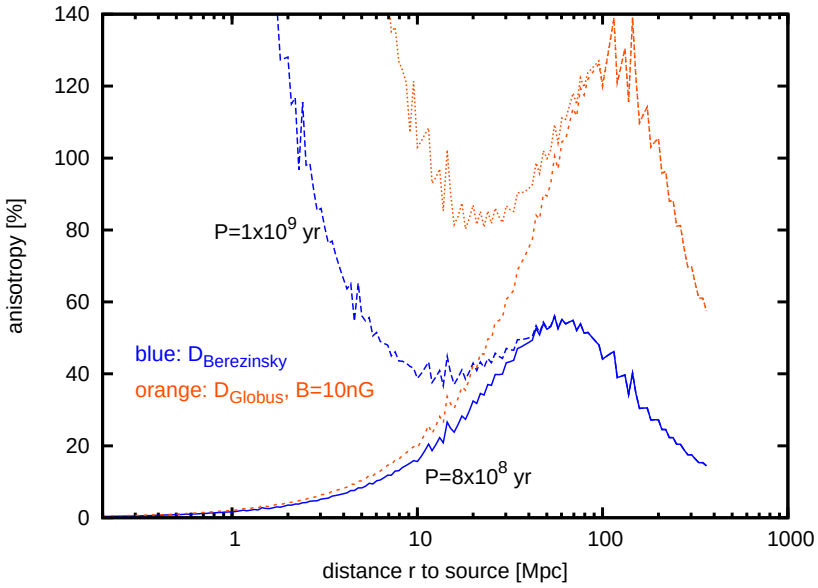

Figure 4.31: The corresponding anisotropies for figure 4.30. The calculations are performed again with equation 4.1. The choice of parameters is the same as for figure 4.30.

same things are to be found as for the case of $E = 10^{19}$ eV. The best agreement with the Auger measurements is achieved when $D(E)_{\text{Berezinsky}}$ is used and pulses $P < t_f$ are considered. Therefore suitable magnetic fields have to be larger than $B = 10$ nG.

4.7 Comparison with Auger data

The energy spectra data is taken from a recent paper of the Auger collaboration, [1] and can be found at the website *http://www.auger.org/combined spectrum icrc09.txt*. The aim is to match the curves from the density calculations of this data from the collaboration.

The scaling point is chosen to be $E = 7 \times 10^{19}$ eV, since the Auger spectrum shows a distinct kink at this energy, the GZK-cutoff. The calculated curves have to be "shifted" until the bump in the curves matches the one of the Auger data. This is done by varying the propagation time t_f. For the comparison with real data, the case of a continuous proton source, $t_f = P$, is assumed, because this is the only way to provide a significant intensity I for $E > 10^{20}$ eV. Figure 4.32 shows the curves for different propagation times. As t_f becomes shorter, the entire curve is not only shifted towards lower intensities, but also to higher energies E. If the propagation time is short, only very energetic protons are able to propagate a certain distance within a given time t_f. The shorter the propagation time, the more energetic must the protons be. The calculations for the blue curves are performed with the diffusion coefficient used by Berezinsky et al. The best agreement occurs for a time of $t_f = 2 \times 10^8$ yr. This propagation time is used for the remaining calculations of this section.

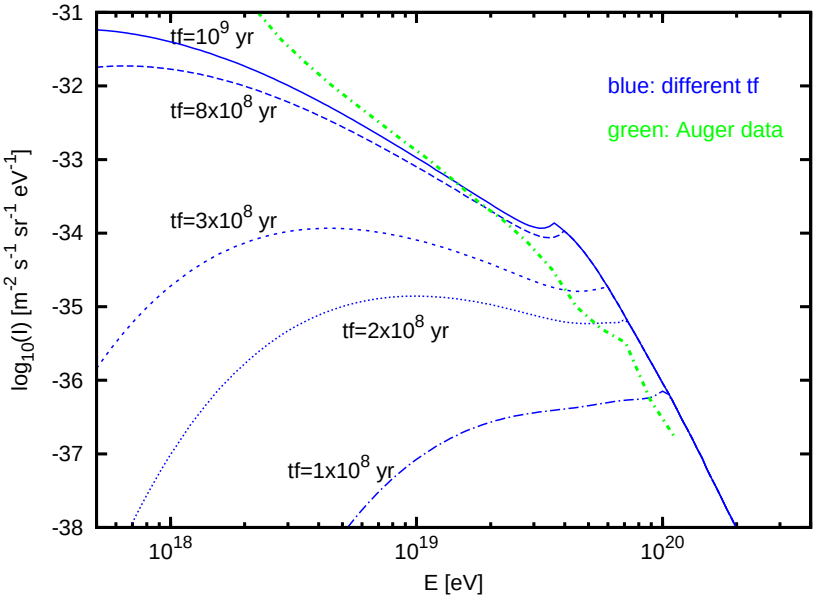

Figure 4.32: The spectrum of UHE protons as measured by the Auger observatory. The Auger data (in green) is taken from the Auger website, *http://www.auger.org/combined spectrum icrc09.txt*. The blue curves show the calculations from this study for different propagation times t_f.

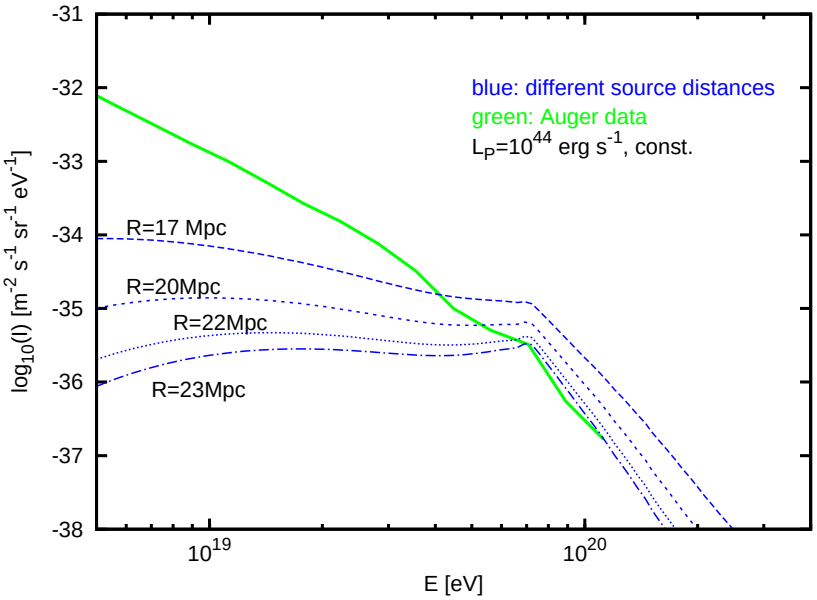

Figure 4.33: The resulting spectra for different distances R to the cosmic ray source, as the source luminosity is fixed. The curves are calculated with $D(E)_{\text{Berezinsky}}$.

Now the curve is scaled to the right intensity values. This can be done by adjusting several parameters, but only two will be examined here: the distance to the source R and the cosmic ray luminosity of the source, L_p. The influence of the different diffusion coefficients is considered as well.
The cosmic ray luminosity is fixed to $L_p = 10^{44}\,\mathrm{erg\,s^{-1}}$ and a possible distance R is to be determined where the spectrum matches the Auger measurements. The results for various distances are depicted in figure 4.33, where one can see that the curve for $R = 23$ Mpc agrees best. The GZK-cutoff is exactly at the same position as the Auger curve indicates. The decrease in I for energies above $E = 7 \times 10^{19}$ eV corresponds also to the green curve, although the values do not match completely. For smaller E the difference of the curves is more obvious. The curves from this study lie well below the Auger data points. This is seen especially well for $E \sim 10^{19}$ eV. A possible explanation is the injection spectrum with which the protons are emitted from the source. Up to now, protons with energies up to $E = 1.22 \times 10^{28}$ eV are ejected with a spectral source index of $\gamma_g = 2.1$. Future studies could change this in a way that more protons with energies around $E = 10^{21} - 10^{23}$ eV are emitted. Those would then be detected in the energy range below $E = 10^{20}$ eV. The intensity would rise in this region and match the Auger results better.
If one assumes the luminosity to be $L_p = 10^{44}\,\mathrm{erg\,s^{-1}}$, this means that the astrophysical object which is responsible for the acceleration of cosmic ray protons is not situated in the centre of the local supercluster, 17 Mpc away from Earth. The calculations imply a source at $R = 23$ Mpc, which would be positioned "behind" the centre.

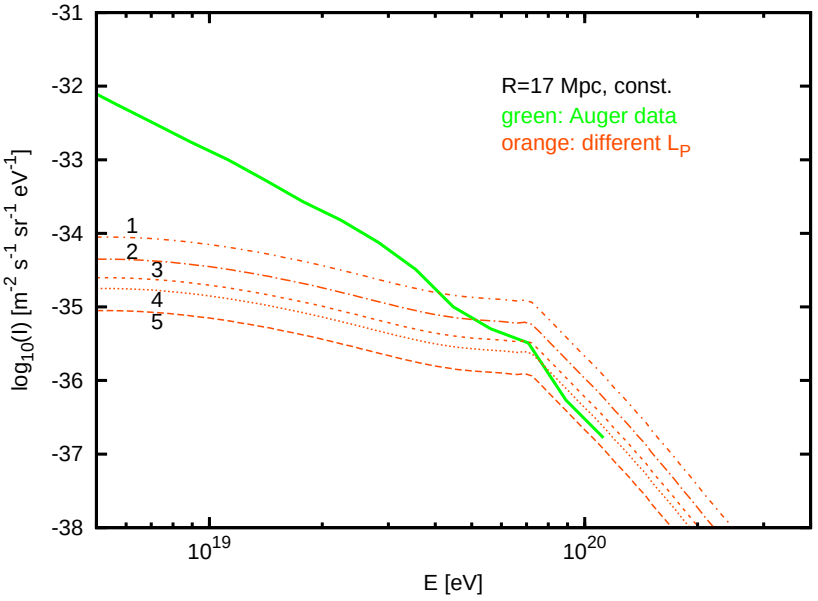

Figure 4.34: The cosmic ray spectra for variable cosmic ray luminosities L_p. The numbers indicate: 1: $L_p = 10^{44}\,\mathrm{erg\,s^{-1}}$, 2: $L_p = 5{\times}10^{43}\,\mathrm{erg\,s^{-1}}$, 3: $L_p = 2.8 \times 10^{43}\,\mathrm{erg\,s^{-1}}$, 4: $L_p = 2 \times 10^{43}\,\mathrm{erg\,s^{-1}}$ and 5: $L_p = 10^{43}\,\mathrm{erg\,s^{-1}}$.

Figure 4.34 displays the case of different L_p if the distance to the source R is fixed to $R = 17$ Mpc. The different curves in this figure indicate luminosities in the range between $L_p = 10^{43}$ erg s^{-1} and $L_p = 10^{44}$ erg s^{-1}. The Auger curve is reproduced with a choice of $L_p = 2.8 \times 10^{43}$ erg s^{-1}. A typical source of this luminosity would be an AGN as numbers in [3] indicate.

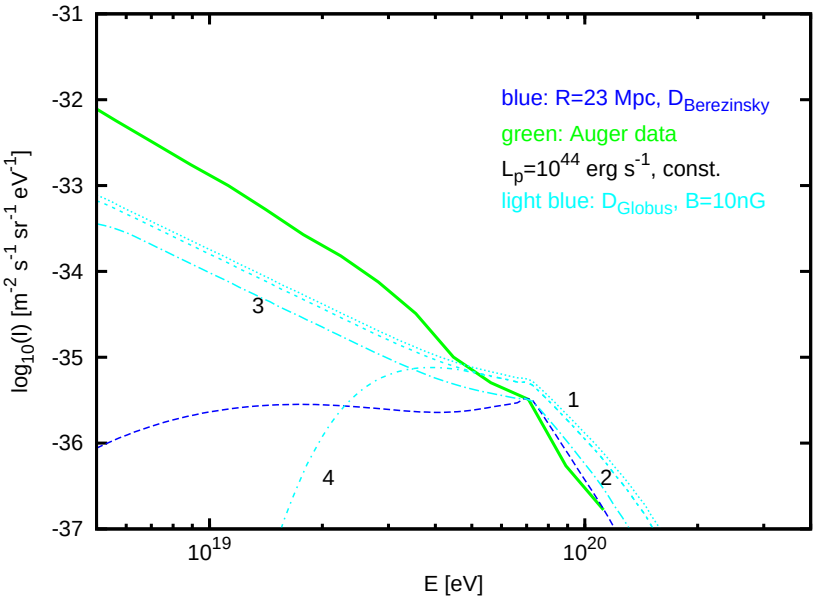

Figure 4.35: This figure shows the intensity for $D(E)_{\text{Globus}}$ (light blue) with a magnetic field of $B = 10$ nG and a fixed cosmic ray luminosity. For comparison, the matching $D(E)_{\text{Berezinsky}}$ curve with $R = 23$ Mpc is shown. The numbers indicate different distances of 1: $R = 22$ Mpc, 2: $R = 23$ Mpc and 3: $R = 27$ Mpc. The curve labeled 4 exhibits the parameter choice of $R = 23$ Mpc and $B = 100$ nG.

Then it is examined how the obtained results change, if $D(E)_{\text{Globus}}$ is taken into consideration. All previous results were obtained with $D(E)_{\text{Berezinsky}}$, now the influence of the change of magnetic fields is discussed. Figure 4.35 displays the difference between the diffusion coefficients for the case of a fixed cosmic ray luminosity of $L_p = 10^{44}$ erg s^{-1}. For the case of $D(E)_{\text{Berezinsky}}$, the best agreement to the Auger data was achieved with a distance of $R = 23$ Mpc to the cosmic ray source. This is shown in the dark blue curve in figure 4.35. As the magnetic fields $B = 10$ nG and $B = 100$ nG are examined, this distance does not match any longer with the Auger data. As seen in figure 4.35, the curve with $R = 23$ Mpc yields then an intensity that is too high in comparison with the previous results. More protons would arrive than the data suggests.
The curve labeled 4 exhibits the same distance $R = 23$ Mpc as curve number 2, but has the field strength of $B = 100$ nG instead of $B = 10$ nG. The intensity for this choice of B-field yields a greater divergence from the Auger results for $E < 4 \times 10^{19}$ eV, so only the case of $B = 10$ nG is considered for the following calculations. The resulting

curves match the Auger data only when a distance of $R = 27$ Mpc is chosen. This means that if there was a magnetic field of $B = 10$ nG present in the supercluster, the cosmic ray source could not be situated in the centre of the supercluster. It had to be even farther away than the results from the previous paragraph indicated.

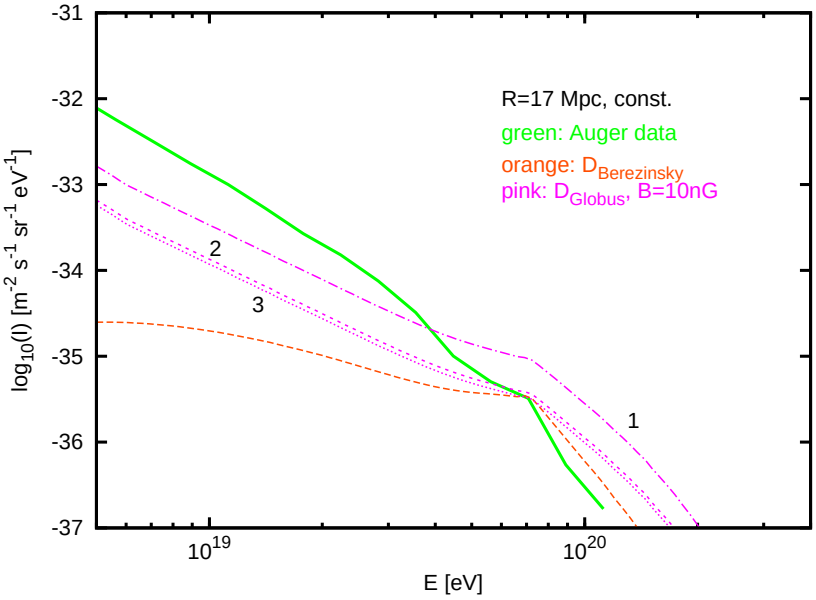

Figure 4.36: This shows the spectra for fixed distance R=17 Mpc, but different cosmic ray luminosities L_p and a magnetic field of 10 nG (pink lines). The curve that was obtained for $D(E)_{\text{Berezinsky}}$ is depicted in orange for comparison. The luminosities are 1: $L_p = 10^{44}$, 2: $L_p = 4 \times 10^{43}$, 3: $L_p = 3.5 \times 10^{43} \frac{\text{erg}}{\text{s}}$.

The curves in figure 4.36 show the results for a variable cosmic ray luminosity and a fixed B-field of $B = 10$ nG. The distance is set to $R = 17$ Mpc. Additionally, the matching curve with $D(E)_{\text{Berezinsky}}$ from figure 4.34 is shown again in orange. This has a luminosity of $L_p = 2.8 \times 10^{43}\,\text{erg}\,\text{s}^{-1}$ and a magnetic field of $B = 2 \times 10^{-8}$ G. The cosmic ray luminosity slightly changes for the choice of $D(E)_{\text{Globus}}$. As can be told from figure 4.36, the best agreement is now achieved with a luminosity of $L_p = 3.5 \times 10^{43}\,\text{erg}\,\text{s}^{-1}$. When a field of $B = 10$ nG is present, a slightly higher luminosity is needed to match the Auger results than before.

To conclude the discussion from this section, one can say that depending on the initial choice of parameters, the calculations of this study yield values that roughly match the data taken with the Auger experiment and describe source that could actually be present in the local supercluster. For a given cosmic ray luminosity of $L_p = 10^{44}\,\text{erg}\,\text{s}^{-1}$, the calculations suggest a source with a distance of $R = 23 - 27$ Mpc from the Earth, depending on the diffusion coefficient and the magnetic field that is present in the supercluster. The parameters choices that give those results seem reasonable. When the central region of the cluster is assumed to be the source of

the UHE protons, then a distance to the source of $R = 17$ Mpc has to be considered. For this case, the calculations suggest a source luminosity $L_p = 2.8 \times 10^{44}\,\mathrm{erg\,s^{-1}}$ for $D(E)_{\mathrm{Berezinsky}}$ and $L_p = 2.8 \times 10^{44}\,\mathrm{erg\,s^{-1}}$ for $D(E)_{\mathrm{Globus}}$ and $B = 10$ nG. These values do not differ much and could be met if an AGN is taken as a source of cosmic protons. One should keep in mind that throughout the performed calculations the source spectrum at generation was fixed to $E^{-\gamma_g}$ with $\gamma_g = 2.1$. Further studies could investigate how a change in the injection spectrum would influence the resulting proton spectra.
In general all curves from this section yield similar values as the Auger experiment for proton energies of $E > 7 \times 10^{19}$ eV. For $E < 7 \times 10^{19}$ eV, the results from this study and Auger do not agrees so well, the calculated curves lie below the Auger data curve. How this can be matched is work for future studies, as well.

Finally, also the anisotropy and actual density distribution for the best agreement curves are displayed in figures 4.37 and 4.38. The anisotropy is calculated with equation 2.8 for the individual parameter sets. The specific numbers can be found in the figure. One sees that although the intensity curves matched the Auger measurements, the corresponding anisotropies do not.

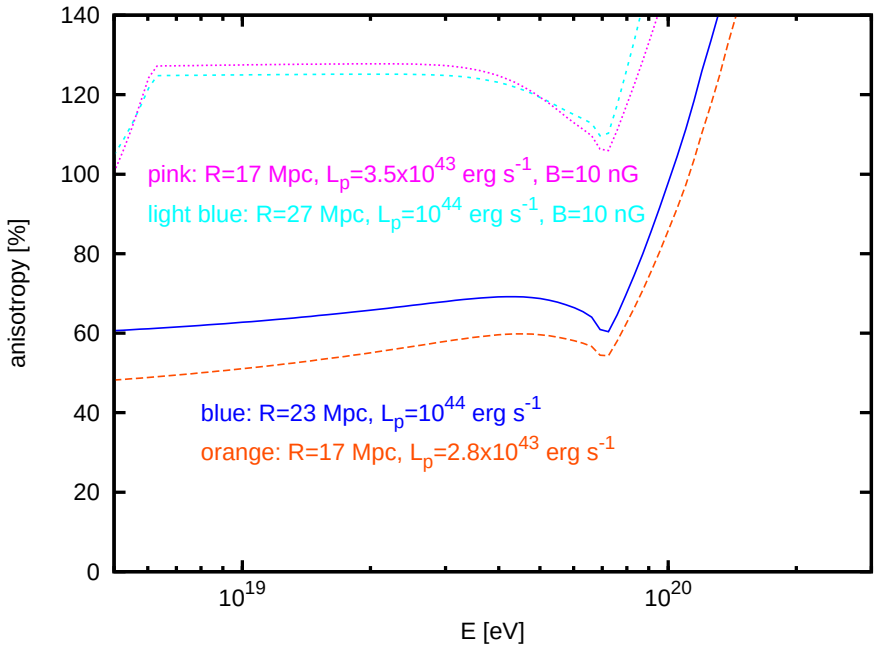

Figure 4.37: This figure shows the anisotropies for the parameters that best match with the Auger data. The curve colours correspond to the other figures of section 4.7. The parameters for the individual curves can be found in the plot. The anisotropy is calculated with equation 2.8.

All curves show a dip at $E = 7 \times 10^{19}$ eV, which corresponds to the GZK-cutoff in the spectrum, as mentioned before in this section. For $E < 7 \times 10^{19}$ eV, the curves show a

steady rise where the anisotropy values lie in the range of 50 – 60% for $D(E)_{\text{Berezinsky}}$ or above 100 % for $D(E)_{\text{Globus}}$. These numbers do not agree at all with the measured anisotropy of $\sim 30\%$ from Auger in [25], they are generally too large. For the curves with $D(E)_{\text{Globus}}$ one can again see the begin of $D(E)_{\max}$ at $E = 7 \times 10^{18}$ eV. The first parameters that could be adjusted to match the anisotropy are the magnetic field B and the source output.
The corresponding proton density distribution is shown in figure 4.38. It shows the density as calculated from the date at *http://www.auger.org/combined spectrum icrc09.txt* in green, the other curve colours correspond to the previous figures. It can be seen that the densities for an energy at detection of $E > 7 \times 10^{19}$ eV match well. This was also visible before in the intensity figures 4.35 and 4.36. Below this value the individual curves diverge from the Auger curve.
The density curves for the different diffusion coefficients show in general a similar behaviour as already discussed in figure 4.15 in section 4.3.2.

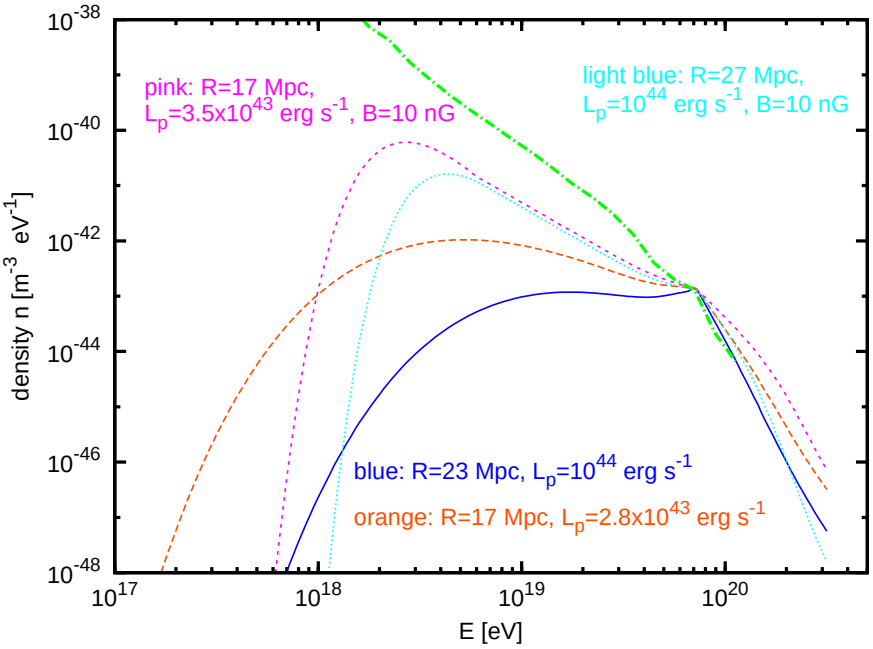

Figure 4.38: The proton density distribution for the best parameters that should best agree with the Auger data. The chosen values are indicated at the curves.

The blue and orange curve for $D(E)_{\text{Berezinsky}}$ exhibit the same shape as in 4.15, but show a slightly steeper decline for $E < 10^{18}$ eV. The shorter the propagation distance R is for the protons, the larger the density at detection. Therefore the orange curve yields higher values than the blue one. The different cosmic ray luminosities do not change this behaviour. This feature also seen for the case of $D(E)_{\text{Globus}}$: The pink curve for $R = 17$ Mpc yields a higher proton density as the curve for $R = 27$ Mpc. Although the cosmic ray luminosity is larger for $R = 27$ Mpc, the propagation distance seems to have a greater influence on the density distribution. The peaks for

$D(E)_{\text{Globus}}$ yield higher density values than the $D(E)_{\text{Berezinsky}}$ curves. This was also visible in figure 4.15 before.

Chapter 5

Summary & Outlook

The following paragraphs sum up the most important issues that were discussed within this work and give an outlook on how the gained results can be used in the future.

The main task of this thesis was to investigate the spatial density of ultra-high energy protons within the local supercluster of galaxies. The calculations are based on the injection of the protons by a single, pulsed source of certain distance to the Earth. The equation 2.4, first presented by Berezinsky et al. [4] and [5], includes the diffusion of the protons, as well as energy losses due to collision with photons from ambient photon fields. The density of UHE protons can be calculated as a function of the energy E at detection at a certain distance r from the source at a certain time t after the source was switched on and a variable source pulse P. This study extends the analysis of Berezinsky et al. in such a way that not only the cosmic microwave background photons were considered, but also the influence of the extragalactic background light and the supercluster radiation field. Two different diffusion coefficients $D(E)$, one by Berezinsky et al., the other by Globus et al. [13], were examined. This allowed to study the influence of different magnetic fields on the diffusion and propagation of the protons. The results are found in section 2.3.
Prior to the actual density calculations, a detailed study on the different energy loss processes was done and is presented in section 4.2. There, the influence of the individual photon fields is discussed. The density calculations were first performed to reproduce the results of Berezinsky et al., the "test source" being the Seyfert I galaxy NGC 4151. Then the diffusion coefficient by Globus et al. was used to examine how the results change when different magnetic field strengths are applied. Besides, the change in proton density due to different choices of propagation time and pulse length was studied. The results of the calculations are also compared to anisotropy data from the Auger observatory, [25]. The best agreement that was achieved occurred when $D(E)_{\text{Berezinsky}}$ or $D(E)_{\text{Globus}}$ with a magnetic field of more than $B = 10$ nG was applied for a source pulse shorter than the propagation time. In section 4.7 the calculations were matched to recent measurements of the energy spectrum by Auger.

The computer code of this thesis can be used for various calculations in the future. But before this can be done, the numerical problem of anisotropies larger than 100% should be taken care of. A detailed investigation of the code should solve this problem. Then, calculations towards a better agreement with the anisotropy measurements by Auger could be performed. A possible approach could be the change of spectral index of the source and the energy at generation, since this was not studied in detail in this thesis.
Moreover, the code could be used to calculate spectra of secondary particles. The amount of secondaries that is produced varies with the density of the primary particles, and this is where the work of this thesis would be of use. The actual change of the primary density can be modelled, taking into account different diffusion and energy loss scenarios. Realistic predictions secondary particle production could be derived and these matched with real data. Furthermore, the proton source can be varied, so individual sources in the supercluster could be tested as sources of ultra-high energy cosmic rays.

Chapter 6

Appendices

Since the energy loss due to interaction of protons with background photons is an essential part of the proton behavior, it is instructive to take a closer look at the derivation of the formulae in chapter 2 that are used to calculate the energy losses. To establish an understanding of the physical properties of the expressions, the appendices deal first with the kinematics of such inelastic collisions and further show the derivation of the formula for $\frac{dE}{dt}$ as it is presented in chapter 2.

Appendix A - Relativistic kinematics of inelastic collisions

The following calculations can also be found in [20], but are also presented here to give an idea on the complexity of the used formulae. Explicit steps of the calculations towards relevant kinematic expression are given. Some important numbers, such as the threshold energy for pion production are calculated as well.
Before the direct calculations are presented, it is good to "warm up" and recall the relation between a particle's energy, its momentum and the gamma factor. From textbooks one finds that the gamma factor (or Lorentz factor) is defined as the quotient of energy and mass

$$\gamma = \frac{E}{m}. \tag{6.1}$$

of a particle. If this is squared and plugged into the expressions for the relativistic energy $E = \sqrt{(pc)^2 + m_0^2 c^4}$ and $m = m_0 c^2$ is inserted, this ends up in

$$\gamma = \sqrt{1 + \frac{p^2}{m_0^2 c^2}}. \tag{6.2}$$

This can be converted to

$$\frac{p}{m_0} = c\sqrt{\gamma^2 - 1}, \tag{6.3}$$

an expression which will be of help later on.

Threshold energy

One should start the derivations from the very beginning and consider in general two inelastically colliding particles, a and b, that form two new particles c and d, $a + b \rightarrow c + d$. They have masses of m_i (i=a, b,...) and their four-momenta look like $P_i = (\frac{\epsilon_i}{c}, \vec{p_i})$, where ϵ_i denotes the particles' kinetic energy. For the production of c and d there must be a minimal energy, the threshold energy, available in the centre-of-mass frame of the reaction that equals at least the rest masses of c and d. Centre-of-mass variables are denoted with a prime. If the invariance of the four-momenta is assumed, one can "write down" the collision for the initial particles as follows:

$$\begin{aligned} E' &= c^2(P_a + P_b) \\ &= c^2(P_a^2 + P_b^2 + 2P_aP_b) \\ &= ... \\ &= m_a^2c^4 + m_b^2c^4 + 2\epsilon_a\epsilon_b - 2c^2\vec{p_a}\vec{p_b} \end{aligned} \tag{6.4}$$

This must equal the threshold energy that is required for the rest masses m_c and m_d, so

$$E'_{th} = m_cc^2 + m_dc^2 = m_ac^2 + m_bc^2 + \Delta mc^2. \tag{6.5}$$

The last equal sign comes from the fact that the energy (and therefore mass) provided by the collision of a and b is larger than the individual rest masses for the resulting particles and denotes the mass difference between incoming and outgoing particles. If the last two expressions, are set equal this gives

$$\epsilon_a\epsilon_b - c^2\vec{p_a}\vec{p_b} = m_am_bc^4 + \Delta mc^4\left(m_a + m_b + \frac{\Delta m}{2}.\right) \tag{6.6}$$

This formula might not seem very intriguing, but will be of need at a later stage in the calculations. From this expression, one can go on. For clarity of the calculations, first all particles are assumed to be massive, so $m_i \neq 0$. Expression 6.6 is multiplied by $\frac{1}{m_am_b}$ on both sides and then left and right side of the equation are examined separately. To transform the left side of 6.6, the old trick of $\vec{a} \cdot \vec{b} = |a||b| \cos\theta$ is used. Moreover the Lorentz factor from 6.3 is inserted. This yields for the left-hand side:

$$\text{lhs}: \quad c^4\gamma_a\gamma_b - c^4\cos\theta\sqrt{(\gamma_a^2 - 1)(\gamma_b^2 - 1)}. \tag{6.7}$$

The angle θ denotes the collision angle between the incoming particles a and b in the laboratory frame. The right-hand side of 6.6 will be converted until:

$$\text{rhs}: \quad c^4 + \Delta mc^4(\frac{m_a}{m_am_b} + \frac{m_b}{m_am_b} + \frac{\Delta m}{2m_am_b}). \tag{6.8}$$

Setting those two expressions equal yields

$$\gamma_a\gamma_b - \cos\theta\sqrt{(\gamma_a^2-1)(\gamma_b^2-1)} = 1 + \Delta mc^4(\frac{1}{m_a}+\frac{1}{m_b}+\frac{\Delta m}{2m_am_b}). \tag{6.9}$$

For the special case of a collision between protons and photons, the rest mass m_b of the photon will be zero and the expression reduces to

$$\epsilon_b(\gamma_a - \sqrt{\gamma_a^2-1}\cos\theta) = \Delta mc^2(1+\frac{\Delta m}{2m_a}). \tag{6.10}$$

So how big is now the threshold energy?

All terms just presented yield no real results, but are mere "working steps" towards the relevant expresssions. Nevertheless, they are of use for later derivations. Now a closer look is taken at the UHE protons and what happens as protons and photons collide. The calculations are done in the laboratory frame of the collision, so the proton is at rest, $\vec{p}_p = 0$. Its energy is therefore $\epsilon_p = m_pc^2$. If equation 6.6 is considered now and the values inserted, one gets a threshold energy of

$$E'_{th} = \epsilon_b = \Delta mc^2(1+\frac{\Delta m}{2m_p}). \tag{6.11}$$

Since collision of p and γ can also lead to the production of more pions, the mass difference can be written as $\Delta m = \xi m_\pi$, with $\xi = 1, 2, ...$ being the number of produced pions. For the production of a single neutral pion (π^0) with a mass of roughly 135 MeV the resulting threshold energy is then $E_{th} = 145$ MeV. For simplicity reasons $m_{\pi^0} = m_{\pi^+}$ is assumed for the entire study.
Looking at equation 6.10 one can also determine the minimal Lorentz factor that must be provided to have pion production taking place. If a photon with a mean energy of $\langle\epsilon\rangle$ in the lab frame is considered, the minimal Lorentz factor will occur in a head-on collision, where $\theta = 180°$. So $\cos\theta = -1$, leading to

$$\gamma_{min} = \frac{\xi m_\pi c^2}{2\langle\epsilon\rangle}\left(1+\frac{\xi m_\pi}{2m_p}\right). \tag{6.12}$$

For the case of the cosmic microwave background with a mean energy of $\langle\epsilon\rangle = 7\cdot10^{-4}$ eV and multipion production, one gets a resulting Lorentz factor of $\xi\cdot10^{11}$ that has to be provided. This corresponds to an energy of $E_{proton} \sim 9.4\cdot10^{19}$ eV. Simple kinetic considerations show that the GZK-cutoff comes into play only for UHECR! But as is seen, for example in figure 2.7 of this study, the GZK-cutoff sets in at earlier proton energies already. This happens, because protons can also interact with photons from the high-frequency tail from the Planck distribution. In that case, a lower proton energy than the one that was just derived, is enough to provide the necessary threshold energy. This spectral energy distribution of the photons is account for by an integration over the possible energies in the energy loss integral, see appendix B for details.

The proton rest frame

The above formulae are useful expressions, but for the parametrization of the cross section, as it is presented in chapter 2, the energy E_{rest} of the photon (particle b in the following calculations) as seen in the rest frame of the high energy proton (particle a) is of interest. The calculation starts again from equation 6.4 first the four-momenta are inserted into that expression. They are $P_a = (\frac{\epsilon_a}{c}, \vec{p_a})$ for the proton and for the photon $P_b = (\frac{\epsilon_b}{c}, \vec{p_b})$, respectively. In the lab frame one receives

$$P_a P_b = \frac{\epsilon_a \epsilon_b}{c^2} - \vec{p_a}\vec{p_b}. \tag{6.13}$$

If now the values for the proton at rest (no momentum, $\vec{p_a} = 0$) are put in, the result is

$$P_a P_b = m_a E_{rest} = \frac{\epsilon_a \epsilon_b}{c^2} - \vec{p_a}\vec{p_b}, \tag{6.14}$$

which introduces the energy of the photons as it is seen in the proton rest frame, E_{rest}. For a better understanding it is, only for a brief period of time, assumed that the photon has a mass m_b. The expression is solved for E_{rest} and, like before, the Lorentz factors are inserted. This leads to:

$$E_{rest} = m_b c^2 \left(\gamma_a \gamma_b - \sqrt{(\gamma_a^2 - 1)(\gamma_b^2 - 1)} \cos\theta \right). \tag{6.15}$$

But a photon is in fact massless. If this is included in equation 6.14 one gets:

$$E_{rest} = \epsilon_b \left(\gamma_a - \sqrt{(\gamma_a^2 - 1)} \cos\theta \right). \tag{6.16}$$

This expression is the essential tool for the understanding of the energy loss integral 2.21. This formula shows how important the role of the incident angle of the incoming photon is. For a "shallow" photon with a cosine close to unity, E_{rest} is approximated by

$$E_r = \epsilon_b \left(\gamma_a - \sqrt{(\gamma_a^2 - 1)} \right). \tag{6.17}$$

For a head on collision with $\cos\theta = -1$, one gets the maximal value of the expression:

$$E_r = \epsilon_b \left(\gamma_a + \sqrt{(\gamma_a^2 - 1)} \right). \tag{6.18}$$

In the case of UHE protons, the Lorentz factor is extremely high, as was just derived in 6.12 and therefore the result that is used in the energy loss integral is $E_{rest} = 2\epsilon_b \gamma_a$. The upper expressions show that, if the proton is at rest while colliding with a photon, the maximal energy that is contained in the collision can only be reached in a head-on collision. This is no revolutionary insight, but it is still nice to see that it comes out of this calculation, isn't it? The other parameter that plays a role, is the energy ϵ_b of the incoming photons, which is denoted as ε in the integral. As mentioned earlier, this is

described by a Planck distribution of different energies and yields a second important aspect for 2.21. The derivation of this expression is presented in appendix B.

Appendix B - Energy loss integral for $p\gamma$-collisions

The analysis of the $p\gamma$-interaction, as mentioned section 2.4.2, is performed by evaluating a double integral. A short derivation of the used formula is presented here.

The general expression for the collision length, the distance between two collisions of a particle, is given by $\lambda_{coll} = \frac{1}{n\sigma}$, where n describes the target density and σ the cross section of the interaction. This expression slightly changes, when the inelasticity K is taken into account. The collision length turns into an attenuation length, which is the distance where the probability that a particle has *not* interacted, has dropped to $1/e$. The expression looks like $\lambda_{att} = \frac{1}{n\sigma K}$.

The equation for the attenuation length is derived from the from the very basic definition of the collision rate $R = j \times \sigma$, where $j = \sqrt{j_\perp^2 + j_\parallel^2}$ is the current density. To receive an expression that can be turned into the energy loss integral $\frac{dE}{dt}$, some computation has to be done. The expression for the reaction rate is Lorentz transformed into the rest system of the proton. The photon parameters are marked by a prime. The proton velocity is v.
One should keep in mind that the current density is the product of particle density n and particle velocity v, $j = nv$. Besides, also the relations $j_\parallel = j \times \cos\theta = j \times \eta$ and $j_\perp = j \times \sin = j \times \sqrt{1 - \cos^2} = j \times \sqrt{1 - \eta^2}$ will be helpful. The transformation looks as follows:

$$\begin{aligned} |j_\parallel| &= \gamma(j'_\parallel - vn') = \gamma(j'\eta - vn') \\ &= \gamma(n'v'\eta - vn') \\ &= \gamma n'(\beta\eta - v), \text{where } \beta \text{ equals one since } v' = c. \\ &= \gamma n'(\eta - v). \end{aligned} \tag{6.19}$$

The proton velocity v is given in units of c. The transformation for the $j_\perp$-component is:

$$\begin{aligned} |j_\perp| = j'_\perp &= \beta n' \sqrt{1 - \eta^2} \\ &= n' \sqrt{1 - \eta^2}. \end{aligned} \tag{6.20}$$

Those transformations are then inserted:

$$
\begin{aligned}
j &= \sqrt{j_{\perp}^2 + j_{\parallel}^2} \\
&= \sqrt{n'^2(1-\eta^2) + \gamma^2 n'^2(\eta - v)^2} \\
&= n'\gamma\sqrt{\frac{1}{\gamma^2}(1-\eta^2) + (\eta - v)^2}, \text{ with } \frac{1}{\gamma^2} = (1 - \frac{v^2}{c^2}) = 1 - v^2 \text{ this yields} \\
&= n'\gamma\sqrt{(1-v^2)(1-\eta^2) + (\eta - v)^2} \\
&= n'\gamma\sqrt{1 + v^2\eta^2 - 2\eta v} \\
&= n'\gamma\sqrt{(1-\eta v)^2} \\
&= n'\gamma(1 - \eta v).
\end{aligned}
\tag{6.21}
$$

The photon density n' can be written as

$$
\begin{aligned}
n' &= \frac{n'}{4\pi} d\Omega = \frac{n'}{4\pi}\, 2\pi d(cos\theta) \\
&= \frac{n'}{4\pi} 2\pi d\eta.
\end{aligned}
\tag{6.22}
$$

If this is plugged into the expression for the collision rate, this looks like

$$
\begin{aligned}
R &= j \times \sigma \\
&= n'\gamma(1 - \eta v) \times \sigma \\
&= \frac{n'}{4\pi} 2\pi d\eta\, \gamma(1 - \eta v) \times \sigma
\end{aligned}
\tag{6.23}
$$

To receive the attenuation length λ_{att}, this is multiplied by the inelasticity K:

$$
\lambda_{att}^{-1} = \gamma \int_{-1}^{+1} d\eta \frac{(1 - \eta v)}{2} n' \sigma K \tag{6.24}
$$

Then the expression is divided by γ to transform back into the laboratory system of the collision. The velocity is assumed to be in units of c, so β enters the expression. The parameters of the cosmic ray are denoted with CR, the photon variables by γ. This describes now the attenuation length for a proton in a in an isotropic photon field. The integral bounds denote the upper and lower limit of the cosine. The integral consists of variables that depend either on the photon energy as seen in the proton rest frame ε' or on the photon energy in the laboratory frame ε. Therefore the double integral occurs:

$$
\lambda_{att}^{-1} = \int_{\varepsilon}^{\infty} d\varepsilon n(\varepsilon) \int_{-1}^{+1} d\eta \frac{1 - \eta\beta_{CR}}{2} \sigma(\varepsilon') K(\varepsilon') \tag{6.25}
$$

where η denotes the angle between the incoming photon and the proton. The cosmic ray (=proton) terms are abbreviated by CR.
The energy of the photon in the protons' rest frame is given by $\varepsilon' = \varepsilon\gamma_{CR}\,(1 - \beta_{CR}\eta)$. This expression can be verified by looking at equation 6.16 in appendix A. If there the incident angle $\cos\theta$ is traded with η, the photon energy ϵ_b with ε, γ_a with γ_{CR} and $\gamma^2 = \frac{1}{(1-\beta^2)}$ is inserted, one receives exactly the result of ε' just presented:

$$\begin{aligned} E_{rest} &= \epsilon_b \left(\gamma_a - \sqrt{\gamma_a^2 - 1}\cos\theta\right) \\ &= \varepsilon \left(\gamma_{CR} - \sqrt{\gamma_{CR}^2 - 1}\eta\right) \\ &= \varepsilon \left(\gamma_{CR} - \gamma_{CR}\sqrt{1 - \frac{1}{\gamma_{CR}^2}}\eta\right) \\ E_{rest} = \varepsilon' &= \varepsilon\gamma_{CR}\left(1 - \underbrace{\sqrt{1 - \frac{1}{\gamma_{CR}^2}}}_{\beta_{CR}}\,\eta\right) \end{aligned} \tag{6.26}$$

If this is solved this for η one receives

$$\eta = \frac{1}{\beta_{CR}} - \frac{\varepsilon'}{\gamma_{CR}\beta_{CR}\varepsilon}, \tag{6.27}$$

which can be used to derive $\frac{d\eta}{d\varepsilon'}$. The derivation yields $d\eta = -\frac{d\varepsilon'}{\gamma_{CR}\varepsilon\beta_{CR}}$. Inserting this into equation 6.25 gives

$$\lambda_{att}^{-1} = \frac{1}{2\gamma_{CR}^2\beta_{CR}} \int d\varepsilon n(\varepsilon)\frac{1}{\varepsilon^2}\int_{\gamma_{CR}\varepsilon(1+\beta_{CR})}^{\gamma_{CR}\varepsilon(1-\beta_{CR})} -d\varepsilon'\varepsilon'\sigma K, \tag{6.28}$$

whereas the integral bounds denote the value of ε' when η is $+1$ or -1. The minus sign in the latter integral is used to switch the integral bounds, giving now correct expressions for the minimal and maximal value of ε'.

$$\lambda_{att}^{-1} = \frac{1}{2\gamma_{CR}^2\beta_{CR}} \int d\varepsilon n(\varepsilon)\frac{1}{\varepsilon^2}\int_{\gamma_{CR}\varepsilon(1-\beta_{CR})}^{\gamma_{CR}\varepsilon(1+\beta_{CR})} d\varepsilon'\varepsilon'\sigma K \tag{6.29}$$

Taking the results from appendix A into account, the boundaries of the double integral can be converted. The bounds of the latter integral over the possible incident angles between the photon and the proton are determined by 6.16. The minimal energy that has to be present in the proton rest frame is the pion threshold energy, so the lower bound is set to $\varepsilon' = \varepsilon_{th} = 145$ MeV. The incident angle does not change this number. If, due to a "shallow" photon, the energy of 145 MeV is not reached, then the entire process of pion production does not take place. The upper bound for equation 6.29

arises for the case of $\cos\theta = -1$, the maximal photon energy in the proton rest frame is then $\varepsilon'_{max} = 2\gamma_p\varepsilon$. The relation $\varepsilon' = 2\gamma_p\varepsilon$ determines also the boundaries for the front integral of $d\varepsilon$. The lower bound emerges when ε' has its smallest possible value in the reaction, $\varepsilon' = \varepsilon_{th} = 145$ MeV. This yields $\varepsilon_{min} = \frac{\varepsilon_{th}}{2\gamma_p}$ as lower bound. The upper bound can reach any value that appears in the Planck distribution of the photons. The overall expression is now

$$\lambda^{-1} = \frac{1}{2\gamma_{CR}^2\beta_{CR}} \int_{\frac{\varepsilon_{th}}{2\gamma_p}}^{\infty} d\varepsilon n_\gamma(\varepsilon)\varepsilon^{-2} \times \int_{\varepsilon_{th}=145MeV}^{2\gamma_p\varepsilon} d\varepsilon'\varepsilon'\sigma(\varepsilon')K_p(\varepsilon'), \tag{6.30}$$

where the dependency on the photon energy is actually given as $\sigma(E_{CM}(\varepsilon'))$, see also section 2.4.2 for a detailed discussion. Since the energy losses $\frac{dE}{dt}$ rather than the attenuation length are of interest, the expression has to be amended which is done by closely examining the factor in front of the double integral. When inserting the values $\gamma = \frac{E_{CR}}{m_{CR}}$, $\beta_{CR} = \frac{v_{CR}}{c}$ and using a simple $t = \frac{\lambda}{v_{CR}}$ one changes

$$\lambda^{-1} = \frac{1}{2\gamma_{CR}^2\beta_{CR}} \quad \text{to} \quad t^{-1} = \frac{m_{CR}\,c}{2\gamma_{CR}^2 E_{CR}} \tag{6.31}$$

Now, if this is multiplied by the energy $E_p = E_{CR}$ of the cosmic ray proton, one gets the desired factor and the expression that can finally be used for calculations is:

$$\left(\frac{dE_p}{dt}\right)_{p\gamma} = \frac{m_p c}{2\gamma_p} \underbrace{\int_{\frac{\varepsilon_{th}}{2\gamma_p}}^{\infty} d\varepsilon n_\gamma(\varepsilon)\varepsilon^{-2}}_{photon\ distribution} \times \underbrace{\int_{\varepsilon_{th}=145MeV}^{2\gamma_p\varepsilon} d\varepsilon'\varepsilon'\sigma(\varepsilon')K_p(\varepsilon')}_{proton\ rest\ frame} \tag{6.32}$$

The factor in front of the integral changes, from $\frac{m_p c}{2\gamma_p}$ to $\frac{m_p c^3}{2\gamma_p}$ when the mass of the proton m_p is given in units of $[\frac{\mathrm{eV}}{\mathrm{c}^2}]$.

Appendix C – Solving a Differential Equation

In this appendix, a short outline on how an ordinary differential equation (ODE) is solved numerically with tools from the GNU scientific library, shall be given. The calculation that is presented here leads to energy losses, which are displayed in figure 4.1 in chapter 4. All the information that is presented here can also be found in the gsl reference manual on the GNU web page, *http://www.gnu.org/software/gsl/*. The gsl library provides a wide range of mathematical tools for solving an ODE, ranging from several ow-level components such as Runge-Kutta and Bulirsch-Stoer routines up to higher-level components, e.g. adaptive step-size control and evolution functions. In order to work with these tools correctly, some work is needed: First the ODE system must be defined, the actual equation that is to be solved. Then, one can choose among several algorithms to solve the ODE. Depending on how complex the equation is, not all available algorithms lead to the best solution. Besides, one can implement advanced methods to enhance the basic algorithms, one of them being the already mentioned step-size control. In this section, only those components will be presented and discussed that were actually used in the code for the calculations of this study. For detailed information on other tools it is recommended to turn to the gsl reference manual. An example of the code is presented in the end of this section, so it is possible to follow the individual steps of the calculation. Important declarations are given in bold writing.
For a proper implementation of all working tools, the header file **gsl_odeiv.h** has to be included in the beginning of the code. The first and probably most important step is to clearly define the ODE system. Every differential equation can be reduced to a n-dimensional first order equation, which looks like

$$\frac{dy_i}{dt} = f_i(t, y_1(t), \dots y_n(t)). \tag{6.33}$$

To implement this in a code, one has to use the **gsl_odeiv_system**, which stores the vector elements f_i of the ODE system along with the parameters of the function. The right-hand side of 6.33 is the equation that is supposed to be solved. In the case of this study, that are the energy loss equations 2.19, 2.21 and 2.26. In the code the allocation of the ODE is done in the main function $int\ main\{\}$. The gsl system has the name **sys** and is initialized in the header file *help.h* by **gsl_odeiv_system sys**. As is then seen in the *main* function, the gsl system contains the function to be solved $func$, the Jacobi matrix jac and other parameters $\&params$. It is one dimensional, since the loss equations depend only on the energy of the proton, E_p. The function $func$ is provided further up in the code and identifies the energy losses, $-edot \triangleq \frac{dE}{dt}$, as the right-hand side of the ODE. More sophisticated algorithms for solving a differential equation make use of the first order derivation of $f(t, y(t), parameters)$, so this should also be provided in order to interchange without problems between different algorithms. The Jacobian matrix has to be provided for this, because it stores the individual derivative elements $\frac{df}{dt}$. In the case of the energy losses this corresponds to

$\frac{d\dot{E}}{dE_p}$, since the functions are not time, but only E_p dependent. The matrix is therefore only a scalar. In the code this can be seen in the dimension of the matrix. It is set to $dim = 1$. The result of the derivation, marked as $resu = ejak$, is a simple numerical derivation of $\frac{dE}{dt}$ with respect to E_p. It is clear that the derivative $\frac{df}{dt}$ is set to zero, since there is no time dependence.
The Bulirsch-Stoer stepping-function, which was used, falls back on the Jacobian matrix. The algorithm for solving the ODE is allocated with **const gsl_odeiv_step_type * T** and chosen by **gsl_odeiv_step_bsimp**.
The stepping-function and the evolution function that were implemented play a big role on the speed and the accuracy of the calculations. It is therefore advisable to take a closer look at these routines. The stepping-function is the lowest-level component of the algorithms, it advances a solution from time t to a later time $t + h$, with a definite step-size of length h. Moreover, this component estimates the local error. The advance in t corresponds to an advance in $E(t)$, since the right-hand side equations are not directly time-dependent. To implement this correctly, one has to allocate enough space for this new instance. This is done with **gsl_odeiv_step * gsl_odeiv_step_alloc**. The stepping-functions work together with the adaptive step-size control functions. Those are further, high-level components that are available.
The size control functions are control functions that examine the proposed change for a stepping function, like the Bulirsch-Stoer method that is used here. They determine the optimal step-size h for an assessed level of error and communicate this to the stepping functions. These increase or decrease then the step size, depending on the size of the error. If the calculated error is smaller than the assessed one, this happens for example in nearly constant parts of the function f, the step size h can be increased. On the other hand, when the error tends to be big (at singularities or rapid changes of f), the step size must be decreased in order to receive the proposed error. The implementation happens with **gsl_odeiv_control * gsl_odeiv_control_y_new**, which creates a control object that keeps the local error on each step within the set bounds with respect to the solution y(t), E(t) respectively. In the code the absolute error is set to be 10^{17}eV, whereas the relative error is set to 10^{-2}.
The last and highest-level component that is discussed here is the evolution function. This combines the results of the stepping and control functions to advance the solution forward in time, without causing error messages. In case the control function signals that the step-size of the stepping function has to be decreased in order to achieve the defined error size, the evolution function backs out of the process and tries the proposed step sizes until the determined level of error is reached. The solution process comes to a entire halt and is not aborted, so the information about the process is stored. There is no loss of memory and so the process itself runs smoother. The pointer space necessary for the evolution function is allocated by **gsl_odeiv_evolve * gsl_odeiv_evolve_alloc** and has also a dimension of 1. It is applied by **int gsl_odeiv_evolve_apply** in the function *solve_ode* in the code. With this the important parameters for the solution are passed on. The function *solve_ode* receives

the time t_f, which is the time span the solution is advanced over. Furthermore the initial step size h and the starting time, $t = 0$, are assigned. The boundary condition for this is also set: at $t = 0$ there is a starting energy of $part- > ener$ (the energy at generation E_g), which is in the range of UHECR energies, $10^{19.5}$ eV in this example. The *while*-loop contains the evolution function, so as long as $t < t_f$ the solutions are advance to $t + h$. The values of the time t, the starting energy $y[0]$ (E_g in the code) and the calculated energy values $E(t)$, which corresponds to $y[1]$ in the code, are printed out.
When the calculation is done, all the allocated pointers must set free their memory space. This is done by **gsl_odeiv_step_free ()**, **gsl_odeiv_control_free ()** and **gsl_odeiv_evolve_free ()** at the end of the main programme.

```
//The header file, that is necessary for solution of an ode is  <gsl/gsl_odeiv.h>

#include <stdlib.h>
#include <stdio.h>
#include <string.h>
#include <getopt.h>
#include <math.h>
#include <gsl/gsl_math.h>
#include <gsl/gsl_deriv.h>
#include <gsl/gsl_sf.h>
#include <gsl/gsl_errno.h>
#include <gsl/gsl_matrix.h>
#include <gsl/gsl_odeiv.h>
#include <gsl/gsl_integration.h>
#include <gsl/gsl_interp.h>
#include <gsl/gsl_spline.h>
#include "help.h" //contains the allocation for the individual tools
#include "edot.h" //contains the energy loss functions dE/dt


int func (double t, const double y[], double f[], void *params);
int jac (double t, const double y[], double *dfdy,
 double dfdt[], void *params);


// This is the function func, that defines the ode system, the
right-hand side of
the first order differential equation

int
func (double t, const double y[], double f[], void *params)
{
struct func_params *part = (struct func_params *)params;
f[0] = -edot(y[0], part);
return GSL_SUCCESS;
}


// This function, jac, defines the Jacobi matrix.

int
jac (double t, const double y[], double *dfdy,
double dfdt[], void *params) {
double resu;
```

```
gsl_matrix_view dfdy_mat
= gsl_matrix_view_array (dfdy, 1, 1);
gsl_matrix * m = &dfdy_mat.matrix;
resu =  ejak(y[0],params); // the Jacobi matrix is calculated
                                // by the function ejak

gsl_matrix_set (m, 0, 0,resu);
dfdt[0]=0.0; // no time dependence
return GSL_SUCCESS;
}



//Here the ODE equation is solved. Printed are the evolution time t, the
//starting value E_{g} (y[0] in the code) and the energy loss E(t)
//(y[1] in the code).


double solve_ode (double tf, void *params ){
  struct func_params *part = (struct func_params *)params;
  double y[2];
  double h=1e-14*part->ener; // step size
  double t=1e3;   //0.0; // time, where the calculation starts
  y[0]= part->ener; // energy at generation E_{g}
  y[1]= -edot(y[0], params);

 while (t < tf){

   int status=  gsl_odeiv_evolve_apply (part->e, part->co, part->s,
&(part->sys), &t, tf, &h, y);

    if (status != GSL_SUCCESS){
    printf("break");
     break;
    }
    printf(" t=%.2e y[0]=%.6e y[1]=%.6e\n", t, y[0], y[1]);
  }

  return (y[0]);

}



 int main (int argc, char *argv[]){
```

```
        double ene;
double tf; // time, to which E(t) is calculated
struct func_params params;
setbuf(stdout, NULL);
params.T   = 2.725; //temperature of CMB in K
ene=19.50; //log10(energy at generation)

params.ener = pow(10., ene); // energy at generation E_{g}

double resu = ejak(params.ener, &params); // d(edot)/dE_p in s^-1;


  //From here on ode
gsl_odeiv_system sys = {func, jac, 1, &params};
const gsl_odeiv_step_type * T = gsl_odeiv_step_bsimp;
                                                //chooses the stepping function
params.s = gsl_odeiv_step_alloc (T, 1);
params.co = gsl_odeiv_control_y_new (1e17, 1e-2);// determines
                                               //the error of the stepping function
params.e = gsl_odeiv_evolve_alloc (1);
params.sys = sys;


tf= (100*params.ener/edot (params.ener, &params));

printf("%.6e \n ", solve_ode(tf, &params));


gsl_odeiv_evolve_free(params.e);
gsl_odeiv_control_free(params.co);
gsl_odeiv_step_free(params.s);

return(1);

}



//These are the paramters, that are included in the header file
"help.h"

  gsl_odeiv_system  sys;
  gsl_odeiv_step    * s;
  gsl_odeiv_evolve  * e;
```

```
  gsl_odeiv_control * co;
}
```

The energy loss is described by $edot = \frac{dE}{dt}$ and looks as follows in the code. The data files for the EBL and SCRF interpolation have to be defined in the main programme with

```
struct func_params params;
sprintf(params.template_file,"cluster.dat");
sprintf(params.template_fileebl,"ebl.dat");.
```

The edot-code:

```
#include <stdlib.h>
#include <stdio.h>
#include <math.h>
#include <gsl/gsl_integration.h>
#include <gsl/gsl_deriv.h>
#include <gsl/gsl_odeiv.h>
#include <gsl/gsl_interp.h>
#include <gsl/gsl_spline.h>
#include "help.h"
#include "constants.h"
#include "BH_Blumentahl.h"
#include "integration.h"
#include "nrutil.h"

double sq(double x) { return(x*x);}


// cross section sigma as parametrization
double sigma (double scme) {
double a[5] = { 0.10908323347151504 ,
0.03165050238465333 ,
0.458147574571271,
0.0009474657178335319,
-3.3644184990774306};
 return  (a[0] + a[1]/pow(scme,a[2]) + a[3]*sq( a[4] + log(scme)));
}


// back integral over epsilon^{prime}
double hikern (double lepsp, void *params){
struct func_params *part = (struct func_params*)params;
double epsp = exp(lepsp);
double sqeps = sq(epsp);
```

```
double cme= (sq(M_P) + 2.*epsp*M_P) ;// E_CM^{2} in eV
double scme=cme/1e9; // E_CM^{2} normalized to  GeV
double s; // cross section in [mb]
double r;

if (epsp < 500e6 ){
      part->K=0.2 ;
  s = 340e-3;
}

else {
          part->K=0.3;
          s = sigma(scme);
}

r = (MB * s * sqeps *part->K);
return (r);
}


//front integral over photon energy epsilon
double vikern (double leps, void *params){
struct func_params *part= (struct func_params*)params;
gsl_integration_workspace *w
= gsl_integration_workspace_alloc (100);
double result, error;
double eps,b, a;
gsl_function F;
F.function = &hikern;
F.params = params;
eps=exp(leps);
a=log(145e6);
b=log(2.*part->gamma*eps);
gsl_integration_qag(&F, a, b, 0.0, 1e-1,
100,GSL_INTEG_GAUSS51, w, &result, &error);
gsl_integration_workspace_free (w);

if ( (eps/(KB*part->T*J)) < 1e-5){

result= result*pow(eps, -2.)*eps*eps*KB*J*part->T*pow(pi,
-2.)*pow( (c*H_BAR), -3.);} // Rayleigh-Jeans law

else{ result=
result*eps*pow(pi,-2.)*pow((c*H_BAR),-3.)*pow(eps,2.)*pow(  (
exp(eps/(KB*J*part->T))    -1. ) , -1.)*pow(eps, -2.);}
 //Planck distribution
```

```
return (result);
}



//Interpolation for SCRF: imports wavelengths lambda (in microns) from
data file and returns intensity nuInu (in nanoWatt/(m^2 sr^1) ) aus

double nuInu(double epsilon, void *params){
struct func_params *part= (struct func_params*)params;
double resu;
if (part->acc == (gsl_interp_accel *)NULL){
part->acc = gsl_interp_accel_alloc();
}
if (part->spline == (gsl_spline*) NULL){
FILE *fp = fopen(part->template_file, "r");
double xval,yval;
printf("Die Datei cluster.dat wurde aufgerufen. \n");
double x[1000],y[1000];
char * line = NULL;
size_t len = 0;
ssize_t read;
int imax=0;
if (fp == NULL) {
  fprintf(stderr,"**ERROR \n Couldn't open file %s
                              %\n", part->template_file);
exit(-1);
}
while ((read = getline(&line, &len, fp)) != -1) {
sscanf(line,"%lg %lg",&xval,&yval);
x[imax] = log(xval);
y[imax] = log(yval);
imax++;
}
if (line)
free(line);

part->spline = gsl_spline_alloc(gsl_interp_cspline, imax);
gsl_spline_init(part->spline,x,y,imax);
fclose(fp);
}

resu = exp(gsl_spline_eval(part->spline,log(epsilon),part->acc));
return(resu);
}
```

```
 //Interpolation for EBL photon fields: imports wavelength lambda (in
microns) and returns intensity  nuInu (in nanoWatt/(m^2 sr^1))

double nuInuebl(double epsilon, void *params){

struct func_params *part= (struct func_params*)params;
double resu;
if (part->accebl == (gsl_interp_accel *)NULL){
part->accebl = gsl_interp_accel_alloc();
}
if (part->splineebl == (gsl_spline*) NULL){
FILE *fpebl = fopen(part->template_fileebl, "r");
double xval,yval;
printf("Die Datei ebl.dat wurde aufgerufen \n");
double x[1000],y[1000];
char * line = NULL;
size_t len = 0;
ssize_t read;
int imax=0;
if (fpebl == NULL) {
  fprintf(stderr,"**ERROR \n Couldn't open file %s
                                %\n", part->template_fileebl);
exit(-1);
}
while ((read = getline(&line, &len, fpebl)) != -1) {
sscanf(line,"%lg %lg",&xval,&yval);
x[imax] = log(xval);
y[imax] = log(yval);
imax++;
}
if (line)
free(line);
part->splineebl = gsl_spline_alloc(gsl_interp_cspline, imax);
gsl_spline_init(part->splineebl,x,y,imax);
fclose(fpebl);
}
resu = exp(gsl_spline_eval(part->splineebl,log(epsilon),part->accebl));
return(resu);

}


// front integral when photons from the SCRF are considered
double vikerncluster (double leps, void *params){
```

```
   struct func_params *part= (struct func_params *)params;
gsl_integration_workspace *w
= gsl_integration_workspace_alloc (100);
double result, error;
double eps,b, a;
gsl_function F;
F.function = &hikern;
F.params = params;
eps=exp(leps);
        a=log(145e6);
b=log(2.*part->gamma*eps);
gsl_integration_qag(&F, a, b, 0.0, 1e-1, 100,
GSL_INTEG_GAUSS21, w, &result, &error);

gsl_integration_workspace_free (w);

double lambda = (HEV*c*1e6)/eps;
double resu = nuInu (lambda, part);// result of interpolation
        double nu= c/(lambda*1e-6);
resu=resu/(nu);// changes  nu*I to I
        resu=resu*4*pi*1e-9/(c*H*nu); // h in J*s, resu now in units of [s/m^3]
resu=resu/(HEV); //resu now in units of  [#/m^3*eV]

      result *= pow(eps, -2.)*eps*resu;
return (result);
}


// front integral when photons from the EBL are considered
double vikernebl (double leps, void *params){

   struct func_params *part= (struct func_params *)params;
gsl_integration_workspace *w
= gsl_integration_workspace_alloc (100);
double result, error;
double eps,b, a;
gsl_function F;
F.function = &hikern;
F.params = params;
eps=exp(leps);
        a=log(145e6);
b=log(2.*part->gamma*eps);
gsl_integration_qag(&F, a, b, 0.0, 1e-1, 100,
GSL_INTEG_GAUSS61, w, &result, &error);
```

```
gsl_integration_workspace_free (w);

double lambda = (HEV*c*1e6)/eps;
double resu = nuInuebl (lambda, part); //result of interpolation
        double nu= c/(lambda*1e-6);
resu=resu/(nu);//changes  nu*I to I
resu=resu*4*pi*1e-9/(c*H*nu); // h in J*s, resu now in units
of  [s/m^3]
resu=resu/(HEV); //resu now in units of [#/m^3*eV]

      result *= pow(eps, -2.)*eps*resu;
return (result);
}


/* Calculation of  dE/dt in [eV/s] with  CMB photons;  */
double
edot(double x,  void *params){
struct func_params *part= (struct func_params*)params;
                part->ep=x;
part->gamma=x/M_P; //calculation of Lorentz factor
gsl_integration_workspace *ws
= gsl_integration_workspace_alloc (1000);
double result;
double error;
double b;
double a;
gsl_function F;
F.function = &vikern;
F.params = params;
b= log(1e19);// resembles infinity
a=log(145e6*M_P/(2*x));
gsl_integration_qag(&F, a, b, 0.0, 1e-1, 1000,
GSL_INTEG_GAUSS51, ws, &result, &error);

gsl_integration_workspace_free (ws);

double vorfaktor= M_P*M_P*c/(2*x);
result=result*vorfaktor; // dE/dt in eV/s
return (result);
}


//Calculation of dE/dt in [eV/s] with  cluster radiaton

double edotcluster(double x,  void *params){
```

```
struct func_params *part= (struct func_params*)params;
                //part->ep=x;
part->gamma=x/M_P; //Berechnung des Gammafaktors
gsl_integration_workspace *ws
= gsl_integration_workspace_alloc (10000);
double result;
double error;
double b;
double a;
gsl_function F;
F.function = &vikerncluster;
F.params = params;
b= log(1e19);
a=log(145e6*M_P/(2*x));
gsl_integration_qag(&F, a, b, 0.0, 1e-1, 10000,
GSL_INTEG_GAUSS21, ws, &result, &error);

gsl_integration_workspace_free (ws);

double vorfaktor= M_P*M_P*c/(2*x);
result=result*vorfaktor; // dE/dt in [eV/s]
return (result);
}


//Calculation of dE/dt in [eV/s] with EBL photons

double edotebl(double x,  void *params){
struct func_params *part= (struct func_params*)params;
                //part->ep=x;
part->gamma=x/M_P;
gsl_integration_workspace *ws
= gsl_integration_workspace_alloc (100);
double result;
double error;
double b;
double a;
gsl_function F;
F.function = &vikernebl;
F.params = params;
b= log(1e19);
a=log(145e6*M_P/(2*x));
                gsl_integration_qag(&F, a, b, 0.0, 1e-1, 100,
GSL_INTEG_GAUSS51, ws, &result, &error);

gsl_integration_workspace_free (ws);
```

```
double vorfaktor= M_P*M_P*c/(2*x);
result=result*vorfaktor; // dE/dt in [eV/s]
return (result);
}
```

This part of the code accesses some constants that are given in the header file "help.h":

```
/*Used constants:*/

#define c 2.9979e8   // in [m/s]
#define H_BAR 6.58211899e-16 // hbar in [eV*s]
#define H 6.626068e-34  // h in [J*s]
#define ALPHA .00729927007299270072 // fine structure constant
#define HEV 4.13566733e-15  //h in [eV*s]

#define pi 3.1415
#define J 6.242e18  // changes J to eV
#define ERG 6.2415e11 // changes erg to eV
#define KB 1.3806503e-23  // Boltzmann constant in [J/K]
#define M_P 0.938e9  // mass of proton in [eV/c^2]
#define MASS_E 0.511e6  // mass of electron in [eV/c^2]
#define YR 3.17e-8  // changes  s to  yrs

#define M  3.3e-23  // changes  m to Mpc
#define MB 1e-31  // changes  mb to  m^2
#define THOM 6.65e-29  // Thomson cross section in [m^-2]
#define E_th 1.22e9  //threshold enery for pion production
#define eps_th 145e6  //threshold energy in proton rest
frame for pionproduction
#define n_gamma 4.13e8  // CMB photon density in [#/m^3]

struct func_params
{
double x; // log10(proton energy [eV])
        double ep; // is proton energy (E_p), used for Lorentz factor
        double p; // is pow(10, x)
double K; // inelasticity
double sigma; // cross section in [mb]
double gamma;// Lorentz factor
   double T; // temperature in [K]
        double L;
        double n; // ISG density
  double B; // magntic field in [nG]
  double Z;// charge of particle
  double l; // gyroradius
```

```
  double E_null, E_eins;
  double D_Bohmnull, D_Bohmeins;
  double R; //radius of supercluster in [Mpc]
  double lambda;// nur fuer plot der planckkurve
  double nu; //nur fuer plot der planckkurve
  double en; //nur fuer plot der planckkurve
  double ener;
  double E_g; // energy at generation
  double tf;// t_final, upper integration bound
  double P; // pulse duration in [yr]
  double ti; // t_initital, differenz of tf and P,lower integration bound
  double r; // distance to proton source
  double gamma_g; // index of generation spectrum
  double L_p; // luminosity of source
  char template_file[100];
  char template_fileebl[100];
  char template_filelookbethe[1000];
  char template_filelookcmb[1000];
  char template_filelookcmbadd[1000];
  gsl_spline  *spline;
  gsl_interp_accel *acc;
  gsl_spline  *splineebl;
  gsl_interp_accel *accebl;
  gsl_spline  *splinelookbethe;
  gsl_interp_accel *acclookbethe;
  gsl_odeiv_system  sys;
  gsl_odeiv_step    * s;
  gsl_odeiv_evolve  * e;
  gsl_odeiv_control * co;
};
```

Bibliography

[1] J. Abraham et al., *Measurement of the energy spectrum of cosmic rays above* 10^{18} *eV using the Pierre Auger Observatory*, Phys. Lett. **B685** (2010), 239–246.

[2] P. M. Bauleo and J. Rodríguez Martino, *The dawn of the particle astronomy era in ultra-high-energy cosmic rays*, Nature**458** (2009), 847–851.

[3] Volker Beckmann, S. Soldi, C. R. Shrader, N. Gehrels, and N. Produit, *The Hard X-ray 20-40 keV AGN Luminosity Function*, Astrophys. J. **652** (2006), 126–135.

[4] V. S. Berezinskii, S. V. Bulanov, V. A. Dogiel, and V. S. Ptuskin, *Astrophysics of cosmic rays*, 1990.

[5] V. S. Berezinskii, S. I. Grigor'eva, and V. A. Dogiel, *Predicted spectrum and anisotropy of the ultra-high energy cosmic rays in a single-source model*, A&A**232** (1990), 582–588.

[6] D. Binosi and L. TheuSSl, *Jaxodraw: A graphical user interface for drawing feynman diagrams*, Computer Physics Communications **161** (2004), no. 1-2, 76 – 86.

[7] George R. Blumenthal, *Energy loss of high-energy cosmic rays in pair-producing collisions with ambient photons*, Phys. Rev. D **1** (1970), no. 6, 1596–1602.

[8] S. P. Boughn, *X-Ray Emission from the Local Supercluster: Possible Evidence for Hot, Diffuse Gas*, ApJ**526** (1999), 14–26.

[9] M. J. Chodorowski, A. A. Zdziarski, and M. Sikora, *Reaction rate and energy-loss rate for photopair production by relativistic nuclei*, ApJ**400** (1992), 181–185.

[10] R. S. Fletcher, T. K. Gaisser, Paolo Lipari, and Todor Stanev, *sibyll: An event generator for simulation of high energy cosmic ray cascades*, Phys. Rev. D **50** (1994), no. 9, 5710–5731.

[11] M. Giler, J. Wdowczyk, and A. W. Wolfendale, *Ultra-high-energy cosmic rays from clusters of galaxies*, Journal of Physics G Nuclear Physics **6** (1980), 1561–1573.

[12] V. L. Ginzburg and S. I. Syrovatskii, *The Origin of Cosmic Rays*, 1964.

[13] N. Globus, D. Allard, and E. Parizot, *Propagation of high-energy cosmic rays in extragalactic turbulent magnetic fields: resulting energy spectrum and composition*, A&A**479** (2008), 97–110.

[14] Nickolay Y. Gnedin, *Effect of cosmic ultraviolet background on star formation in high-redshift galaxies*, The Astrophysical Journal Letters **721** (2010), no. 2, L79.

[15] Kenneth Greisen, *End to the cosmic-ray spectrum?*, Phys. Rev. Lett. **16** (1966), no. 17, 748–750.

[16] C. Grupen, *Astroparticle Physics*, 2005.

[17] A. M. Hillas, *Cosmic Rays: Recent Progress and some Current Questions*, ArXiv Astrophysics e-prints (2006).

[18] S. R. Kelner, F. A. Aharonian, and V. V. Bugayov, *Energy spectra of gamma rays, electrons, and neutrinos produced at proton-proton interactions in the very high energy regime*, Phys. Rev. D**74** (2006), no. 3, 034018–+.

[19] T. M. Kneiske and H. Dole, *A strict lower-limit EBL Applications on gamma-ray absorption*, American Institute of Physics Conference Series (F. A. Aharonian, W. Hofmann, & F. Rieger, ed.), American Institute of Physics Conference Series, vol. 1085, December 2008, pp. 620–623.

[20] K. Mannheim and R. Schlickeiser, *Interactions of cosmic ray nuclei*, A&A**286** (1994), 983–996.

[21] G. Matthiae, *The cosmic ray energy spectrum as measured using the Pierre Auger Observatory*, New Journal of Physics **12** (2010), no. 7, 075009–+.

[22] C. D. Orth and A. Buffington, *Secondary cosmic-ray electrons and positrons from 1 to 100 GeV in the upper atmosphere and interstellar space, and interpretation of a recent positron flux measurement*, ApJ**206** (1976), 312–332.

[23] R. Schlickeiser, *Cosmic Ray Astrophysics*, 2002.

[24] G. Sigl, M. Lemoine, and P. Biermann, *Ultra-high energy cosmic ray propagation in the local supercluster*, Astroparticle Physics **10** (1999), 141–156.

[25] The Pierre AUGER Collaboration, P. Abreu, M. Aglietta, E. J. Ahn, D. Allard, I. Allekotte, J. Allen, J. Alvarez Castillo, J. Alvarez-Muñiz, M. Ambrosio, and et al., *Update on the correlation of the highest energy cosmic rays with nearby extragalactic matter*, Astroparticle Physics **34** (2010), 314–326.

[26] R. B. Tully, *The Local Supercluster*, ApJ**257** (1982), 389–422.

[27] S. Weinberg, *The first three minutes. A modern view of the origin of the universe*, 1977.

[28] G. T. Zatsepin and V. A. Kuzmin, *Upper limit of the spectrum of cosmic rays*, JETP Lett. **4** (1966), 78–80.

Danksagung

To everything (turn, turn, turn),
There is a season (turn, turn, turn),
And a time to every purpose under heaven.
Pete Seeger, 1950

Nun ist es an der Zeit all jenen zu danken, die mich in den Jahren meines Studiums und besonders auf der Zielgeraden begleitet haben.
Zunächst wäre da Prof. Dieter Horns zu nennen, der mir die Gelegenheit gegeben hat, mich eindringlich mit der Propagation von kosmischen Teilchen und den Abgründen der Programmiererei zu befassen und nicht müde wurde, Basisarbeit in den verschiedensten Fragen zu leisten. Desweiteren Dr. Tanja Kneiske, deren code und EBL-Modell ich nach Belieben ausschlachten konnte und mit der ich, trotz Diplomarbeits-Stresses, den tollsten Mutter-Kind-Raum der Uni Hamburg ins Leben gerufen habe. Ausserdem möchte ich mich ganz besonders bei "meinen Jungs" aus dem Büro Nummer 14 bedanken, Attila, Eike, Ian und Jan, die mich in wechselnder Besetzung während des letzten Jahres stets bei Laune gehalten haben und natürlich auch dem Rest der Horns-Gruppe, der eine sehr nette Arbeitsatmosphäre geschaffen hat. Desweiteren möchte ich den DynamiX-lern danken, dass sie mich trotz Abtrünnigkeit immer wieder so herzlich empfangen haben. Nicht zu Letzt, möchte ich an dieser Stelle auch meine Eltern Danke sagen, für die nötige Geduld und Zuversicht, die sie für dieses Langzeitexperiment aufgebracht haben.
Schliesslich, gilt ein besonders herzlicher Dank denjenigen, die dieses ganze Physikstudium (in Hamburg!) ins Rollen gebracht haben: Prof. Dr. Lutz Wisotzki, Dr. Knud Jahnke, Dr. Björn Kuhlbrodt und Dr. Sebastian Sánchez. Und ein noch herzlicherer Dank geht an die, die es am Laufen gehalten haben: Dr. Erik Butz, Daniel Bick und an den, der alle Höhen und Tiefen mitgemacht hat - meinen Herrn Björn.

Und, nur um ihn mal einer breiteren Öffentlichkeit zu präsentieren, der "Sherman's Lagoon" comic, welcher mich erfolgreich das letzte halbe Jahr hindurch erheitert hat: